Johannes Gutenberg–Universität

Mainz

Institut für Kernphysik

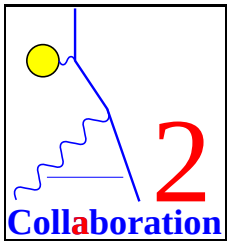

First Doubly Polarised Photoproduction on ^{3}He at the Photon Beam of MAMI

Ph. D. Thesis

of

Patricia Aguar Bartolomé

November 2010

≪Wenn du es nicht versuchst,
wirst du es nicht bekommen≫

≪Si no lo intentas,
nunca lo conseguirás≫

J. W. Goethe, *"Fausto".*

Dedicado a mi madre y mi hermano

Abstract

A first experiment with a polarised ^{3}He target was carried out in July 2009 at the MAMI accelerator in Mainz in a photon energy range between 200 MeV and 800 MeV. The aim of this measurement was to investigate the Gerasimov-Drell-Hearn sum rule on the neutron. The use of the data obtained with the polarised ^{3}He target, compared to existing data on the deuteron, gives a complementary and more direct access to the neutron, due to the spin structure of the ^{3}He.
The measurement of the helicity dependence of the inclusive total photoabsorption cross section required a beam of tagged circularly polarised photons incident on the longitudinally polarised ^{3}He target. The data were taken using the 4π Crystal Ball photon spectrometer in combination with TAPS as a forward wall and complemented by a threshold Cherenkov detector used to on-line suppress the background from electromagnetic events.
The development and preparation of the different components of the ^{3}He experimental setup was an important part of this work and are described in detail in this thesis.
The detector system and the analysis method were tested by the measurement of the unpolarised total inclusive photoabsorption cross section on liquid hydrogen. The results obtained are in good agreement with previous published data.
Preliminary results of the unpolarised total photoabsorption cross section, as well as the helicity dependent photoabsorption cross section difference on ^{3}He compared with several theoretical models will also be presented.

Zusammenfassung

Im Juli 2009 wurde am Mainzer Microtron (MAMI) erstmal ein Experiment durchgeführt, bei dem ein polarisiertes ^{3}He Target mit Photonen im Energiebereich von 200 bis 800 MeV untersucht wurde. Das Ziel dieses Experiments war die Überprüfung der Gerasimov-Drell-Hearn Summenregel am Neutron. Die Verwendung der Messdaten welche mit dem polarisierten ^{3}He Target gewonnen wurden, geben - im Vergleich mit den bereits existieren Daten vom Deuteron - aufgrund der Spin-Struktur des ^{3}He einen komplementären und direkteren Zugang zum Neutron. Die Messung des totalen helizitätsabhängigen Photoabsorptions-Wirkungsquerschnitts wurde mittels eines energiemarkierten Strahls von zirkular polarisierten Photonen, welcher auf das longitudinal polarisierte ^{3}He Target trifft, durchgeführt. Als Produktdetektoren kamen der Crystal Ball (4π Raumabdeckung), TAPS (als "Vorwärtswand") sowie ein Schwellen-Cherenkov-Detektor (online Veto zur Reduktion von elektromagnetischen Ereignissen) zum Einsatz.
Planung und Aufbau der verschiedenen komponenten Teile des ^{3}He Experimentaufbaus war ein entscheidender Teil dieser Dissertation und wird detailliert in der vorliegenden Arbeit beschrieben. Das Detektorsystem als auch die Analyse-Methoden wurden durch die Messung des unpolarisierten, totalen und inklusiven Photoabsoprtions-Wirkungsquerschnitts an flüssigem Wasserstoff getestet. Hierbei zeigten die Ergebnisse eine gute Übereinstimmung mit bereits zuvor publizierten Daten. Vorläufige Ergebnisse des unpolarisierten totalen Photoabsorptions-Wirkungsquerschnitts sowie der helizitätsabhängige Unterschied zwischen Photoabsorptions-Wirkungsquerschnitten an ^{3}He im Vergleich zu verschiedenen theoretischen Modellen werden vorgestellt.

Contents

List of Figures

List of Tables

Chapter 1
Introduction

The nucleon internal structure has been a central issue in nuclear and particle physics activities since the beginning of the 1960's. Of particular interest is the study of the spin structure which is not as well understood as other nucleon properties such as charge, mass or magnetic moment. With this purpose many scattering experiments were designed to investigate the spin structure of the nucleon. In 1968, the fundamental experiments of Friedmann, Kendall and Taylor at SLAC in the Deep Inelastic Scattering (DIS) [1] regime gave the first evidence of a nucleon substructure. The experimental result was in accordance with the Feynman parton model [2] and the partons were identified with the quarks and gluons introduced by Gell-Mann [3] and Zweig [4] to explain hadron mass spectroscopy. This new theory describing the behaviour of these quarks and gluons was called Quantum Chromo Dynamics(QCD). In this context, the nucleons are composed of three valence quarks which are bound together by gluons.
Experiments at SLAC in 1976 [5] and 1980 [6] measured the contribution of the quarks to the total nucleon spin. These first results were in agreement with the parton model prediction, but the EMC experiment at CERN in 1987 [7] found that at small distances the quarks carry only a fraction of the total nucleon spin. This result is known as the "spin crisis".
The information obtained from the different polarised DIS experiments was complemented with a number of sum rules like those due to Bjorken [8], Ellis-Jaffe [9] and Gerasimov, Drell and Hearn (GDH) [10]. The Bjorken and Ellis-Jaffe sum rules are derived for high four-momentum transfer Q^2 and relate the first moment of the nucleon's first spin structure function g_1 to the scale invariant axial charges of the target nucleon [11-15]. The other fundamental sum rule, the Gerasimov-Drell-Hern sum rule, holds at $Q^2 = 0$ and is valid in the real photon limit, $Q^2 = 0$.
The GDH sum rule is derived from fundamental physics principles and can be written as:

$$I_{GDH} = \int_{\nu_0}^{\infty} \frac{\sigma_p - \sigma_a}{\nu} d\nu = 4\pi^2\kappa^2 \frac{e^2}{M^2} S$$

where σ_p and σ_a are the total absorption cross sections of circularly polarised photons on longitudinally polarised nucleons with parallel and anti-parallel polarisation orientations, respectively. The cross section difference is weighted by the photon energy ν and is integrated over all photon energies. The integral of the difference of these cross sections is related to the nucleon magnetic moment κ and connects the static properties of the nucleon with the dynamics of the excitation spectrum.
The first experimental check of the GDH sum rule was the measurement of the total photoabsorption cross section on the proton carried out jointly at Mainz and Bonn by the GDH collaboration, with a measured photon energy range between 200 MeV and 2.9 GeV. The combined results obtained in these measurements support the validity of the GDH sum rule for the proton.
For the neutron, due to the lack of free neutron targets, the experimental verification of the GDH sum rule has to be performed using polarised deuteron or ^{3}He targets. In the deuteron, the proton and the neutron are essentially in S states of relative motion with aligned spins, while in the ^{3}He ground state, the nucleus predominantly consist of two spin paired protons and an unpaired neutron also in the S-state. This configuration effectively cancels the proton contribution to the nuclear magnetic moment [16]. Hence, with slight corrections for the residual proton effects [17], the ^{3}He nuclear spin is dominated by that of the neutron. Therefore, the proton contribution to the measured helicity dependent yields is smaller for the ^{3}He than for the deuteron and thus the ^{3}He spin structure is closer to the free neutron.
The helicity dependent total inclusive cross section on the deuteron was measured by the GDH-Collaboration in the photon energy range from 200 MeV to 1.9 GeV at Mainz and Bonn, while there was no polarised data for ^{3}He . Therefore, it was decided to perform the first double polarisation experiment on ^{3}He with a measured photon energy range between 200 and 800 MeV. The measurement was carried out in Mainz in July 2009.
The different steps in the preparation of this measurement and the final results obtained from the analysis of the data are the main topic of this thesis. The GDH sum rule and the physics motivation are presented in Chapter 2. A detailed description of the Mainz experimental setup is given in Chapter 3. The method used to polarise the ^{3}He gas and the relaxation mechanisms, as well as the description of all the different components of the ^{3}He setup and the polarimetry measurement are shown in Chapter 4. In Chapter 5 is outlined the experimental method and the trigger conditions used in the measurement. The analyisis procedure and the total photoabsorption cross section obtained in the unpolarised feasibility test on hydrogen carried out in March 2009 and the analyisis of the polarised ^{3}He data are presented in Chapter 6. The results for the helicity dependent total photoabsorption cross section difference obtained from the polarised ^{3}He data compared with some theoretical models are given in chapter 7. Finally, in Chapter 8 a summary and some conclusions from this work are presented.

Chapter 2
The Gerasimov-Drell-Hearn Sum Rule

The Gerasimov-Drell-Hearn (GDH) sum rule is an important prediction of QCD that was first derived by Gerasimov [18] and independently by Drell and Hearn [19]. It relates the integral over the helicity asymetry of the total absorption cross section for circularly polarised photons on a longitudinally polarised nucleon target to the nucleon anomalous magnetic moment κ, the spin S and the mass M:

$$I_{GDH} = \int_{\nu_{th}}^{\infty} \frac{\sigma_p - \sigma_a}{\nu} d\nu = 4\pi^2\kappa^2 \frac{e^2}{M^2} S \tag{2.1}$$

where σ_p and σ_a are the total absorption cross sections for parallel and antiparallel relative spin configurations (see Fig. 2.1) respectively, and the cross section is weighted by the inverse of the photon energy ν. The lower limit of the integral, ν_{th}, corresponds to the inelastic threshold of the reaction which, in the case of the nucleons, is the pion photoproduction threshold.

2.1 Derivation of the GDH Sum Rule

The GDH sum rule is derived from very general fundamental physical principles and is based on the following assumptions:

1. Lorentz and Gauge invariance $\Longrightarrow$ Low's Theorem.
2. Causality and Analyticity.
3. Crossing symmetry.
4. Unitarity $\Longrightarrow$ Optical Theorem.

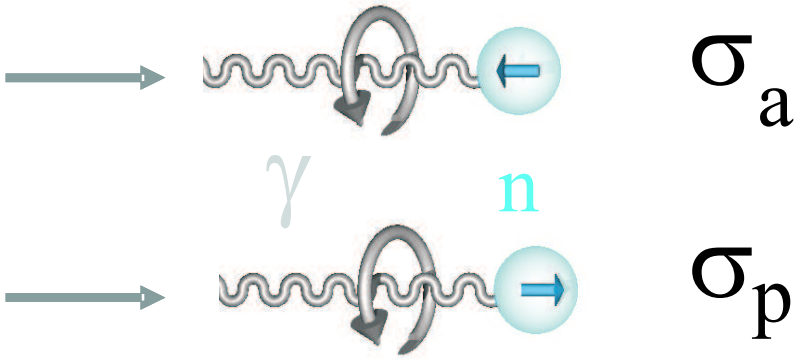

Figure 2.1: Spin configuration

5. No-subtraction hypothesis.

In the following this derivation will be outlined in detail.

2.1.1 Forward Compton Scattering Amplitude

The nucleon forward Compton amplitude for a scattering angle equal to zero can be written as [20]:

$$F(\theta = 0, \nu) = \langle \chi_2 | f_1(\nu) \vec{\epsilon_2}^* \cdot \vec{\epsilon_1} + f_2(\nu) i\vec{\sigma} \cdot (\vec{\epsilon_2}^* \times \vec{\epsilon_1}) | \chi_1 \rangle \tag{2.2}$$

where ν is the real photon energy, χ_1 and χ_2 are the initial and final spinors of the nucleon, $\vec{\epsilon_1}$ and $\vec{\epsilon_2}$ are the transverse polarisation vectors of the incident and scattered photon, respectively, and $\vec{\sigma}$ is the Pauli matrix vector which acts on the spinor of the nucleon. $f_1(\nu)$ denotes the non-spin-flip part of the amplitude and $f_2(\nu)$ is the spin-flip contribution which is accessible only via doubly polarised measurements. Using right and left handed circularly polarised photons the two polarisation vectors are:

$$\vec{\epsilon}_R = -\frac{1}{\sqrt{2}}(\vec{\epsilon}_x + i\vec{\epsilon}_y), \qquad \vec{\epsilon}_L = +\frac{1}{\sqrt{2}}(\vec{\epsilon}_x - i\vec{\epsilon}_y) \tag{2.3}$$

with the z-axis being the direction of motion of the photon. From the two products of Eq. (2.2) one obtains the following combinations:

$$\vec{\epsilon_2}^* \cdot \vec{\epsilon_1} = \begin{cases} 1 & \vec{\epsilon}_1 = \vec{\epsilon}_2 = \vec{\epsilon}_R \\ 1 & \vec{\epsilon}_1 = \vec{\epsilon}_2 = \vec{\epsilon}_L \\ 0 & \vec{\epsilon}_1 \neq \vec{\epsilon}_2 \end{cases} \tag{2.4}$$

$$\vec{\epsilon_2}^* \times \vec{\epsilon}_1 = \begin{cases} i\vec{\epsilon}_z & \vec{\epsilon}_1 = \vec{\epsilon}_2 = \vec{\epsilon}_R \\ -i\vec{\epsilon}_z & \vec{\epsilon}_1 = \vec{\epsilon}_2 = \vec{\epsilon}_L \\ 0 & \vec{\epsilon}_1 \neq \vec{\epsilon}_2 \end{cases} \tag{2.5}$$

There are two possible spin combinations when using circularly polarised photons and longitudinally polarised nucleons when the spinor of the nucleon is parallel ($S = 3/2$) or antiparallel ($S = 1/2$) to the photon polarisation. Then, the scattering amplitudes can be written as:

$$f_{3/2}(\nu) = f_1(\nu) - f_2(\nu), \qquad f_{1/2}(\nu) = f_1(\nu) + f_2(\nu) \tag{2.6}$$

or:

$$f_1(\nu) = \frac{f_{3/2}(\nu) + f_{1/2}(\nu)}{2}, \qquad f_2(\nu) = \frac{f_{3/2}(\nu) - f_{1/2}(\nu)}{2} \tag{2.7}$$

The total absorption cross section as the average of the two helicity cross sections can be defined in a similar way:

$$\sigma_T = \frac{\sigma_{3/2} + \sigma_{1/2}}{2} \tag{2.8}$$

and also the transverse-transverse interference term:

$$\sigma_{TT} = \frac{\sigma_{3/2} - \sigma_{1/2}}{2} \tag{2.9}$$

2.1.2 Causality and Analyticity

Causality implies analyticity of the Compton scattering amplitude $f(\nu)$ in the complex plane. One can apply now the Cauchy's integral therorem:

$$f(\nu) = \frac{1}{2\pi i} \oint_C \frac{f(\nu')}{\nu' - \nu} d\nu' \tag{2.10}$$

The integral of the path C as depicted in Fig. 2.2 has to be taken counter-clockwise. $K_+(0, \infty)$ is the half-circle at infinity in the upper half of the complex plane and $K_-(\nu, \varepsilon)$ a small half circle around ν of radius ε in the lower half of the complex plane with the center ν on the real axis. The individual contributions from the segments of the integration path can be evaluated now:

$$\begin{aligned} f(\nu) &= \frac{1}{2\pi i} \mathcal{P} \int_{-\infty}^{+\infty} \frac{f(\nu')}{\nu' - \nu} d\nu' \\ &\quad + \frac{1}{2\pi i} \int_{K_+(0,\infty)} \frac{f(\nu')}{\nu' - \nu} d\nu' + \lim_{\varepsilon \to 0} \frac{1}{2\pi i} \int_{K_-(\nu,\varepsilon)} \frac{f(\nu')}{\nu' - \nu} d\nu' \end{aligned} \tag{2.11}$$

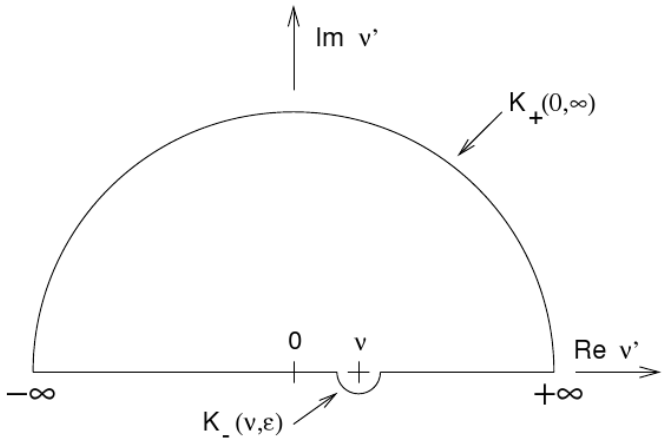

Figure 2.2: Cauchy's integration path applied to the forward scattering amplitude.

with the Cauchy principle value:

$$\mathcal{P}\int_{-\infty}^{+\infty} \equiv \lim_{\varepsilon\to 0}\int_{-\infty}^{\nu-\varepsilon} + \int_{\nu+\varepsilon}^{+\infty} \tag{2.12}$$

Using the residue theorem the integral for $K_-(\nu,\varepsilon)$ can be evaluated and is equal to $\frac{1}{2}f(\nu)$. Under the assumption of the "No-Subtraction" hypothesis (see section 2.1.4) the integral along the path $K_+(0,\infty)$ becomes zero. One then obtains:

$$f(\nu) = \frac{1}{\pi i}\,\mathcal{P}\int_{-\infty}^{+\infty}\frac{f(\nu')}{\nu'-\nu}d\nu'. \tag{2.13}$$

2.1.3 Crossing Symmetry

The Compton scattering amplitude has to be symmetric under the exchange of momentum ($\vec{k_1}\to-\vec{k_2}$) and polarisation ($\vec{\epsilon_1}\to\vec{\epsilon_2}^*$) for the ingoing and outgoing photons. This symmetry is called crossing symmetry and is exact for all orders of electromagnetic coupling. Therefore, the crossing properties for the Compton amplitude can be writen as:

$$F(\vec{k_1},\vec{\epsilon_1},\vec{\epsilon_2}) = F^*(-\vec{k_2},\vec{\epsilon_2}^*\vec{\epsilon_1}^*) \tag{2.14}$$

Appliying this crossing properties to F, f_1,f_2, and f_2/ν one then obtains:

$$\begin{aligned} F(\theta=0,-\nu) = F^*(\theta=0,\nu), \qquad & f_1(-\nu) = f_1^*(\nu), \\ f_2(-\nu) = -f_2^*(\nu), \qquad & \frac{f_2(-\nu)}{-\nu} = \frac{f_2^*(\nu)}{\nu} \end{aligned} \tag{2.15}$$

In the following, Eq.(2.13) will be used only for f_1 and f_2/ν. Therefore the crossing relation for f can be expressed as: $f(-\nu) = f^*(\nu)$.
One can now write Eq.(2.13) as:

$$f(\nu) = \frac{1}{\pi i}\,\mathcal{P}\int_0^{+\infty}\left(\frac{f(\nu')}{\nu'-\nu} + \frac{f^*(\nu')}{-\nu'-\nu}\right)d\nu'. \tag{2.16}$$

2.1.4 Dispersion Relations

The real and imaginary parts of $f(\nu)$ can be written as:

$$Ref(\nu) = \frac{1}{2}(f(\nu) + f^*(\nu)), \qquad Imf(\nu) = \frac{1}{2i}(f(\nu) - f^*(\nu)) \tag{2.17}$$

Considering the real part only, the Eq.(2.16) simplifies to the so called Kramers-Kronig [21] dispersion relation:

$$Ref(\nu) = \frac{2}{\pi}\,\mathcal{P}\int_0^{+\infty}\frac{Imf(\nu')}{\nu'^2-\nu^2}\nu' d\nu'. \tag{2.18}$$

Optical Theorem

The optical theorem can be derived from current conservation which is also called unitarity. It connects the imaginary part of the amplitudes and the total absorption cross section:

$$Imf(\nu) = \frac{\nu}{4\pi}\sigma. \tag{2.19}$$

Using Eq.(2.7) and Eq.(2.19) one obtains:

$$Imf_1(\nu) = \frac{\nu}{8\pi}[\sigma_{3/2}(\nu) + \sigma_{1/2}(\nu)] = \frac{\nu}{4\pi}\sigma_T(\nu) \tag{2.20}$$

$$Imf_2(\nu) = -\frac{\nu}{8\pi}[\sigma_{3/2}(\nu) - \sigma_{1/2}(\nu)] = -\frac{\nu}{4\pi}\sigma_{TT}(\nu). \tag{2.21}$$

For the transverse polarisation of the photon the subscripts of the total cross sections $\sigma_{3/2}$ and $\sigma_{1/2}$ denote the total helicity of the photon-nucleon system in the nucleon rest frame with respect to the center of mass momentum.

Low's Theorem

For small values of the photon energy ν, the functions f_1 and f_2 can be developed as:

$$f_1(\nu) = -\frac{\alpha}{m} + (\alpha_E + \beta_M)\nu^2 + \mathcal{O}(\nu^4), \tag{2.22}$$

$$f_2(\nu) = -\frac{\alpha\kappa_N^2}{2m^2}\nu + \gamma_0\nu^3 + \mathcal{O}(\nu^5). \tag{2.23}$$

The first term in the spin-independent amplitude f_1 describes the Thompson scattering which depends on mass and charge and is a consequence of gauge invariance. The second term is described by Rayleigh scattering and is related to the electric (α_E) and magnetic (β_M) polarisabilities. The spin-dependent amplitude f_2 is given by the low energy theorem of Low [22], Gell-Mann and Goldberger [23] and appears as a consequence of both gauge and relativistic invariance. In this case, the first term is determined by the anomalous magnetic moment κ_N and the so called spin polarisability γ_0 in the third order of ν.
The static properties of Eq.(2.22) and Eq.(2.23) can be connected with the cross sections of Eq.(2.20) and Eq.(2.21) via the dispersion relation given in Eq.(2.18).
Expanding the integrand into a series the following equations are obtained:

$$\begin{aligned} Re f_1(\nu) &= \frac{1}{2\pi^2}\,\mathcal{P}\int_0^{+\infty}\frac{\sigma_{tot}}{\nu'^2-\nu^2}\nu'^2 d\nu' \\ &= \frac{1}{2\pi^2}\,\mathcal{P}\int_0^{+\infty}\left(1+\frac{\nu^2}{\nu'^2}+...\right)\sigma_{tot}d\nu' \end{aligned} \tag{2.24}$$

$$\begin{aligned} Re f_2(\nu) &= -\frac{1}{4\pi^2}\,\mathcal{P}\int_0^{+\infty}\frac{(\sigma_{3/2}-\sigma_{1/2})}{\nu'^2-\nu^2}\nu\nu' d\nu' \\ &= -\frac{1}{4\pi^2}\,\mathcal{P}\int_0^{+\infty}(\sigma_{3/2}-\sigma_{1/2})\left(\frac{\nu}{\nu'}+\frac{\nu^3}{\nu'^3}+...\right)d\nu' \end{aligned} \tag{2.25}$$

No-subtraction Hypothesis

Comparing the first order terms of Eq.(2.22) and Eq.(2.24) for the spin independent amplitude f_1 the following relation is obtained:

$$f_1(\nu=0) = \frac{1}{2\pi^2}\,\mathcal{P}\int_0^{+\infty}\sigma_{tot}(\nu')d\nu' = -\frac{\alpha}{m} \tag{2.26}$$

This relation gives a contradiction since the total cross section in the left hand side is a positive quantity and the right part of the equation is negative. This is due to the fact that σ_{tot} is an increasing function of the photon energy at high energies [24] and this makes not converge the first term in the integrand of Eq.(2.24). Therefore, for the convergence of f_1 at least one subtraction is needed:

$$\begin{aligned} Re f_1(\nu) - Re f_1(\nu=0) &= -\frac{\alpha}{m} + \frac{1}{2\pi^2}\,\mathcal{P}\int_0^{+\infty}\frac{\sigma_{tot}(\nu')}{\nu'^2-\nu^2}\nu'^2 d\nu' \\ &= \frac{1}{2\pi^2}\,\mathcal{P}\int_0^{+\infty}\sigma_{tot}(\nu')\left(\frac{\nu^2}{\nu'^2}+\mathcal{O}(\nu^4)\right)d\nu' \end{aligned} \tag{2.27}$$

The necessity for subtraction in the f_1 dispersion relation can also be demonstrated in the Regge poles model [25]. In this approach the cross section at high photon energies ν can be described by

$$\sigma \sim \nu^{\alpha(0)-1} \tag{2.28}$$

where $\alpha(0)$ is the intercept of the leading Regge trajectory. For the total unpolarised cross section this is the Pomeron trajectory with intercept $\alpha(0) = 1.08$. Combining Eq.(2.26) and Eq.(2.28) one obtains:

$$f_1(\nu = 0) \sim \int_0^{+\infty} \sigma_{tot} d\nu \sim \int_0^{+\infty} \nu^{0.08} d\nu \tag{2.29}$$

which diverges for $\nu \to \infty$. Therefore, one subtraction has to be done in order to insure a better convergence. In the case of f_2 the integrand $(\sigma_{3/2} - \sigma_{1/2})$ can be either positive or negative, so there is no direct evidence that the integral does not converge. In the derivation of the GDH sume rule it is assumed that this integrand converges, so that no subtraction is needed in the dispersion relation and a Regge approach [26] confirms that the integral has a convergent behaviour.

2.1.5 GDH Sum Rule

Making a no subtraction assumption for f_2 and comparing the different order terms of Eq.(2.25) and Eq.(2.23) one obtains the GDH sum rule for a spin 1/2 target:

$$I_{GDH} = \int_0^{\infty} \frac{\sigma_{3/2}(\nu') - \sigma_{1/2}(\nu')}{\nu'} d\nu' = \frac{2\pi^2\alpha}{m^2}\kappa^2 \tag{2.30}$$

and the forward spin polarisability γ_0 [27]:

$$\gamma_0 = \int_0^{\infty} \frac{\sigma_{3/2}(\nu') - \sigma_{1/2}(\nu')}{\nu'^3} d\nu'. \tag{2.31}$$

2.2 Generalised GDH Sum Rule

The GDH sum rule can be generalised to include an arbitrary Q^2 dependence and to extend the integral to the case of the absoption of circularly polarised virtual photons in electron scattering. Many different approaches have been proposed. The first GDH integral extension was proposed in 1989 by Anselmino et al. [28] as an attempt to solve the spin crisis where the GDH was used to estimate the higher twist corrections to the DIS experiments. Burkert, Li and Ioffe [29], [30], [31] added the resonances to the model. Other authors tried to extend the GDH using Chiral Perturbation Theory (Ch.P.T) [32],

the Buckhardt-Cottingham sum rule [33], [34] a multipole analysis [35] or the Constituent Quark Model framework [36]. The most straightforward approach is to replace the real-photon cross sections with the corresponding transverse virtual photon cross sections:

$$I(Q^2) = \int_{\nu_{th}}^{\infty} \frac{\sigma_{3/2}^T(\nu, Q^2) - \sigma_{1/2}^T(\nu, Q^2)}{\nu} d\nu \approx 2 \int_{\nu_{th}}^{\infty} \frac{\sigma^{TT}(\nu, Q^2)}{\nu} d\nu \tag{2.32}$$

This equation can be writen in terms of the two nucleon polarised structure functions $G_1(\nu, Q^2)$ and $G_2(\nu, Q^2)$:

$$I(Q^2) = 8\pi^2 \alpha \int_{\nu_{th}}^{\infty} \frac{M\nu G_1(\nu, Q^2) - Q^2 G_2(\nu, Q^2)}{K(\nu, Q^2)} \frac{d\nu}{\nu} \tag{2.33}$$

where $K(\nu, Q^2)$ is a virtual photon flux factor and α is the electromagnetic coupling constant. The contribution of $G_2(\nu, Q^2)$ to the integral vanishes as Q^2 goes to zero and in the limit of deep inelastic scattering. Anselmino et al. [37] pointed out that the generalised GDH sum can be expressed by the first moment of the spin structure function $g_1(\nu, Q^2)$ in the DIS limit:

$$I(Q^2) = m \int_{\frac{Q^2}{2m}}^{\infty} \frac{g_1(\nu, Q^2)}{\nu^2} d\nu \tag{2.34}$$

As Q^2 and ν go to infinity, g_1 becomes a function only of x ($x = \frac{Q^2}{2m\nu}$ is the Bjorken scaling variable). Therefore, changing the integration variable from ν to x yields the generalised GDH integral:

$$I(Q^2) = \frac{2m^2}{Q^2} \int_0^1 g_1(x, Q^2) dx. \tag{2.35}$$

Phenomenological models have been proposed to extend the GDH sum rule integral for the proton and neutron to finite Q^2. Recently, Ji and Osborn [38] derived a sum rule generalisation that is valid at all Q^2:

$$\int_{\nu_{el}}^{\infty} \frac{G_1(\nu, Q^2)}{\nu} d\nu = \frac{S_1(Q^2)}{4} \tag{2.36}$$

where $S_1(Q^2)$ is the spin-dependent forward virtual Compton scattering amplitude. $G_1(\nu, Q^2)$ is one of the nucleon spin structure functions, and it can be measured experimentally.
One limiting case of Eq.(2.36) at $Q^2 = \infty$ is the Bjorken sum rule [8] for the isovector combination proton minus neutron:

$$\int_0^1 (g_1^p(x, Q^2) - g_1^n(x, Q^2)) dx = \frac{1}{6} \frac{g_A}{g_V} \left(1 - \frac{\alpha_s(Q^2)}{\pi}\right) \tag{2.37}$$

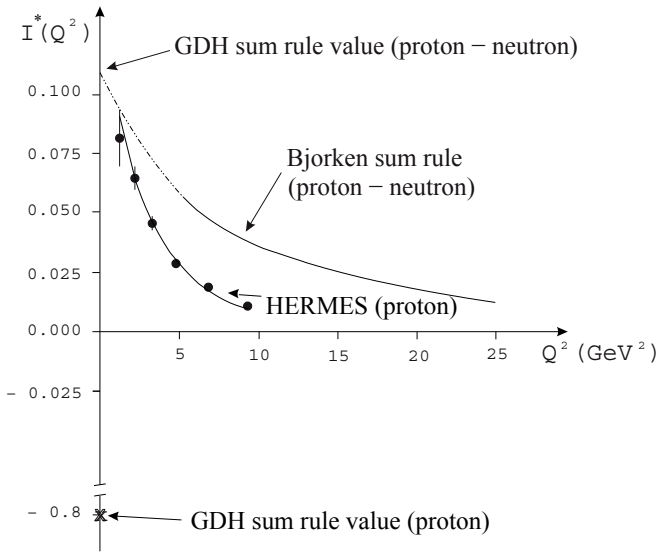

Figure 2.3: HERMES data on the proton for the generalised GDH integral.

where g_A and g_V are the axial and vector coupling constants of the weak interaction, respectively [39], [40], and $\alpha_s(Q^2)$ is the strong coupling constant [13], [41].
On the other hand, in the case of real photons where $Q^2 = 0$, the GDH sum rule predicts:

$$I(0) = -\frac{m^2}{8\pi^2\alpha}\int_0^\infty \frac{\sigma_{3/2} - \sigma_{1/2}}{\nu} d\nu = -\frac{\kappa^2}{4} \tag{2.38}$$

For the proton and neutron this integral takes the following values:

$$I_p(0) = -\frac{\kappa_p^2}{4} = -0.804; \qquad I_n(0) = -\frac{\kappa_n^2}{4} = -0.912; \tag{2.39}$$

and the difference gives:

$$I_{p-n}(0) = I_p(0) - I_n(0) = 0.112 \tag{2.40}$$

Appart from the two limiting cases ($Q^2 = 0$ and $Q^2 = \infty$), $S_1(Q^2)$ can be calculated at small Q^2 (where hadronic degrees of freedom dominate) using Chiral Perturbation Theory and at large Q^2 (where quarks and gluons (partons) are the relevant degrees of freedom) with twist expansions and lattice QCD.

Several experiments have been performed in order to determine the value of $I(Q^2)$ at different Q^2 points. Fig. 2.3 summarizes the different experimental and theoretical determinations of $I(Q^2)$ for the proton and the isovector combination proton-neutron. The data agree on a positive value for the generalised GDH integral, at least down to $Q^2 \sim 1.0 GeV^2$.

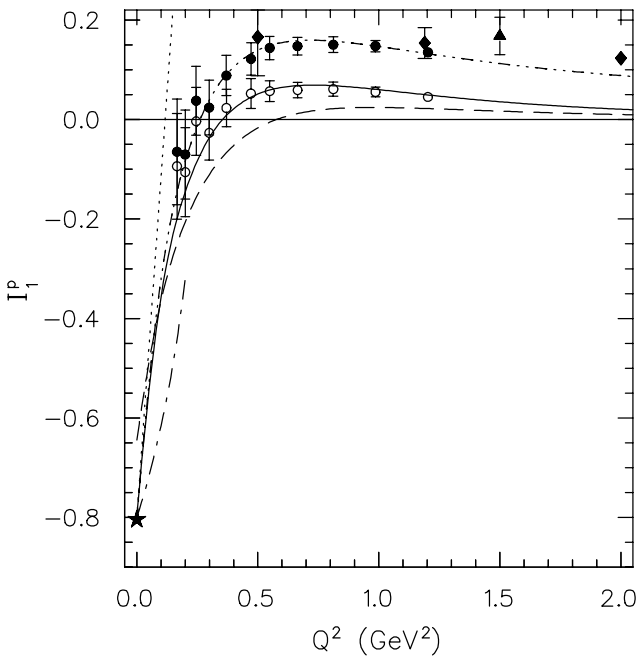

Figure 2.4: Q^2 dependence of the integral I_p. The open circles show the resonance contribution ($W < 0.2$ GeV), the solid symbols also include the DIS contribution. The data are from Fatemi et al. (2003), CLAS Collaboration (circles), Abe et al. (1998), SLAC (diamonds), and Airapetian et al. (2003), HERMES (triangles). Full line: MAID including all channels up to W = 2 GeV, dashed line: one-pion channel only, dotted $O(p^4)$ prediction of HBChPT (Ji et al., 2000), dash-dotted: relativistic baryon ChPT (Bernard et al., 2002b, 2003), dashed-dot-dotted: interpolating formula of Anselmino et al., (1989), asterisk: sum rule value at $Q^2 = 0$. Figure from Dreschel and Tiator (2004).

The closed circles on the figure are data points from the HERMES experiment on the proton [42]. The Bjorken sum rule prediction for the proton-neutron difference is also shown and seems to extrapolate rather smoothly to the GDH value. In the case of the proton the GDH sum rule value has a different sign from the deep inelastic regime and is in disagreement with what one would expect. A simple extrapolation of the proton curve leads to a positive value at $Q^2 = 0$ which is in contradiction to the negative value predicted by the GDH sum rule. Therefore an experimental check of the GDH sum rule at $Q^2 = 0$ could ascertain this intringuing situation.
Data obtained with the CLAS detector at Jefferson Lab [43] clearly shows the sign change of I_p at $Q^2 \sim 0.3GeV^2$ as it can be seen in Fig. 2.4.

	I_{GDH}^{proton}	$I_{GDH}^{neutron}$
$\gamma N \to N\pi$	172[164]	147[131]
$\gamma N \to N\pi\pi$	94	82
$\gamma N \to N\eta$	-8	-6
$\gamma N \to K\Lambda(\Sigma)$	-4	2
$\gamma N \to N\rho(\omega)$	0	2
Regge contribution ($E_\gamma > 2$ GeV)	-14	20
TOTAL	$\sim$ 239[231]	$\sim$ 247[231]
GDG sum rule	204	233

Table 2.1: Contributions of different partial reaction channels to the GDH sum rule. Predictions for Nπ are from SAID [48] and (within brackets) MAID [49] multipole analysis; estimates for N$\pi\pi$ are from [50]; estimates for Nη are from [49]; kaon channel contributions are from [51]; predictions for vector meson production are from [52]; Regge contributions are from [53].

2.3 Experimental Check of the GDH Sum Rule

The first experimental check of the GDH sum rule was the measurements of I_{GDH}^{p} that was jointly perfomed at two laboratories located in Germany: the microtron accelerator facility MAMI in Mainz [44], [45] in the photon energy range 150 MeV $< E_\gamma <$ 800 MeV and the electron synchrotron ELSA in Bonn [46] in the photon energy range 500 MeV $< E_\gamma <$ 2.9 GeV. The combined result of these two experiments with the theoretical estimates for the unmeasured energy ranges (see Table 2.1 [47]) supports the validity of the GDH sum rule for the proton.

In Table 2.2 are shown the current theoretical estimates of the GDH sum rule values for the proton and the neutron. These estimates disagree with the GDH sum rule predictions for the proton while they roughly reproduce the neutron GDH value. However, the (proton-neutron) difference has a different sign with respect to the GDH expectations. The main reason of this discrepancy is the oscillating photon-energy dependence of the GDH integrand due to multipole contributions of alternating sign. Therefore, a reliable prediction requires a very high accuracy that has not been reached by any of the existing models.

For this, a sytematic study of the GDH sum rule for both the neutron and proton as well as a precise double polarisation measurement for all $\gamma N \to N\pi(\pi)$ channels, which give the dominant contribution to the GDH integral, are needed to pin down the reasons of this discrepancy.

$E_\gamma(MeV)$	I_{GDH}^{proton}
≤ 0.2	-28.5 ± 2
0.2-0.8 (measured)	226 ± 5 ± 12
0.8-2.9 (measured)	27.5 ± 2 ± 1.2
≥ 2.9	-14 ± 2
TOTAL	211 ± 5 ± 12
GDG sum rule	204

Table 2.2: Contributions (in μb) of several energy regions to the GDH integral I_{GDH}^{p} on the proton. The contribution for $E_\gamma < 0.2$ GeV is from MAID [49] multipole analysis with an error estimated by a comparison with SAID [48]. The asymptotic contribution ($E_\gamma > 2.9$ GeV) is from [53] with an error estimated by a comparison with a similar approach [54].

2.4 The GDH Sum Rule on the neutron

Due to the lack of free neutron targets, the experimental verification of the GDH sum rule for the neutron has to be performed using a polarised deuteron or ^{3}He target. In the case of the deuteron, the proton and the neutron are essentially in s states of relative motion with aligned spins, while ^{3}He is a two spin paired proton system with an unpaired neutron, also in relative s states. As it can be seen in Table 2.3:

$$\mu_d \approx \mu_p + \mu_n \qquad ; \qquad \mu_{^3He} \approx \mu_n$$

so, the most accurate evaluation of the GDH integral for the neutron is obtained from ^{3}He, since the proton contribution to the measured helicity dependent yields, is smaller than in the deuteron case and the ^{3}He spin structure function is much closer to the free neutron.
However, ^{3}He or deuterium are not only interesting as a neutron substitute. In fact, the GDH sum rule is valid for any system (nucleus, atom, molecule, etc) which has non-zero spin [18]. In this case, the sume rule can be written as follows:

$$\int_{\nu_{th}}^{\infty} \frac{\sigma_p - \sigma_a}{\nu} d\nu = 4\pi^2 S \left(\frac{1}{S}\mu - \frac{Q}{M}\right)^2 \tag{2.41}$$

where ν_{th} is the photodisintegration threshold, μ is the total magnetic moment of the considered system and Q, M and S are its charge, mass and spin respectively.
The expected contribution for the GDH sum rule on the neutron from the pion production threshold to ∞ is 233 μb. Since the ^{3}He spin structure is very similar to the neutron, one would naively expect to have approximately also the same value for I_{GDH}. However, from Table 2.3 it can be clearly seen that I_{GDH} for the ^{3}He is more than a factor of two larger.

Therefore, the contribution from the two-body breakup to the pion production threshold is necessarily quite large in order to satisfy the ^{3}He predicted value of 498 μb.
Investigations of the neutron using polarised ^{3}He are suitable at MAMI beyond the pion

	p	n	d	^{3}He
μ	2.79	-1.91	0.86	-2.13
κ	1.79	-1.92	-0.14	-8.37
I_{GDH}	204	233	0.65	498

Table 2.3: Magnetic moment μ (in units of the nuclear magneton μ_N), anomalous magnetic moment κ, and GDH sum rule I_{GDH} in units of μb for the proton, neutron, deuteron and ^{3}He nuclei.

production region. For lower energies is planned at the new upgraded HIγS facility of the TUNL laboratory (Durham NC, USA) [55] a measurement of the $I^{^3He}_{GDH}$ from the break-up threshold region up to around 60 MeV. The results obtained from both measurements will provide a valuable information to better understand the GDH sum rule integrand for the ^{3}He and from this to extract the neutron information.

2.5 Pion Photoproduction Multipole Analysis

Apart from the contribution to the GDH sum rule, the study of the helicity dependence of single and double pion production channels provides an important information on partial wave amplitudes. In the partial wave and isobar-model analysis, the physical observables are written in terms of the helicity amplitudes that are in turn written as partial wave expansions of electromagnetic multipoles. The strength of the various multipoles that contribute to the studied process can be obtained by parameterising the amplitudes fitted to the experimental data. Specific nucleon resonances are then related to the specific multipoles and the knowledge of the different multipoles allows to pin down the resonance contributions and characteristics. The study of these excited states is an important aspect in the understanding of the nucleon structure.
In the MAMI energy range that was used in the measurement performed in this work, the resonances that contribute with a resonable strength are $P_{33}(1232)$, $P_{11}(1440)$, $D_{13}(1520)$ and $S_{11}(1535)$. Their peak position, width and relative strength are shown in Fig. 2.5. The Δ-resonance ($P_{33}(1232)$) is the most important in the first resonance region (excitation energies below ∼500 MeV) while the D_{13} state is the dominating one in the second resonance region (excitation energies from ∼500 MeV to ∼1 GeV), with overlapping smaller contributions from P_{11} and S_{11} as it can be seen in Fig. 2.6.
The correspondance between electromagnetic pion multipoles and resonances for the first

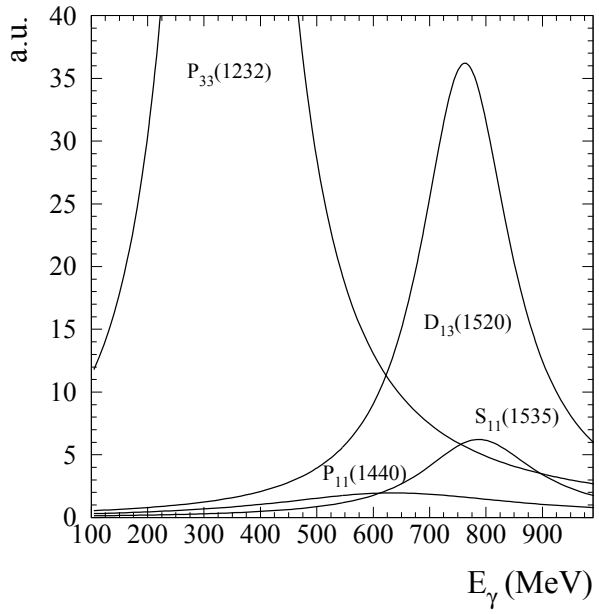

Figure 2.5: Contribution of the nucleon resonances to the γN $\rightarrow$ πN total cross section for exitation energies below 1 GeV taken from the MAID analysis [49], [56].

excited states is shown in Table 2.4.

Up to now, the determination of the multipoles has been estimated using mostly the unpolarised data from single pion photoproduction reactions on the proton. However, for the nπ^0 channel there is a small amount of available data even in the unpolarised case. Therefore, the measurement of new data will provide a complete characterisation of the different isospin components of the multipole amplitudes and a better access to some resonant states. In Fig. 2.7 and 2.8., the MAID07 predictions for the helicity asymmetry of the partial channels γp $\rightarrow$ pπ^0 and γn $\rightarrow$ nπ^0 are shown displayed as a function of the photon energy at $\theta_{cms} = 90^\circ$ and $\theta_{cms} = 120^\circ$ respectively. The standard MAID07 solution is represented by the filled squares while the other curves are solutions in which the coupling constant of a specific resonance state was set to zero. As one can see in these figures, the difference between these models is an evidence of the sensitivity of these observables to the different resonances.

This fact strongly motivates further theoretical and experimental research in this field. In particular, additional single pion photoproduction channels, even in the Δ-resonance region, need to be measured in order to perform a reliable isospin decomposition of the different multipoles. Due to the large branching decay ratios of the higher resonances

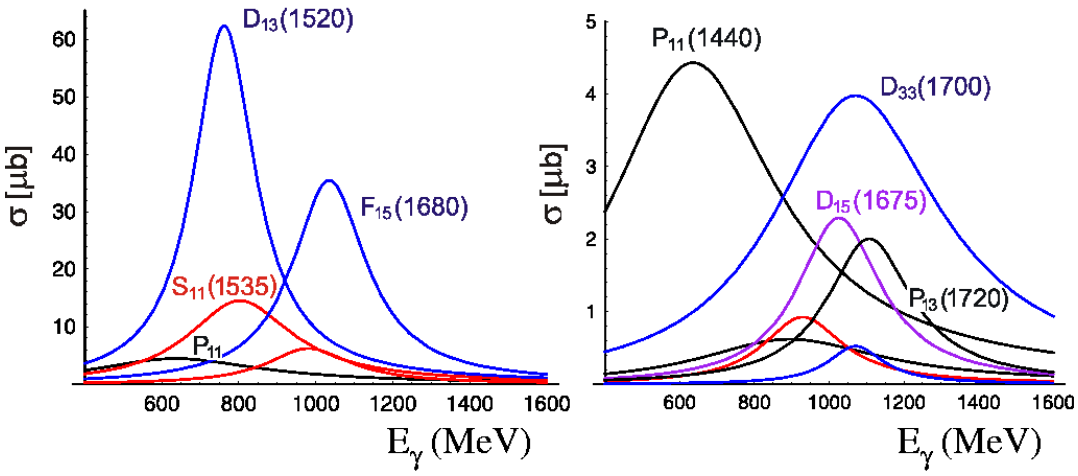

Figure 2.6: Contribution of the nucleon resonances to the γN $\rightarrow$ πN total cross section for exitation energies between 500 MeV and 1.6 GeV taken from the MAID analysis[49], [56].

into $\pi\pi$N and ηN channels, also precise measurements of these reactions, using different polarisation observables, will provide additional and complementary information on the different baryon resonances. This partial channel study will be performed at the Mainz MAMI tagged photon facility using a deuterated butanol target, due to the higher luminosity that can be reached. However, in the Δ resonance region, where the cross section is higher, reasonable precision can be obtained with a polarised ^{3}He gas target. Since nuclear effects are most important, the comparison between the results from deuterium and ^{3}He will further constrain the nuclear models that are needed for the evaluation of the free-neutron contribution.

Photon Multipole	Pion Multipole	Resonance
E1	E_{0+}	$S_{11}(1535)$
E1	E_{2-}	$D_{13}(1520)$
M1	M_{1-}	$P_{11}(1440)$
M1	M_{1+}	$P_{33}(1232)$
E2	E_{1+}	$P_{33}(1232)$
M2	M_{2-}	$D_{13}(1520)$

Table 2.4: Correspondance between electromagnetic pion multipoles and resonances in γN $\rightarrow$ πN reactions.

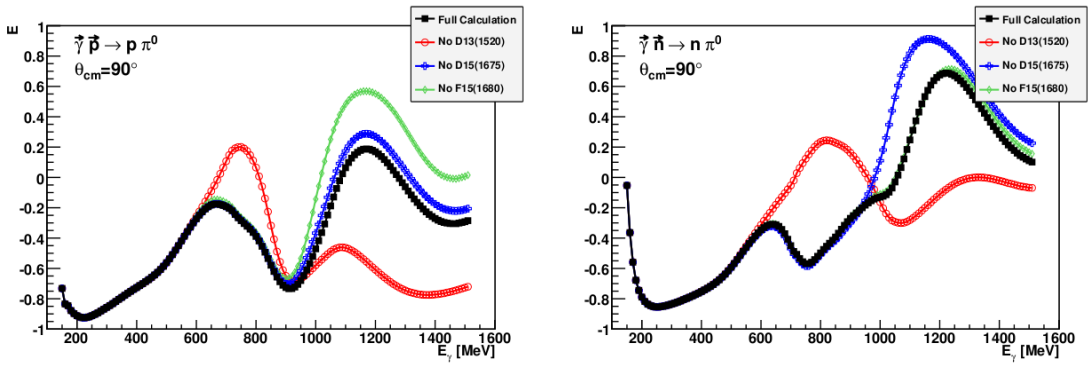

Figure 2.7: Nucleon resonances of the helicity asymmetry E for the $\gamma p \rightarrow p\pi^0$(left) and $\gamma n \rightarrow n\pi^0$(right)reactions at $\theta_{cms} = 90°$ predicted by the MAID07 model.

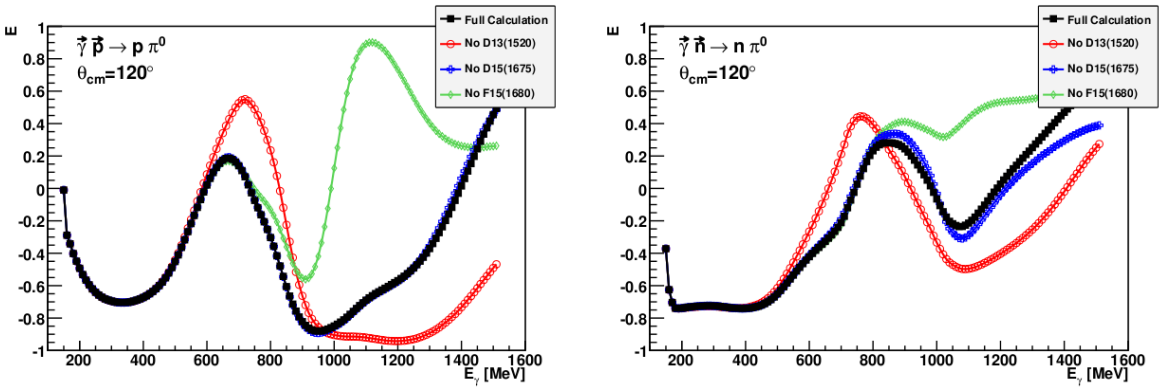

Figure 2.8: Nucleon resonances of the helicity asymmetry E for the $\gamma p \rightarrow p\pi^0$(left) and $\gamma n \rightarrow n\pi^0$(right)reactions at $\theta_{cms} = 120°$ predicted by the MAID07 model.

Chapter 3
Experimental Setup

3.1 Overview

To verify the GDH sum rule, the integral of the polarised total inclusive cross section over the photon energy has to be determined experimentally. This was the major aim of this work and for this an experiment was carried out at the MAMI accelerator facility in 2009. This is the first experiment carried out with a circularly polarised photon beam and a longitudinally polarised ^{3}He target, in the photon energy range from pion photoproduction threshold ($\sim$140 MeV) up to 800 MeV.
In this experiment, the photon beam was produced via bremsstrahlung process in which a thin radiator converted the incoming electron beam into a beam of high energy photons. The energy of the photons was determined with the Mainz-Glasgow tagger spectrometer. Then the photon beam impinged on the polarised target and the reaction products were detected by the central detector system. This detector system was composed by the Crystal Ball multiphoton detector (CB) which provided accurate spectroscopic information over most part of the solid angle, the Multi-Wire Proportional Chambers (MWPCs) used to identify and track the charged particles impinging on CB and the Particle Identification Detector (PID) to distinguish the charged from the neutral particles detected by CB. In addition, the TAPS spectrometer provided information about the particles detected in the forward region outside of the acceptance of the central detector. Finally, a gas Cherenkov counter, placed in front of TAPS, was used to online suppress the electromagnetic background. The complete experimental setup will be presented in more detail in the following sections.

3.2 The Mainz Microtron (MAMI)

The Mainz Microtron MAMI [44], [45] is located in the Institut for Nuclear Physics in Mainz, Germany. The first version of the accelerator, called MAMI-A1, came into oper-

	RTM1	RTM2	RTM3
Input energy (MeV)	3.455	14.35	179.5
Output energy (MeV)	14.35	179.5	854.6
No. of recirculations	18	51	90
Energy gain per recirculations (MeV)	0.599	3.24	7.5

Table 3.1: MAMI race track parameters.

ation in 1979. It consisted of a 3.5 MeV injector linear accelerator (LINAC) and a Race Track Microtron (RTM), producing electrons with an energy up to 14 MeV at a maximum intensity of 25 μA. That machine was upgraded in 1983, MAMI-A2, adding a second microtron accelerating the electrons from 14 MeV up to 183 MeV. In 1991 a third microtron was added and MAMI-B started to operate producing electrons with a maximum energy of 855 MeV. The last upgrade, MAMI-C, was done in 2006. In this new section of the accelerator, the Harmonic Double-Sided Microtron (HDSM) raises the maximum electron beam energy to 1.5 GeV. A complete floorplan of the MAMI facility and the different exerimental halls to which the beam can be delivered is shown in Fig. 3.1. As the measurements performed for this thesis were carrired out using only MAMI-B, in the following only this part of the accelerator will be explained in more detail.

MAMI-B is an electron accelerator which delivers a continuous beam of (un)polarised electrons, with a maximum current of 100 μA. A thermionic source provides 100 KeV unpolarised electrons which pass into 3 successive LINAC sections where they are accelerated up to 3.46 MeV. On the other hand, to create a polarised electron beam, circularly polarised 830 nm laser light from a Titanium-Sapphire laser induces the photoelectric emission of linearly polarised electrons from a strained GaAsP crystal photocathode [57]. The maximum current of the polarised source is 30 μA with a degree of polarisation of around 75%. Once the (un)polarised electron beam leaves the 3.5 MeV LINAC is injected into a cascade of three race-track microtrons.

These RTMs consist of one LINAC section and two large dipole magnets in which the electron beam is deflected by 180° as it is illustrated in Fig. 3.2. After the first injection the electrons are accelerated each time they pass through the LINAC and deflected at each turn by the dipoles. With every recirculation the beam energy increases and consequently also the radius of curvature of the path through the bending magnets as well. After a certain number of turns the beam is extracted and transported to the next RTM. It is possible to select the energy of the beam by extracting the electrons from an intermediate recirculation trajectory in the third microtron (RTM3). With this procedure the beam energy is given by $E = 180 + 2n \cdot 7.5$ MeV, $n = 1, ..., 45$ circulations. In Table 3.1 are shown the main parameters of the three RTMs.

The energy resolution of the microtron has a small variation in the MAMI-B energy

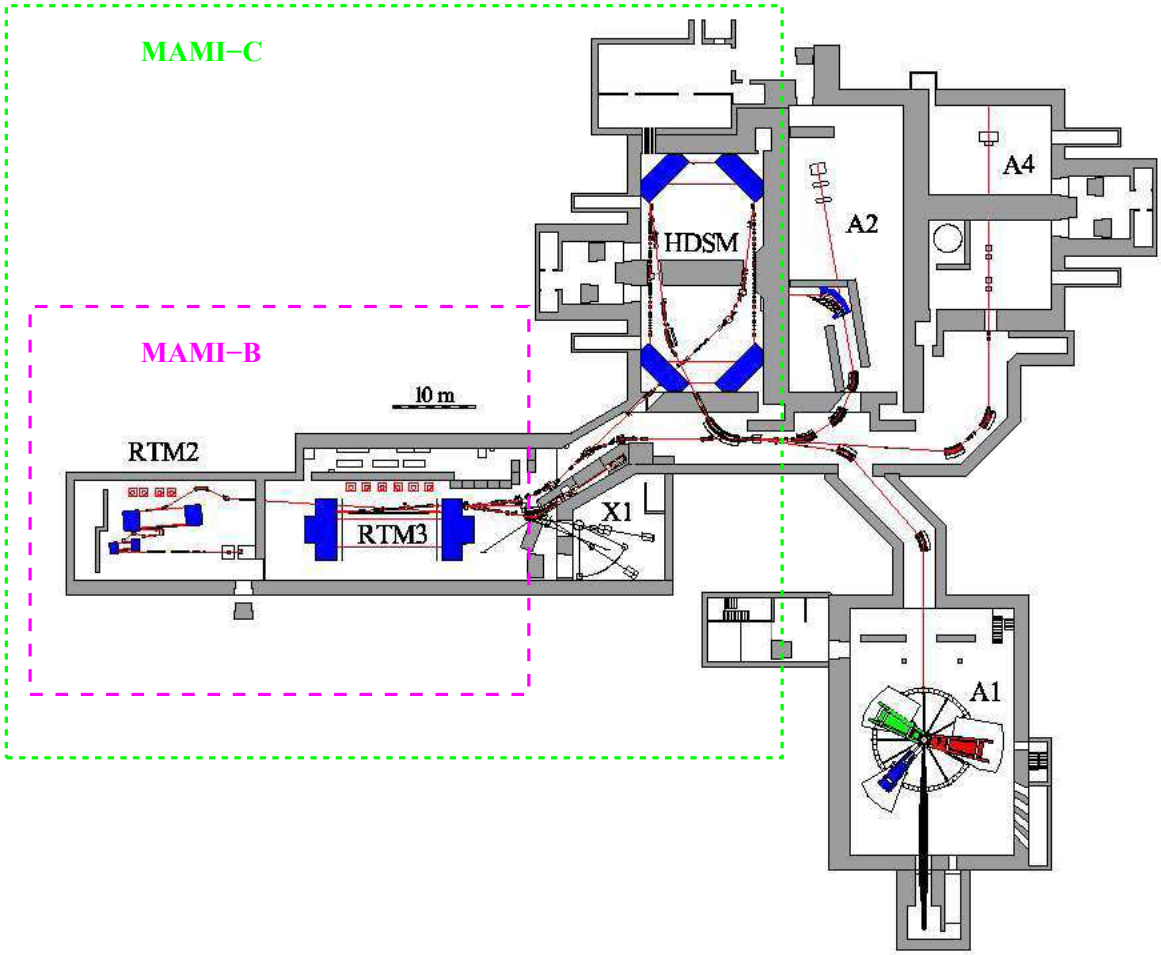

Figure 3.1: Floorplan of the MAMI facility.

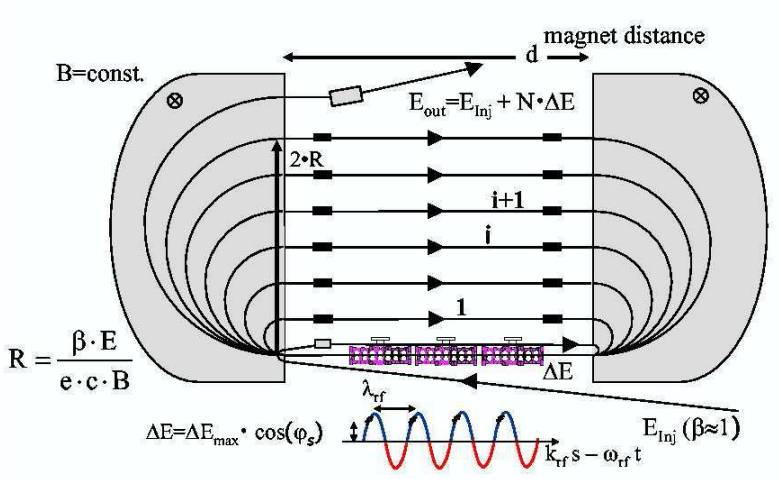

Figure 3.2: Race-Track Microtron schematic view.

(∼ 50 KeV at 855 MeV) mainly due to synchrotron radiation effects. In order to reduce systematic errors originated from fixed beam polarisation the direction of the beam polarisation was switched and monitored every second. Finally, after the extraction from the final microtron and using a series of dipoles and quadrupoles, the beam is delivered to the different experimental halls.

3.3 Photon Beam

3.3.1 Glasgow-Mainz Tagger Spectrometer

The electron beam coming into the A2 hall at MAMI, were this experiment was performed, is converted into a real photon beam when the electrons pass through a thin radiator(∼ 10^{-3} radiation length), producing photons by Bremsstrahlung radiation. The photons produced in this process are then collimated towards the target and the detectors.
In the experiment it is necessary to know the energy of the photons that induces the reaction, therefore the photons were tagged using the Glasgow-Mainz Photon Tagging Spectrometer [58], [59]. The tagger consists of a large bending dipole magnet and the Tagger Ladder, which is a detector system located along the curved focal plane of the tagger magnet (see Fig. 3.3).
After passing through the radiator, the electrons that did not radiate and therefore still have maximum energy, are bent by the ∼ 1 T tagger's magnetic field and dumped into the Faraday cup, which monitored the electron beam current. The electrons that have radiated a photon have less momentum and are bent through larger angles to impinge on

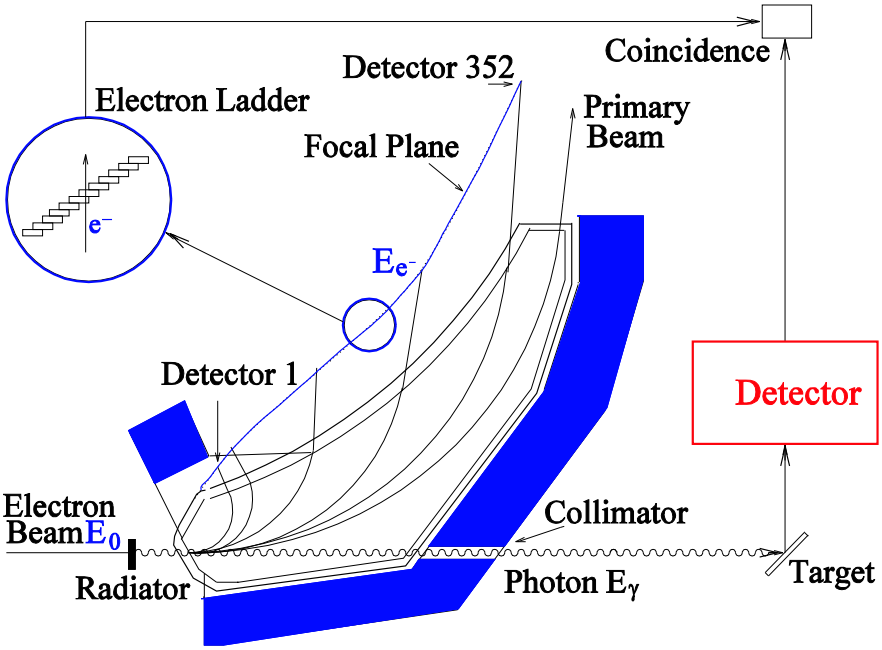

Figure 3.3: The Glasgow-Mainz Tagger.

the focal plane of the tagger system.
The focal plane detector system (FP) [59] consists of 353 plastic scintillators (type NE 111), each approximately 2 cm wide, 8 cm long and 2 mm thick. The plastic scintillators are oriented at $\sim 90°$ to the electron trajectories and the signals of each scintillator are read out by a HamamatsuR1635 photomultiplier tubes. The complete spectrometer tags photons in the energy range 40 to 800 MeV with an energy resolution of ~ 2 MeV at the highest electron beam energies. It operates at a maximum photon flux of $\approx 10^8$ electrons per second. As it is shown in Fig. 3.3, each scintillator overlaps with both of its neighbours, which is used to generate coincidences between them in order to minimise random signals from neutrons, photons or multiply scattered electrons from the primary beam. All events hitting only a single element are rejected. Thus, the photon tagger has a total of 352 coincidence channels. The tagger is calibrated to exactly correlate each tagger signal with the energy of the deflected electron E_{e^-}. Therefore, using energy and momentum conservation, and neglecting the relatively small kinetic energy of the recoiling nucleus (a few keV), the energy of the radiated photon can be calculated as:

$$E_\gamma = E_0 - E_{e^-} \tag{3.1}$$

where E_0 is the energy of the primary electron beam. Fig. 3.4 shows the typical Bremsstrahlung shape of a spectrum as a function of tagger channel and energies. The

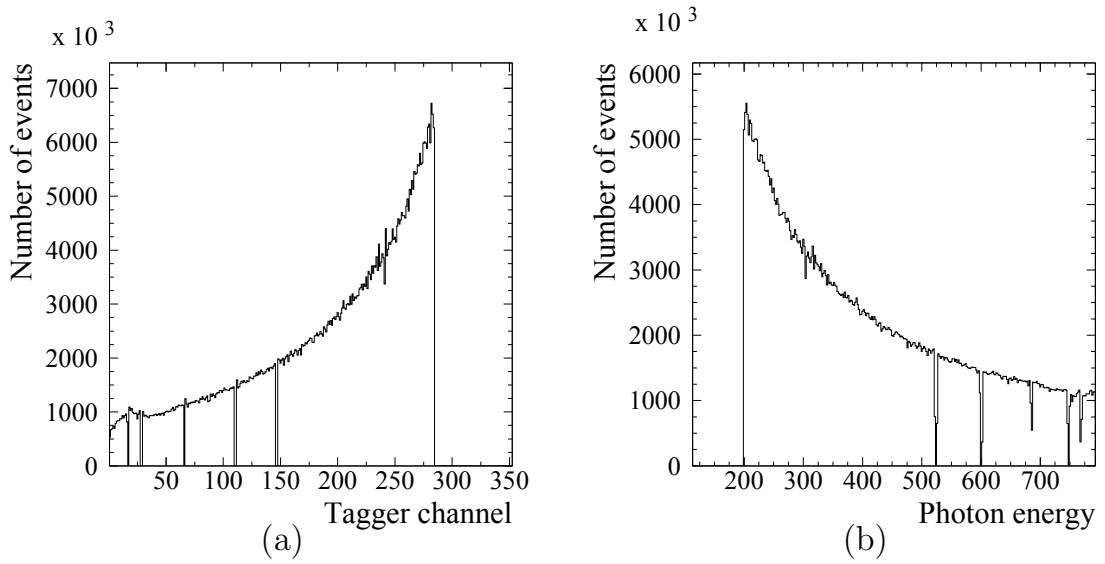

Figure 3.4: Tagger spectrum as a function of tagger channel(a), and as a function of photon energy(b).

highest tagger channel correspond to the highest electron energy which in turn corresponds to the lowest photon energy. In our experiment the tagger was operating with a photon intensity of $\sim 10^7 s^{-1}$.

3.3.2 Photon Flux

In order to obtain a well defined beam spot contained within the target diameter, the photon beam is collimated before leaving the tagger magnet. The collimator consisted of 4 lead cylinders each 20 mm long and with a 3 mm diameter hole bored through the center and aligned on the beam axis. To ensure a precise normalisation of the measured cross sections it is essential to know the number of photons that reach the target. Due to the collimation some of the tagged photons do not reach the experimental area. The photons with a large angle will be stopped in the collimator, since the Bremsstrahlung process is characterised by a polar opening angle, θ_c, which encloses half of the radiated photons. This angle is dependent of the energy of the primary beam, E_0 and can be expressed as:

$$\theta_c = \frac{m_e}{E_0}, \tag{3.2}$$

where m_e is the mass of the electron. The number of tagged photons that reach the target can be determined by the 'tagging efficiency' measurement which for each focal plane detector is defined as:

$$\epsilon_{tagg} = \frac{N_\gamma}{N_e} \tag{3.3}$$

where N_γ is the number of photons hitting the target and N_e is the number of corresponding electrons detected in the tagger focal plane. The tagging efficiency can be ontained using a Pb-Glass detector with $\sim 100\%$ photon detection efficiency. However, this detector can stand a maximum intensity of $10^5\gamma/s$, while during the experiment the required intensity was two orders of magnitude higher. Therefore, a reduced beam current was used during the tagging efficiency measurement in order to protect the detector.

3.3.3 Photon Polarisation

It is necessary to know the real degree of polarisation of the photon beam, since not all the detected events are polarised photons.
The longitudinal polarisation of an electron is converted into circular polarisation of the emitted photon during the Bremsstrahlung process. The fraction of transferred polarisation depends on the electron beam energy E_0 and on the energy of the emitted photon E_γ. If P_γ is the photon polarisation and P_{e^-} is the polarisation of the incoming electron, the ratio for the transfer of polarisation can be written as [60]:

$$\frac{P_\gamma}{P_{e^-}} = \frac{4E_\gamma E_0 - E_\gamma^2}{4E_0^2 - 4E_\gamma E_0 + 3E_\gamma^2} \tag{3.4}$$

The electron polarisation is completely transferred to the photon at $E_\gamma = E_0$, when the entire energy of the electron is transfered to the photon. In order to obtain sufficient data with a relatively high degree of polarisation, two different energy settings for the primary beam were chosen at 525 and 855 MeV. Fig. 3.5 illustrates the energy dependence of the polarisation ratio for these two E_0 settings.
The electron beam polarisation P_{e^-} is measured by means of a Møller polarimeter. The cross section for Møller scattering of longitudinally polarised electrons on the atomic electrons of a magnetised metal foil is polarisation dependent [61]. The polarised Møller cross section can be written as a function of the unpolarised cross section:

$$\left(\frac{d\sigma}{dE_e}\right)^{pol} = \left(\frac{d\sigma}{dE_e}\right)^{unpol} \cdot \left(1 + \sum_{j,k} a_{jk} P_t^j P_e^k\right) \tag{3.5}$$

where P_t^j and P_e^k are the cartesian components of the target foil and electron beam polarisation respectively and $a_{j,k}$ is the analysing power [61] which can be calculated from

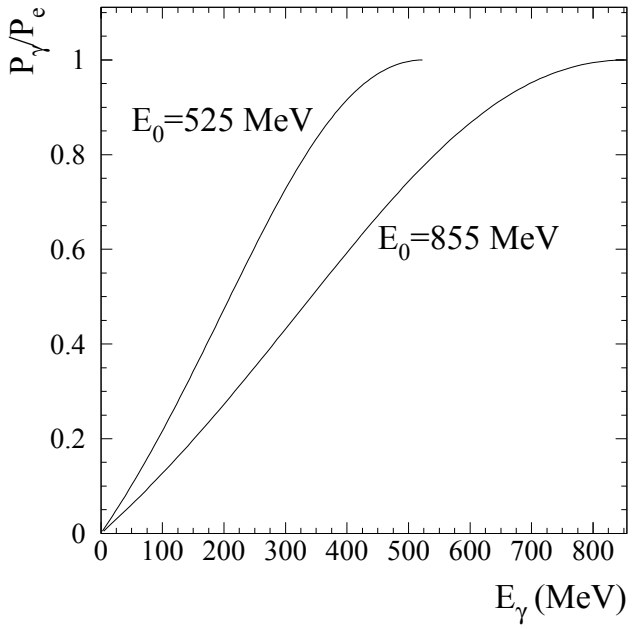

Figure 3.5: Fraction of transferred polarisation from the electron to the photon as a function of the energy for 525 and 855 MeV.

QED [62]. The non-diagonal tensor elements either vanish because of parity conservation or are negligible, therefore the asymmetry can be approximated as:

$$A^{Møller} \approx a_{zz} P_t P_e cos\alpha \tag{3.6}$$

where P_t and P_e are the polarisation degree of the Møller target and the electron beam respectively, α is the angle between these polarisation directions and a_{zz} = -7/9.
The Møller asymmetry can be determined experimentally by detecting the number of events where beam and target have parallel ($N^{\uparrow\uparrow}$) or antiparallel ($N^{\uparrow\downarrow}$) orientation:

$$A^{Møller} = \frac{N^{\uparrow\uparrow} - N^{\uparrow\downarrow}}{N^{\uparrow\uparrow} + N^{\uparrow\downarrow}} \tag{3.7}$$

The tagger spectrometer can be simultaneously used as a polarimeter with a separate electronic chain and read out system [63]. The experimental setup is shown in Fig. 3.6. Two sets of tagger channels are selected to detect electron pairs in coincidence. A good Møller event is the coincidence of two focal plain detectors with the sum of the corresponding electron energies equal to the primary beam energy E_0. The two main sources of background are due to secondary Bremsstrahlung electrons and electrons from pair electroproduction. The electrons produced in the first case are suppressed by time correlation. The electrons

from pair electroproduction are suppresed by demanding coincidences between single tagger channels. By coincidences in these sets of tagger channels the asymmetry $A^{Møller}$ can be measured. This asymmetry is very small (~ 0.02) and statistically significant results of $P_{e^-} \approx 75\%$ could be obtained after 4 hours of measurement.

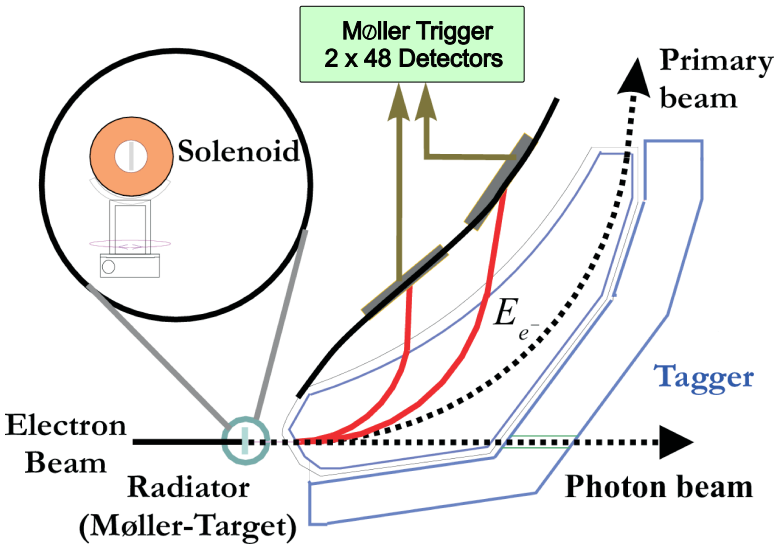

Figure 3.6: The Møller polarimeter.

3.4 The Polarised ^{3}He Gas Target

In this experiment, polarised ^{3}He gas was used as a substitute for a polarised neutron target. The polarised gas was contained in a cylindrical cell with a total length of 20 cm and an outer diameter of 6 cm. The cell material was quartz coated with Cesium vapor and with entry and exit windows for the photon beam. After the polarisation process of the gas, performed in the Institute of Physics, the target cell was brought to the A2 experimental area at MAMI and inserted inside the CB detector, where the polarisation alignement was mantained by a solenoid inside a region with a very low magnetic field gradient. Also a relative measurement of the polarisation was done via NMR techniques every hour. In Fig. 3.7 the ^{3}He setup is shown. The principles of operation for this target, as well as the complete target setup used in the experiment will be described in more detail in chapter 4.

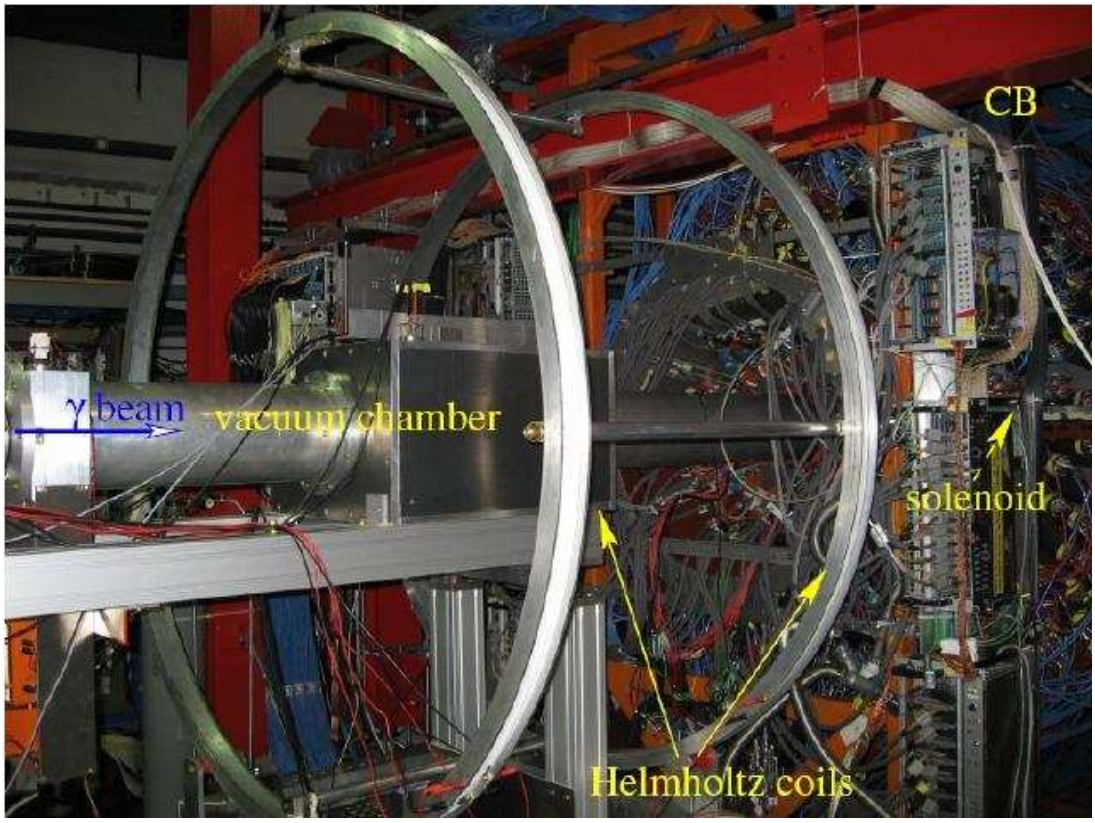

Figure 3.7: ^{3}He experimental setup.

3.5 The Detector Setup

The Crystal Ball detector setup is composed of a NaI spectrometer, two Multi-Wire Proportional Chambers (MWPCs) and a Patricle Identification Detector (PID). The combined information provided by these three detectors provides accurate energy, angle and particle identification in the azimuthal(ϕ) and polar(θ) angle regions from 0° to 360° and 21° to 159° respectively.

The Crystal Ball

The Crystal Ball (CB) was designed in the 1970's and after being in use in many different laboratories arrived to the MAMI facility in Mainz in 2002. The CB is a highly segmented electromagnetic calorimeter and spectrometer that covers 94% of 4π steradians. The geometry of the CB is based on an icosahedron, which has 20 triangular faces (major triangles) divided into 4 smaller triangles. These 4 minor triangles in turn contain

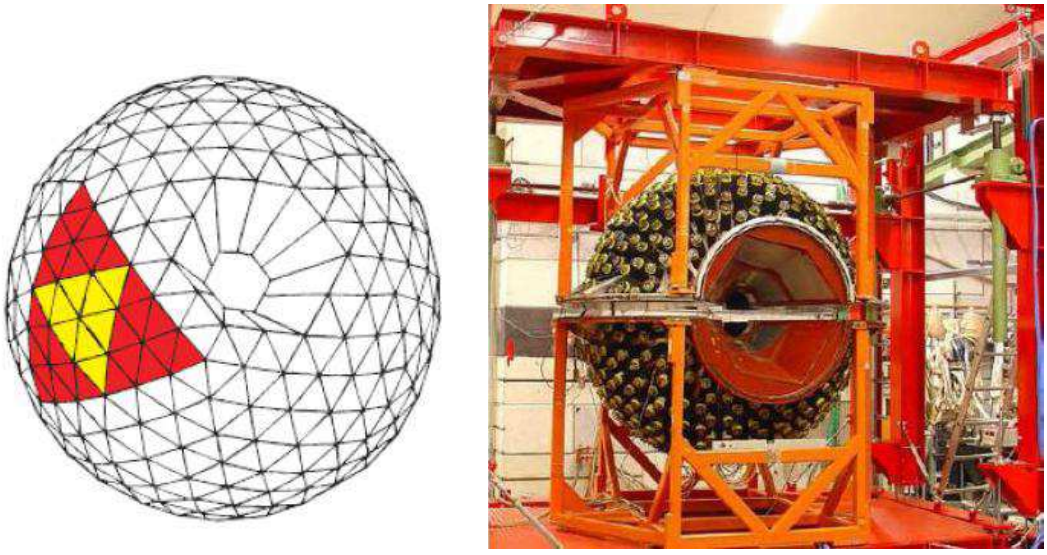

Figure 3.8: Crystal Ball geometry.

9 triangular crystals (see Fig. 3.8). The smallest triangular surface represent the base of a NaI(Tl) crystal shaped like a truncated triangular pyramid. Each crystal is 40.6 cm in length (15.7 radiation lengths), with 12.7 cm length at the inner triangular side and 5.1 cm at the outer surface (see Fig. 3.9). The crystals are aligned in such a way that they point radially outward from the center of CB, with the wider end of the crystal being along the outside of the ball. In this arrangement, a near spherical shell of 720 elements is formed. However, 24 crystals have been removed at both the front and rear part of CB to create a tunnel through the center allowing space for the beam and target holding structures. Thus, the CB has a total of 672 crystals. Each of the crystals is individually wrapped in reflecting paper and aluminised mylar in order to ensure optical isolation. The scintillation light produced in each NaI(Tl) crystal passes through a 5 cm air gap and a glass window before reaching a 5.1 cm diameter and 21 cm long photomultiplier tube (PMT). The spherical cavity in the center of CB has a radius of 25.3 cm and the radius of the outer shell is 66.0 cm. Thus taking into account that the PMTs with base and connectors are about 26 cm long, in total the CB radius is 92 cm.
The CB is divided into two hemispheres whith a weight of around 3 tons each. The hemispheres are separated by a 0.8 cm air gap between two 1.6 mm thick stainless steel disks on which the crystals rest. Along the inner spherical cavity, each hemisphere has a shell of 1.5 mm thick (0.09 radiation lengths) stainless steel. The NaI crystals are extremely hygroscopic, so the hemispheres are hemetically vacuum sealed in order to protect the

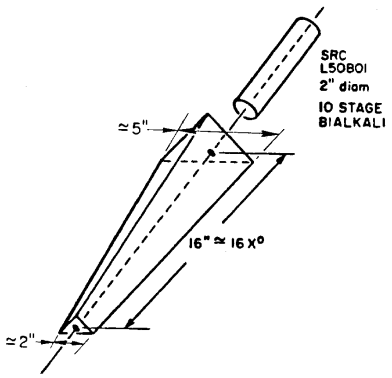

Figure 3.9: NaI(Tl) crystal.

crystals from a possible contact with moisture in the atmosphere. Therefore, the pressure within the steel casing as well as the temperature and humidity are monitored. The mechanical separation of the two hemispheres also allows for easy mounting and maintenance of the targets and detectors in the tunnel region.
For photons up to ∼400 MeV, typically 98% of all the deposited energy from the electromagnetic shower created by a photon is contained in a cluster of 13 crystals. Due to its high degree of segmentation, the CB achives very high angular resolution values in the energy range from 50 MeV to 500 MeV (see Table 3.2). The length of the NaI crystals corresponds to a stopping range of 233 MeV for $\mu^{\pm}$, 240 MeV for $\pi^{\pm}$, 340 MeV for $K^{\pm}$ and 425 MeV for protons. The neutron detection efficiency varies between 10 and 40 % for 50 and 250 MeV neutrons respectively.

Azimuthal angular acceptance	$0° \leq \phi \leq 360°$
Polar angular acceptance	$20° \leq \theta \leq 160°$
Azimuthal angular resolution	$\sigma_\phi = 2°/sin\theta$
Polar angular resolution	$\sigma_\phi = 2° - 3°$
Photon energy resolution	$\frac{\sigma(E)}{E} = 2\%(\frac{E}{GeV})^{-1/4}$
Time resolution	1 ns FWHM, after rise time compensation

Table 3.2: Principal characteristics of Crystal Ball.

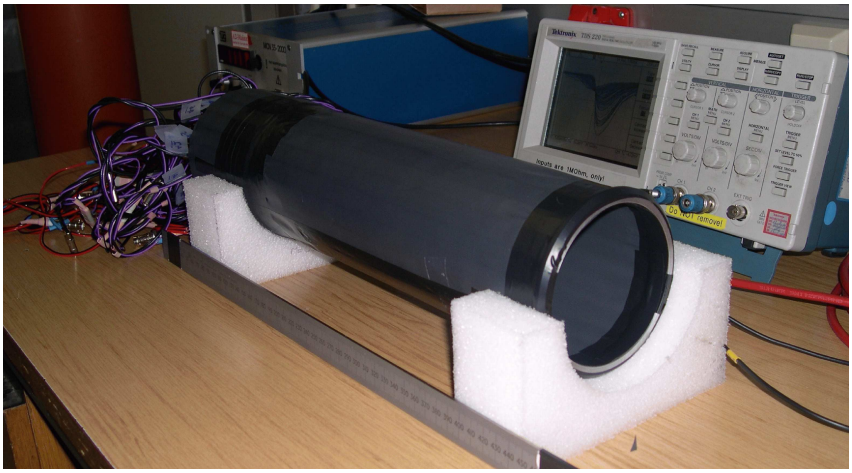

Figure 3.10: The Particle Identification Detector before installation inside the CB.

Particle Identification Detector

The Particle Identification Detector (PID) is a scintillator detector used to distinguish between neutral and charged particles as well as between different charged particles detected by the Crystal Ball. It is located in the tunnel region of the CB. The PID is a ∼10 cm diameter barrel formed by 24 plastic scintillators, cilindrically arranged around the beam axis centered on the target (see Fig. 3.10). The size of each scintillator is 310 mm long, 13 mm wide and 2mm thick.
The EJ204 plastic scintillators are connected to a 24 Hamamatsu R1635 photomultiplier tubes via perspex light guides. The PMTs are affixed to the end of each scintillator, at the downstream end of the CB exit to minimise the length of the light guides. Each scintillator is individually wrapped in aluminised Mylar to ensure light isolation and the entire detector is covered by a black Tedlar (PVF) foil to provide light-proofing as well as structural support and protection for the scintillators. To minimise the loss of information in the gaps between the detector elements from the particles travelling radially out from the target, the profile of each scintillator is a right-angled trapezium.
The length of the scintillators gives a polar angle coverage between 15° and 159° matching the coverage of the Crystal Ball. Also the barrel design of the PID allows for a full 360° coverage of the azimuthal angle.
The PID identifies different particle species by a comparison of the energy deposited in the CB (assumed to be approximately the total energy of the particle) and the energy deposited in the PID scintillators. The lighter particles deposit a smaller fraction of their total energy in the PID, so by matching the energy deposited in the PID (ΔE) with the corresponding energy deposited in the CB (E), it is possible to use the locus of the

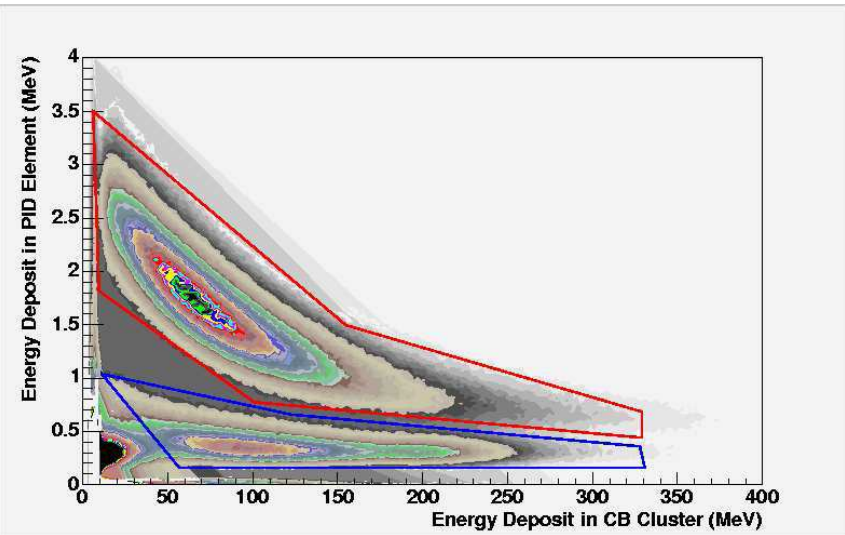

Figure 3.11: ΔE/E plot from the Crystal Ball and the PID. The upper curved region (red band) is the proton locus, the lower region (blue band) contains the charged pions and the the peak near the origin contains mostly electrons.

combination to identify the particle species as shown in Fig. 3.11.

Multi Wire Proportional Chambers

The Crystal Ball segmentation provides position information for photons with a high resolution. This is due to the fact that a given photon triggers several NaI crystals and the energy-weighted mean of their positions locates the photon position better than the crystal pitch. However, for charged particles, which deposit their energy over only one or two crystals, a more precise information can be obtained using two coaxial cylindrical Multi Wire Proportional Chambers (MWPCs) with cathode strip read out.
These MWPCs surround the PID and are similar to those originally used as part of DAPHNE (Detecteur a grande Acceptance pour la PHysique photoNucleaire Experimentale) [64]. With this detector system, the tracks of charged particles emitted within the angular and momentum acceptance of the CB are reconstructed.
Each of the MWPCs consist of three layers: internal strips, wires and external strips (see Fig. 3.12). The inner and outer layers act as cathodes for the proportional counter and are made from 1mm thick cylindrical Rohacell [65] walls covered by a 25μm Kapton foil. Electrical screening is achieved via a 0.1µm thick Aluminium coating on the external surfaces of the chamber walls. Both interior surfaces are laminated with 4 mm wide aluminium strips of 0.1µm thickness with a 0.5 mm gap between adjacent strips. These

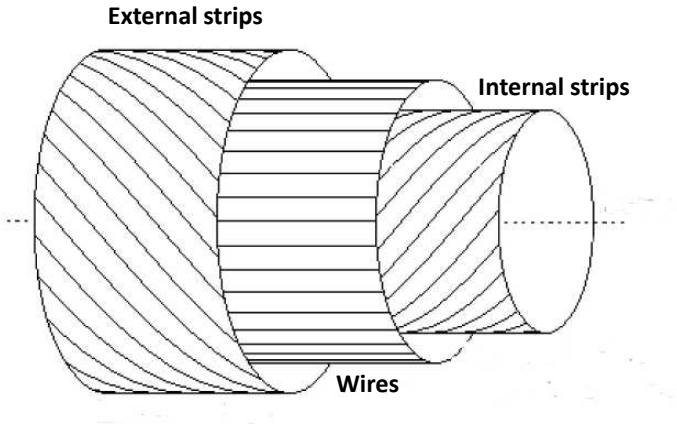

Figure 3.12: Multi Wire Proportional Chamber(MWPC) diagram showing relative positions of anode wires and cathode winding.

cathode strips are wound helicoidally in opposite directions, at angles of ± 45° with respect to the cylinder axis (wires). Each of the inner and outer cathode strips cross each other twice along the length of the chamber and it is necessary to establish which anode wires have also fired to identify the correct intersection point. The anode is composed of 20 μm Tungsten wires arranged parallel to the cylinder axis and separated by 2 mm. The anode is placed in between the two cathode strip walls and separated from them by 4 mm gaps. The geometrical parameters of the MWPCs are given in Table 3.3.
The MWPCs are filled with a gas mixture of argon (79.5%), ethane (30%) and freon-CF4

MWPC	1	2
Length (mm)	560	560
Internal radius (mm)	70	90
External radius (mm)	78	98
Number of wires	232	296
Number of internal strips	69	89
Number of external strips	77	97

Table 3.3: Geometrical parameters of the MWPCs.

(0.5%). This mixture is a compromise between charge multiplication and localization requirements imposed by the ionizing particle tracks.
A charged particle travelling through the chamber ionizes the gas mixture. The resulting

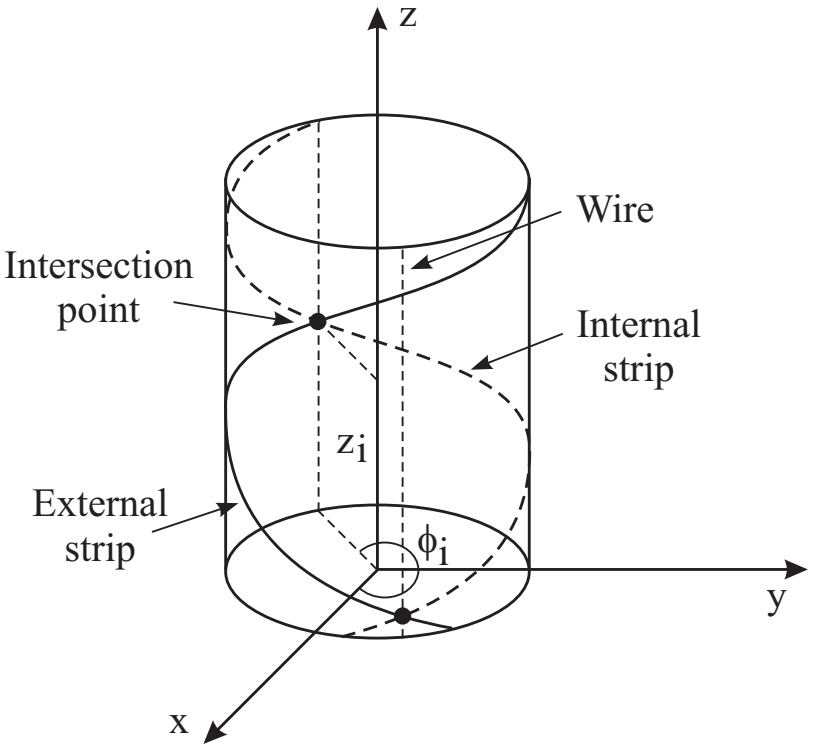

Figure 3.13: Impact reconstruction of a charged particle trajectory in the MWPCs.

ionization electrons move to the anode wire due to the potential difference present between the anode wires and the cathode strips, creating an avalanche of electron-ion pairs on their way by secondary ionization. This avalanche, which is physically collected quasi-punctually on one or more wires, electrostatically induces positive ions on both cathodes, which are accelerated to the internal and external strips. From the center of gravity of the charge distribution induced on the cathode strips of each chamber the azimuthal angle ϕ and the longitudinal coordinate z of the impact point are evaluated. Fig. 3.13, illustrates how ϕ and z are defined. There are two possibilities for ϕ and z, since the internal and external strips overlap twice and the wires are read just as a hit-or-miss signal. The point of intersection of the particle's trajectory with the surface of the cylinder can be accurately determined by correlating the information extracted from the two cathode planes with the anode information.

Since the chambers are operating in proportional mode the charges created by the secondary ionization are proportional to the charges created by the original traversing particle. Once ϕ and z are obtained for each chamber, a straight line can be fitted to these

coordinates and the polar angle θ and azimuthal angle ϕ of the track are obtained. The vertex reconstruction for two or more charged tracks is done by tracking the intersection point of the trajectories. In the case of only one trajectory, the vertex position is defined as the closest point to the z-axis.
Due to the cylindrical symmetry of the wire chambers, they cover 360° in ϕ. The θ range is from 21° to 159° because of the openings at the front and rear of the cylinders, giving a coverage of 94% of 4π steradians.
The precision of the MWPCs is angle dependent and the expected angular resolution (rms) is approx $\approx 2°$ in the polar emission angle θ and $\approx 3°$ in the azimuthal emission angle ϕ.
In order to correct for the loss of particle tracks the global MWPCs track reconstructing efficiency should be determined. This efficiency depends not only on the number of tracks detected, but also on the target type and the identified particles, and can be determined from experimental data.

3.6 Cherenkov Detector

3.6.1 Introduction

There is a huge amount of background originated from electromagnetic reactions inside the target. Incoming photons interact with the target material and the detector parts and induce pair production of electrons and positrons in the Coulomb field of the atomic nuclei and Compton scattering at forward angles. The reaction products, i.e, electrons and positrons, then enter the forward detector and give rise to useless trigger signals. Thus, in order to suppress this background as much as possible a threshold Cherenkov detector was installed. The detector was located between the CB and the TAPS detector to cover the angular polar region from 0° to 18°, where practically all electromagnetic events take place.
The main principle of this detector and its different components are explained below, as well as the efficiency test carried out in a dedicated beamtime measurement.

3.6.2 Principle

Cherenkov light is emitted by a charged particle travelling through a medium at a velocity exceeding the velocity of light in that medium. This light is emitted in a direction at a specific angle θ with respect to the direction of the particle. The angle of the emitted light depends on the particles velocity v and on the refractive index n of the traversed medium:

$$cos(\theta) = \frac{1}{\beta n} \tag{3.8}$$

with $\beta = \frac{v}{c}$ (where c is the speed of light in vacuum). The refractive index n determines the speed of light in the material and hence, the minimum velocity ($\frac{c}{n}$) at which the particle should travel to emit the Cherenkov light. Thus, from the threshold $\beta_t = \frac{1}{n}$ the Cherenkov effect will occur. The corresponding threshold Lorentz factor γ_t can be written as:

$$\gamma_t = \sqrt{\frac{1}{1-\beta_t^2}} = \sqrt{\frac{n^2}{n^2-1}} \tag{3.9}$$

The threshold can also be expressed as a function of the energy of the particle and its rest mass m_0 as:

$$E_t = \gamma_t \cdot (m_0 c^2) \tag{3.10}$$

where it is shown that lighter particles will have a lower energy threshold.
The threshold Cherenkov detector detects all particles that exceed their Cherenkov energy threshold. However, there is no distinction between the different particles, thus it can be used to suppress a certain type of particle if there are no other particles with a Cherenkov threshold in the measured energy range. In our case it is used to get a signal from electrons/positrons for their on-line suppression. This type of Cherenkov detector usually contains a radiator, a mirror and a photomultiplier as it will be discussed in the next section.

3.6.3 Components

The Cherenkov detector is mainly composed by three different elements: a gas volume, a mirror and a photomultiplier tube (PMT). The gas volume is enclosed in a hermetically sealed aluminium casing which has an entrance and exit window on the front and the back covers of the detector respectively. Both windows consist of a mylar foil of 100 μm thickness and a TEDLAR-PVF foil which are light and gas tight.
In order to use part of the space inside the downstream side of the CB tunnel region, the gas Cherenkov detector is shaped to fit inside the backward aperture of the CB. A schematic drawing of the detector geometry is shown in Fig. 3.14.
The total volume of this detector is $\approx 1.3\text{m}^3$ and the light emission length along the z(beam)-axis (L_{rad}) is about 70 cm. The produced light is reflected from the mirror and is focused onto the PMT. A black cloth was mounted inside the detector in order to avoid that the light from stray electrons reaches the mirror.
The mechanical construction is similar to the threshold Cherenkov used for the previous GDH measurements [66], [67]. The PMT and mirror have been reused for the present detector.

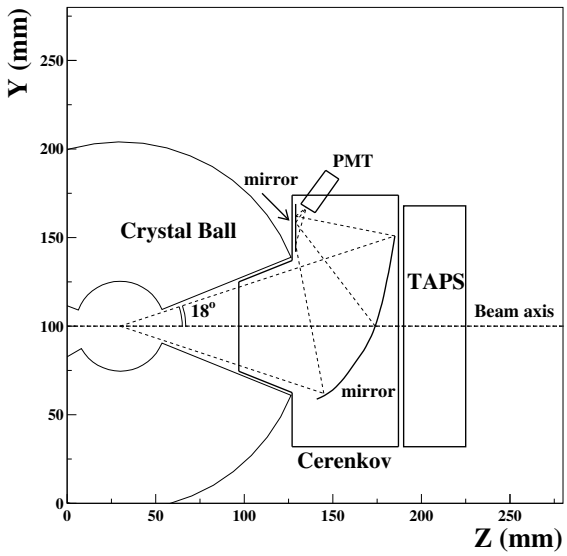

Figure 3.14: Schematic side view of the experimental setup including the Cherenkov detector.

Radiator

The choice of the radiator material used in the Cherenkov detector is dictated by the requirement that electrons and positrons should be detected but not any hadronic reaction products. Since the lightest generated hadron is the pion (m $\approx$ 140 MeV) and the highest possible MAMI beam energy is about 1.5 GeV, it follows that the maximum possible kinetic energy for the pion will be around 1.4 GeV.
Combining formula 3.10 and 3.9 for those pions gives a refractive index n = 1.004 for the radiator medium. The energy threshold for electrons for this radiator is 5.7 MeV. All electrons with an energy below this threshold will not be detected by the Cherenkov detector and consequently will be not vetoed.
A list of different gases with refractive index below 1.004 and threshold energy for electrons and pions for these gases is shown in Table 3.4. The final choice was to use C_4F_8 as radiator gas with n = 1.0013 and 10 MeV Cherenkov light threshold for electrons and 2.7 GeV for pions. This gas also has a good transparency for light in the UV range, where a large part of the Cherenkov radiation is emitted.

Material	Refractive index n	Threshold energy e^{+-} (MeV)	Threshold energy π (GeV)
Air	1.0003	21.9	6.0
N_2	1.0003	20.4	5.7
CO_2	1.0004	17.9	4.9
C_4F_{10}	1.0014	9.7	2.6
C_4F_8	1.0013	10.0	2.7

Table 3.4: Radiator gases.

Mirror

The produced Cherenkov light is collected and focussed by a highly-reflective ellipsoidal mirror onto a photomultiplier tube. The mirror is made out of perspex and has one focus at the assumed target position and the other focus at the photomultiplier. To let the incoming photon pass through the mirror, a 5 cm diameter hole was made in the mirror and covered with a thin highly reflective mylar foil in order to avoid the loss of Cherenkov light.

Photomultiplier tube

The Cherenkov light reflected in the ellipsoidal mirror is focussed into a photomultiplier tube (PMT). An estimate of the position of the focal points of the ellipsoidal mirror can be perforemed based on the geometrical characteristics of the mirror [68]. The first focal point of the mirror was positioned at the target location and the second focal point should be placed at the PMT position in order to collect all the Cherenkov light produced by particles originating from the target.
Since most of the Cherenkov light is emitted in the UV region, a PMT with an entrance window that is transparent for UV light was required. Finally, a Hamamatsu R1584-03 SEL with UV transparent entrance window and a peak quantum efficiency of 26% at 390 nm was chosen as a PMT for the detector. The diameter of the active surface for this PMT is 5 inch (12 cm) and the operating voltage is -2000 V.

Gas system

Prior to the filling of the Cherenkov detector with the C_4F_8 radiator gas, the detector volume was flushed with dry nitrogen gas (N_2) to minimize the presence of air and water vapor. Afterwards, during the filling operation with the C_4F_8, the gas flowed directly from the supply bottle to the detector gas inlet. This gas inlet consists of a tube reaching nearly to the bottom of the detector. Because of the relatively high density of the gas compared

to air or nitrogen, the C_4F_8 pushed the air or nitrogen out of the detector through the outlet located at the top of the detector. This operation was performed at a low flow-rate to prevent too much mixing of the C_4F_8 with the N_2. The outlet valve of the detector was connected to a gas purification system built to recover the C_4F_8 and to remove possible impurities and the air or water from the system. The recycling gas system is graphically depicted in Fig. 3.15.

In the purification process, the gas is sucked from the detector volume with the help of a membran pump (1.5 m^3/h) and it passes through a transparent case filled with silica gel. This material absorbs water and is used as a desiccant (drying agent). It can be used as a monitor since the silica gel changes the color once its saturated with water. The gel can be regenerated by heating it to 120°C for two hours. Then the gas passes a 7 μm filter to remove possible impurities like dust and enters a refrigerator which temperature is -28°C. At this temperature the C_4F_8 gas liquifies. This recovers the pure C_4F_8 and the non-condensable gasses are vented directly to the atmosphere. To re-fill again the detector with the purified gas, the pressure of the C_4F_8 inside the refrigerator should be $\approx$ 2.5 bar. If this pressure is lower than 2 bar, it is possible to achieve this value flowing some N_2 into the cooling unit. Then, once the purified C_4F_8 exits the fridge and is again at atmospheric pressure and temperature, it evaporates and is directed again to the inlet valve of the detector.

Since it is very important to control and monitor the pressure and flow of the gas at any point of the system, and specially inside the detector, some monitoring equipment was implemented to the detector system. The pressure of the gas at the entrance and exit points of the Cherenkov detector was controlled by two WIKA sensors. Another two WIKA sensors were used to monitor the pressure of the membran pump and inside the fridge.

The differential pressure between the inside and the outside of the detector was measured with a Halstrup differential pressure sensor located about 10 cm above the bottom of the detector.

The consumption of too large amounts of radiator gas could point to a leak in the detector volume. Thus, the weight of the gas bottle was measured using a scale with a digital readout. Besides this, during the first stage of filling the detector this was the easiest way to control the amount of gas that was transferred to the detector. Also the weight of the fridge was monitored using a scale with digital readout in order to control the liquifying process.

The flow rate of the gas inside the recycling gas system was controlled with two flow meters located after the silica gel filter and the other one before entering the Cherenkov detector. A needle valve in the inlet on top of the detector was used to adjust the gas flow to reach the required flow rate. The flow rate of the gas inside the detector was determined using another flow meter from Honeywell installed at the exit of the detector.

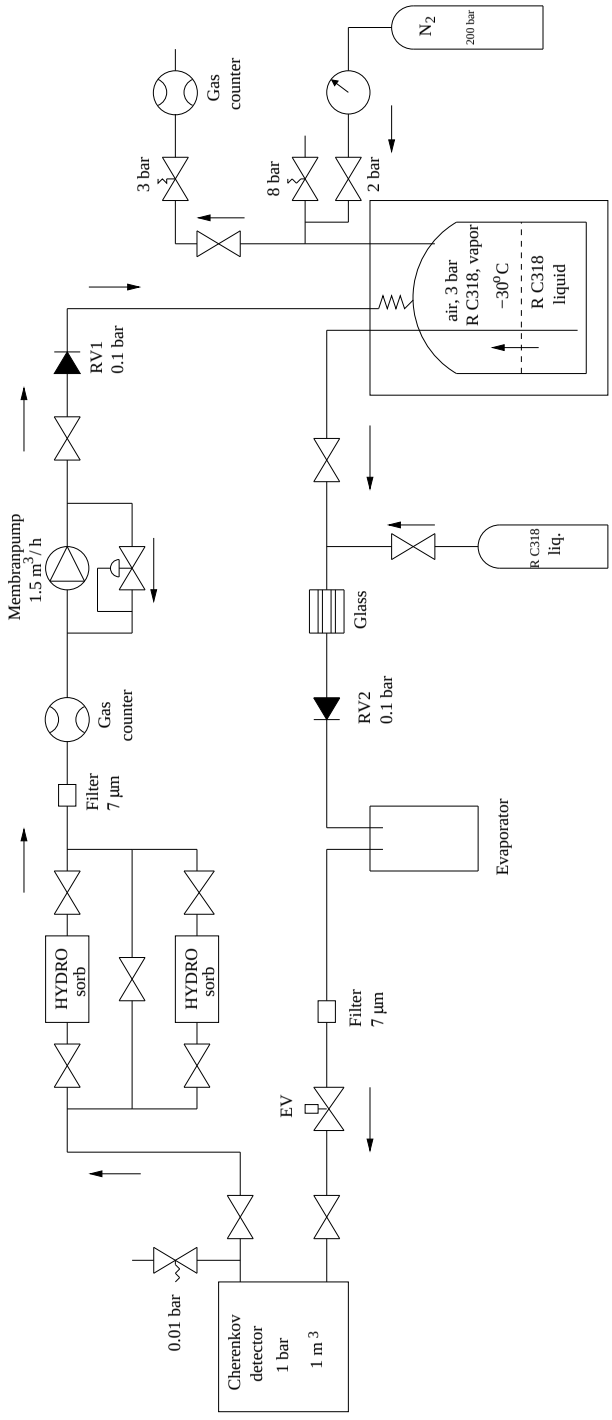

Figure 3.15: Schematic view of the C_4F_8 recycling gas system.

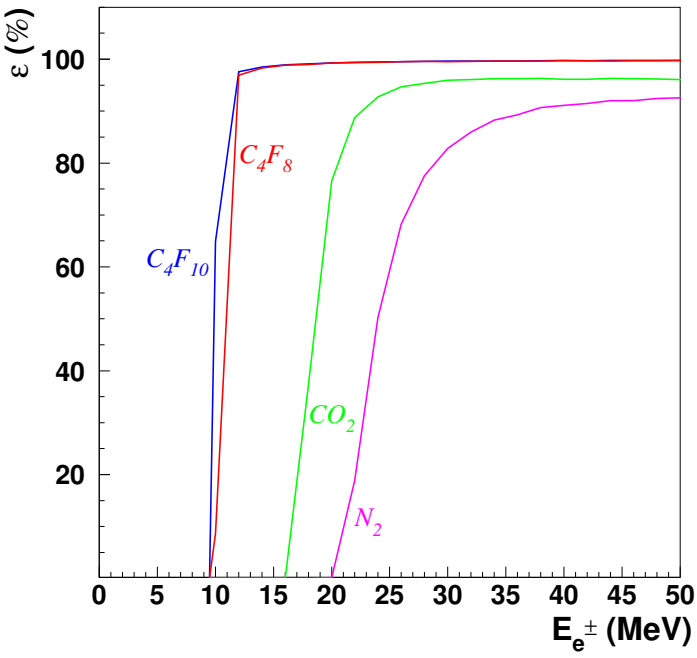

Figure 3.16: Simulated efficiency for different radiator gases.

3.6.4 Efficiency test

A computer simulation was used to evaluate the detector efficiency for different radiator gases. This simulation takes into account light propagation, reflection and the photocathode conversion probability and predicts an efficiency of 100% for C_4F_8 (see Fig. 3.16). In September 2007 a dedicated efficiency test measurement was performed on the A2 beamline. A setup as shown in Fig. 3.17 was used in this measurement. In this figure P1, P2 and P3 are scintillators.
Since the photon beam originates from the bremsstrahlung process in the tagger radiator, the energy distribution exhibitis a bremsstrahlung shape. The energy distribution of the electrons produced by e^+e^- pair production and Compton scattering has a similar shape as the photon energy spectrum. Thus, the efficiency measured in this way is an integrated efficiency over energy and not an efficiency as a function of the electron energy. Due to the approximate 1/E behaviour of the electron energy distribution, low energetic electrons will represent the largest part. The inclusion of the P1 scintillator was intended to cut away these low energy electrons. P1 was placed at large distance from the Cherenkov detector because the electrons at low energies have a larger mean scattering angle than high energetic electrons.

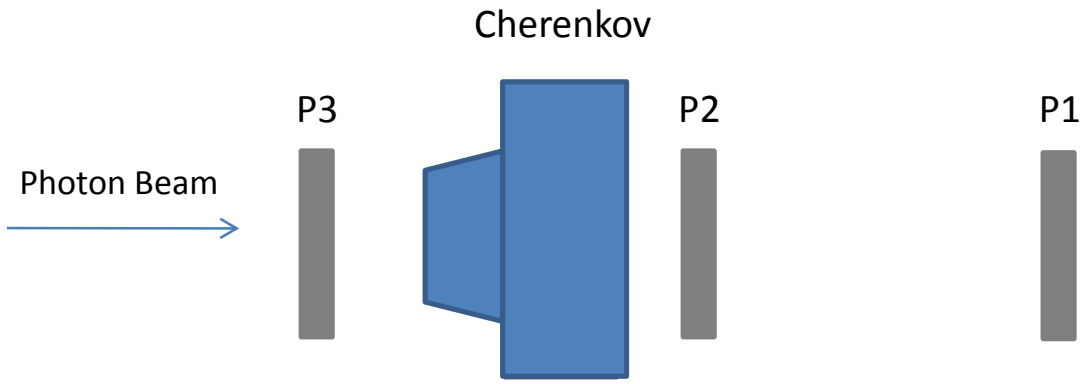

Figure 3.17: Schematic view of the experimental setup used in the Cherenkov efficiency measurement. P1, P2 and P3 are scintillation counters.

During the beamtime, P2 and P3 were in coincidence with the tagger and only triple coincidences (P1-P2-P3) were used to determine the efficiency. Hence, a "good" electron was defined as a particle hitting all three scintillators.
The efficiency at a certain photon energy can be calculated using different TDC spectra of the scintillators. A TDC module (Time to Digital Convertor) receives a start and a stop signal and converts the time difference between these two signals into a channel number. Due to the time difference between the generated start and stop signal a peak will be visible at a certain channel in the TDC spectrum, this is the so called coincidence peak. In the offline analysis it was required that all the scintillators have the same TDC time window and some cuts were applied to reject the random-events and select only events that lie inside the coincidence peak. The efficiency was determined by taking the ratio of the number of good electrons for which the Cherenkov generated a signal and the total number of good electrons.

$$\epsilon = \frac{N_{Good\ \&\ Ch}}{N_{Good}} \tag{3.11}$$

The measured efficiency obtained in this test is shown in Fig. 3.18. The efficiency rises to about 99.95 $\pm$ 0.01 % with a detector that was partially (80 %) filled with C_4F_8 which is in good agreement with the expectations obtained in the efficiency simulation.

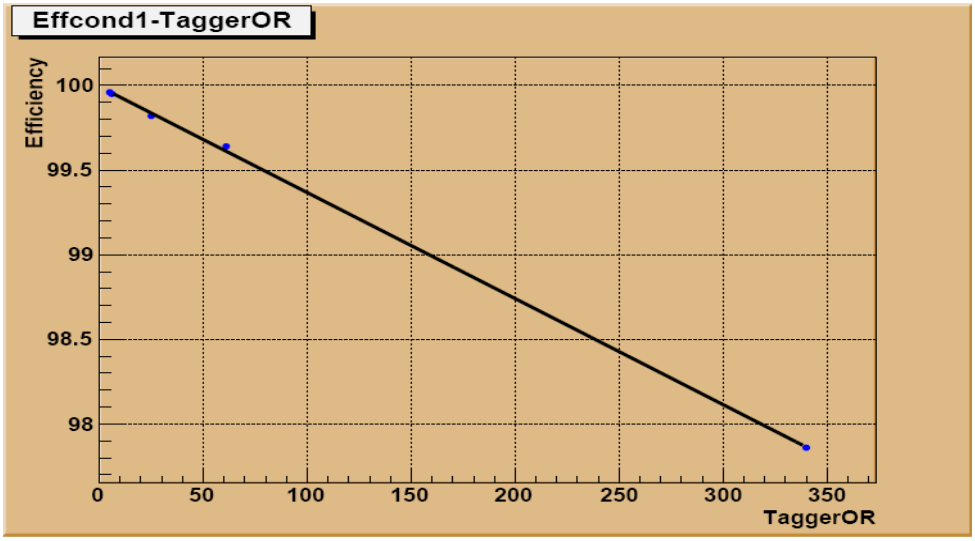

Figure 3.18: Efficiency of the Cherenkov detector partially (80%) filled with C_4F_8 radiator gas as a function of the tagger rate (kHz units).

3.7 TAPS Forward Wall

TAPS [69] is a highly segmented photon spectrometer composed of 384 Barium Fluoride (BaF_2) elements. The acronym TAPS was originally assigned for "Two/Three Arm Photon Spectrometer" reflecting the geometrical setup used in its first experimental run in 1990. TAPS was set up as a forward wall detector to improve the detection efficiencies at forward angles and compensate for the forward coverage gap in the beam exit tunnel of the Crystal Ball. TAPS provides tracking, calorimetry, and identification of particles in this region.

Each of the BaF_2 detector elements is 250 mm long (12 radiation lengths) and has a hexagonal cross section with a 59 mm diameter cylindrical end part (see Fig. 3.19). They are individually wrapped in 8 layers of 38 μm thick PTFE and one layer of 15 μm thick aluminium foil used as a UV-reflector. The crystals are optically coupled to the quartz window of a Hamamatsu R2059-01 photomultiplier tube. To protect the tubes from stray electromagnetic fields in the closed packed detector, the phototubes and the cylindrical part of the crystals were surrounded by a magnetic shield. The length of each crystal corresponds to a stopping range of 180 MeV for $\pi^{\pm}$, 280 MeV for $K^{\pm}$ and 360 MeV for protons.

The scintillation light output of BaF_2 is about 29% lower than that produced by NaI (Tl) [69], however, its high atomic number (^{56}Ba) and density (4.89 g/cm^3) ensure that it maintains a high detection efficiency. The relative intensity of the components of its

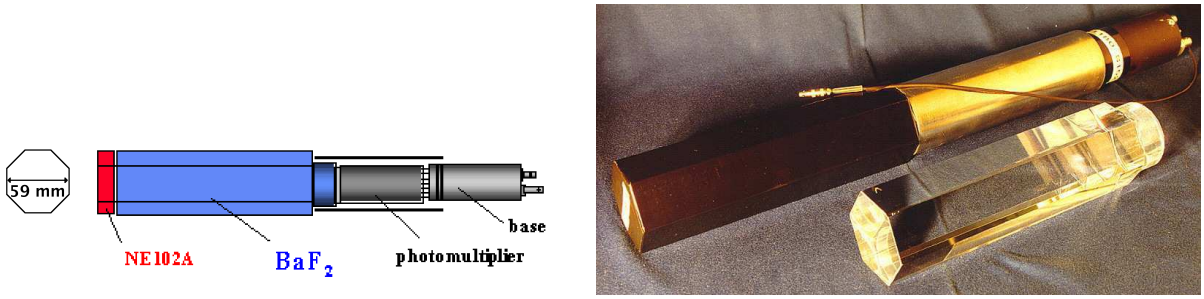

Figure 3.19: Left: Schematic drawing of one BaF_2 element. Right: A Barium Fluoride crystal and assembled detector element.

scintillation emission, one with a very short decay time ($\sim$ 0.6 ns) and another slower one ($\sim$ 620 ns) both in the UV range (220 nm and 310 nm respectively) [70], is strongly dependent on the velocity of the incident particle. The ratio of fast light output to total light output decreases with increasing ionization density (decreasing velocity) of the incoming particle [71]. The fast component provides very accurate timing information on detected signals.

In front of each TAPS counter were mounted an equal number of 5 mm thick plastic veto scintillators (NE102A) of the exact same granularity and hexagonally shaped to match each TAPS counter. Their scintillator light is read out in Valvo XP2972 phototubes via an optical fiber (see Fig. 3.20).

The single counter time resolution is $\sim$ 0.2 ns except at very low photon energies (around 10 MeV). The energy resolution can be described by ΔE/E = 0.018 + 0.008/E$[GeV]^{0.5}$ [69], [72]. The polar angular resolution is better than 1°, and in the azimuthal angle it improves with increasing θ, being better than 1/R radians, where R is the distance in centimeters from the central point of the TAPS wall surface to the point on the surface where the particle trajectory meets the detector. A position resolution of $\sim$ 3 cm can be obtained by taking the "center of gravity" of the signal amplitudes of the electromagnetic shower induced by an incident photon that fires several adjacent crystals.

Several methods can be used for the particle identification in TAPS. The plastic scintillators are used as veto detectors separating charged and uncharged particles. Also due to the excellent timing resolution provided by the fast decay component of the BaF_2, Time Of Flight (TOF) particle identification methods can be used to separate the slower protons and neutrons from the relativistic photons, electrons and pions. Finally, the fraction of light deposited in the slow component of the BaF_2 light output is mainly dependent on the energy loss of the detected particle. It is possible to separate particles via an analysis of the ratio of energy deposited in the fast and the slow components, i.e., a pulse shape analysis (PSA) by placing both a short and a long gate on the QDC of the BaF_2.

TAPS can also contribute to the CB multiplicity trigger and is currently divided in six

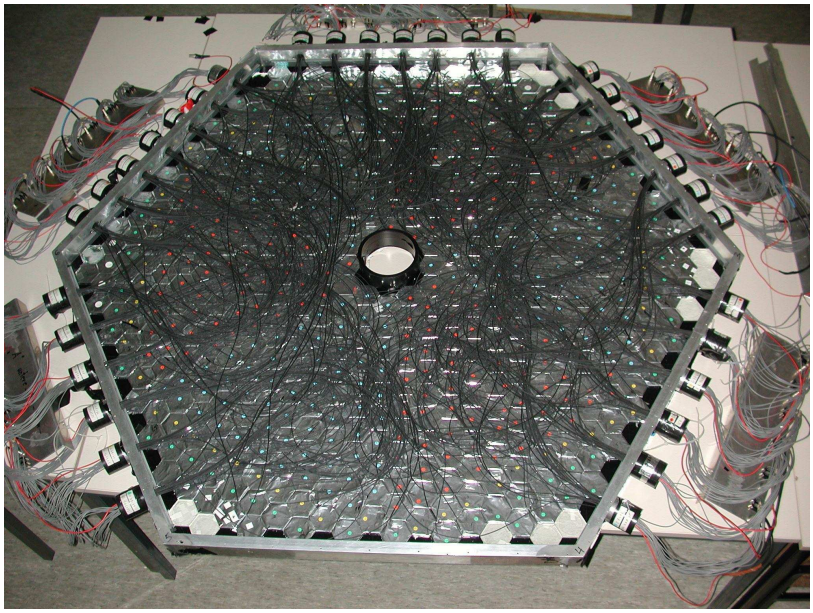

Figure 3.20: TAPS veto wall with the veto detectors and the light guide fibres.

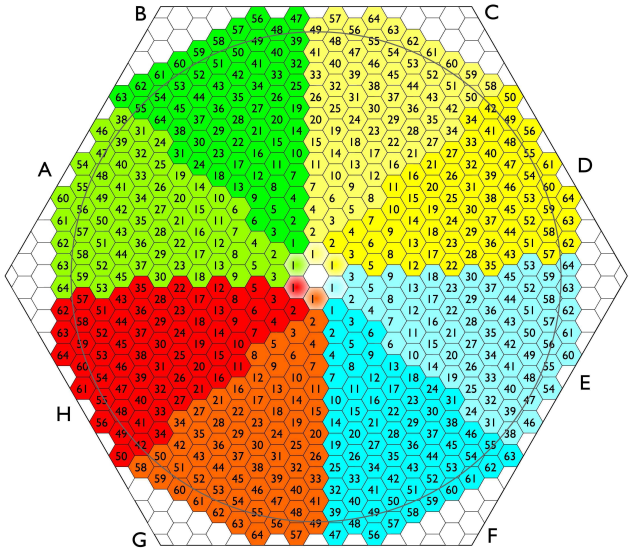

Figure 3.21: Diagram of TAPS forward wall. The numbers in the figure are the labels given to each crystal.

sectors for this purpose (see Fig.3.21). Recently, the two inner rings of 18 BaF_2 elements have been replaced by 72 $PbWO_4$ crystals. Each crystal has 200 mm length (22 radiation lengths) and the higher granularity improves the rate capability as well as the angular resolution. The crystals are operated at room temperature. The energy resolution for photons is similar to BaF_2 under these conditions [50].
TAPS covers an angular range of $0° < \theta < 20°$ and the combined setup of Crystal Ball and TAPS cover 97% of the 4π sr of solid angle.

3.8 Data Acquisition

One of the main factors to be considered in the experiment is the treatment and processing of the data. For this, it is necessary to have a fast acquisition system and an efficient trigger selection. This could be reached with an appropriate electronic setup and read out system.
The goal of the electronic system is to collect the information obtained from the detectors and to provide a digitalization of the time and amplitude of the output signal. The analogue signals are fed to a charge to digital converter (QDC) and, via a discriminator, to a time to digital converter (TDC). The QDC returns a value which is proportional to the amount of energy deposited in the detector by integrating over a sample of the pulse. The TDCs require a start signal which is provided by the experimental trigger and a stop signal which comes from the relevant detector signal above the discriminator threshold. Thus, the timing of a signal in a particular detector is relative to the other detectors.
In this section only a general overview of the electronic system will be presented. For more detailed information see [73].

Crystal Ball Electronics

A simple schematic view of the Crystal Ball electronics is shown in Fig. 3.22. The analogue output signals from the NaI crystal photomultipliers are transmitted to an active splitter where they are divided in groups of 16 crystals. The amplitude signal is delayed by 300 ns and fed to the ADCs and the amplitude of all the 672 crystals is summed and sent to the energy sum trigger. The summed amplitude of the 16 crystal groups is also calculated and sent to the discriminator which provides a high threshold of ≈10 MeV and a low threshold of ≈1 MeV. Then, the number of 16 crystal groups whose energy is above the high threshold is sent to the cluster multiplicity trigger while the signals above the low threshold are used to start the TDCs and the scalers. The trigger signal is sent to the ADC, TDCs and scalers via the trigger control system. Finally, the information is digitalized in the ADCs and TDCs and sent to the storage computer.

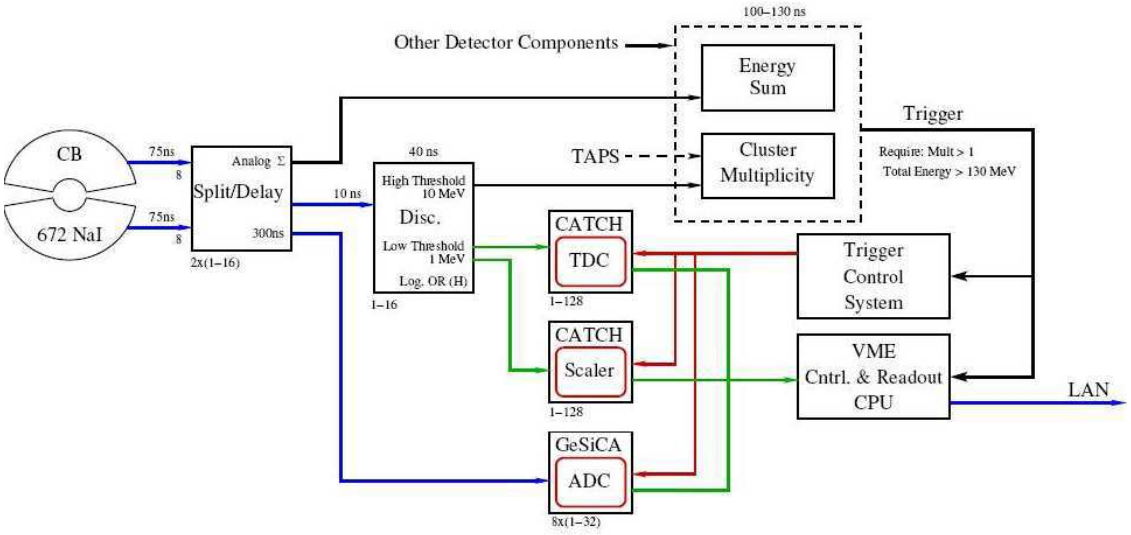

Figure 3.22: Schematic view of the CB electronics.

TAPS Electronics

In this section a schematic overview of the TAPS electronics (see Fig. 3.23) will be given. More detailed information can be found in [74].
The analogue output signal from the BaF_2 crystal photomultiplier is transmitted to a CFD (Constant Fraction Discriminator) with a 30 MeV threshold. A signal higher than the CFD threshold is the signature of a hit in the crystal. It gives the start signal for energy integration in both long and short gate QDCs and for the time measurements in the TDC. The constant fraction technique with minimum walk determines the start signal very precisely and thus to perform time of flight and pulse shape analysis with a high resolution. Then, if the signal is higher than the LED (Leading Edge Discriminator) threshold, it will be part of the trigger. The trigger signal is sent to the QDCs and TDC and it stops the time measurement in the TDC. Finally, the digitalized QDCs and TDCs information is sent to the storage computer.

Triggering Electronics

The experimental setup used in the ^{3}He beamtime used event triggering from CB and TAPS. The trigger is based on the energy sum of the Crystal Ball and the cluster multiplicity. The CB energy sum is carried out by summing the analog energies of all 672 NaI crystals. If the total energy deposition is below a definite threshold (20 MeV in our

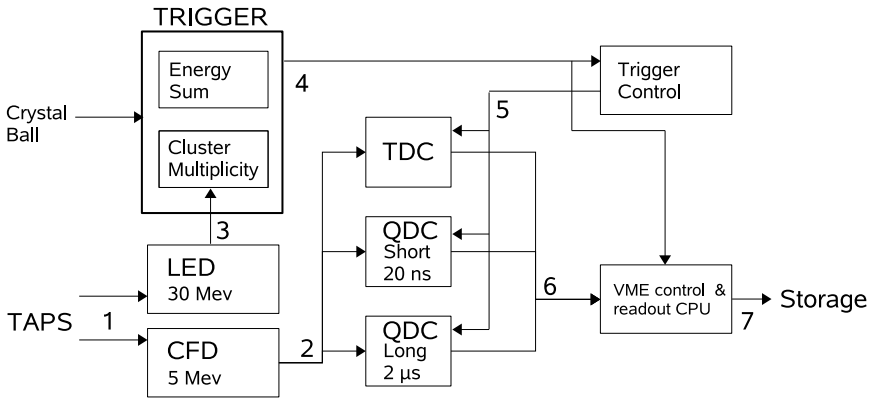

Figure 3.23: Schematic view of the TAPS electronics.

experiment) the event will be rejected. The cluster multiplicity is used to reject or keep events according to the number of final state particles. For this purpose, the active splitter in the CB electronics divides the 672 NaI crystals readout in 45 logical segments made of 16 contiguous crystals and calculates the analog energy sum of each individual segment (for more information see section 6.4).
TAPS takes part in this trigger in a similar way. It has been split in 4 logical segments made of 128 BaF_2 crystals. If any crystal in a segment has an energy deposition above 40 MeV LED threshold, a multiplicity hit will be recorded.
Fig. 3.24. shows a technical scheme of the trigger implementation in the electronics. More detailed information about the trigger electronics can be found in [73]

Analysis Software

The electronic setup is controlled by a VMEbus single-board computer running the LynxOS operating system and the ACQU data acquisition program. The data acquisition program, called AcquRoot, is written in C++ and is based on the ROOT analysis package from CERN [75].
The CB and TAPS data acquisition run at the same time and AcquRoot, which recognises both data formats, allows to simultaneously perform basic online analysis of the data. Thus, it provides the detectors basic energy, time and scaler histograms. This gives a continuous information of the data quality and check that the synchronisation between the CB and TAPS DAQ systems is maintained.

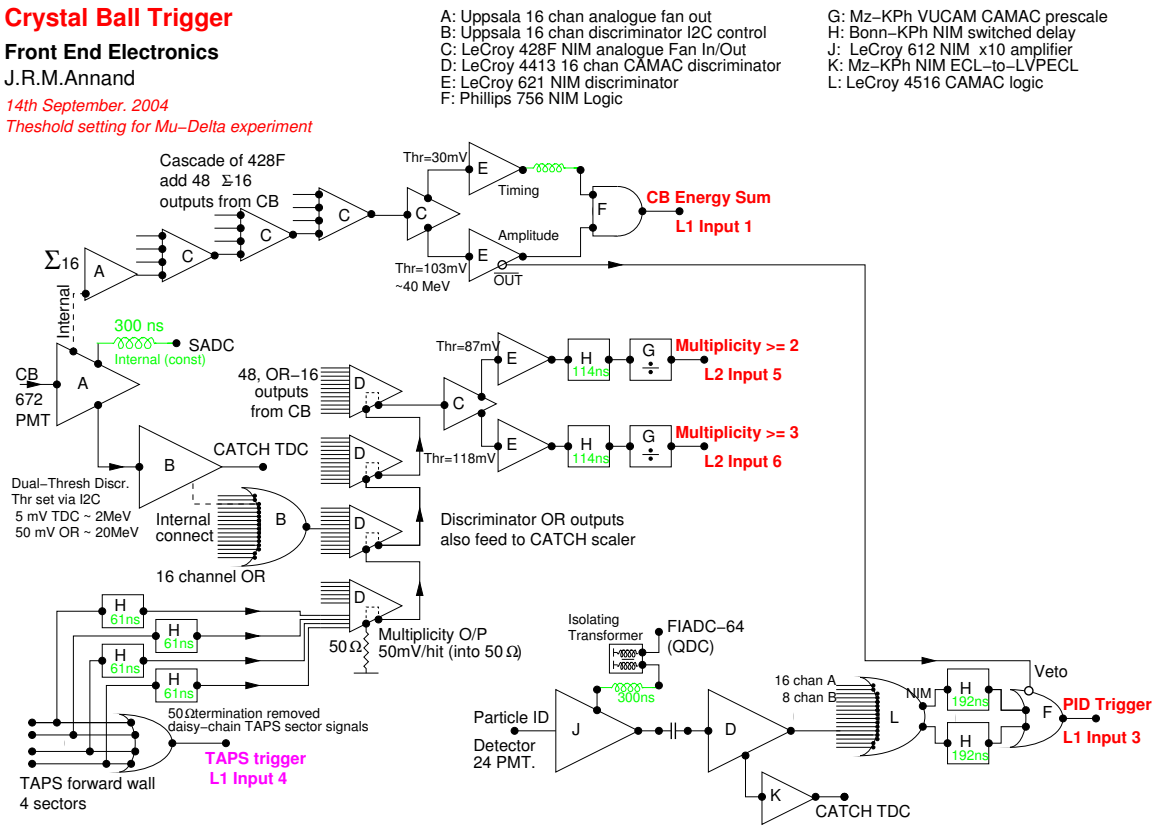

Figure 3.24: Schematic view of the CB trigger electronics.

Chapter 4
The Polarized ^{3}He Gas Target

4.1 Introduction

Polarised ^{3}He has applications in different fields of physics ranging from quantum phenomena in the gaseous and fluid phases at low temperature [76], spin filters for cold neutrons [77], [78], [79] to medical diagnostics (^{3}He MR-tomography of the human lung) [80-83] and as a polarised target for nuclear physics experiments [84], [85].
Neutron targets would be useful in scattering experiments, but a free neutron has a half-life of about 15 minutes [86]. Instead of a free neutron, a ^{3}He nucleus is a stable alternative. The ^{3}He nucleus is composed by two protons and a neutron. The dominant component of the ground state wave function is the spatially symmetric S-state [87], [88] with small admixtures of D-state and S'-state (see Fig. 4.1). In the S-state, because of the Pauli principle, the spins of the two protons are coupled to spin = 0 and the neutron carries the ^{3}He nuclear spin. The D-state is due to the presence of the tensor force and is a L = 2 state in which the three nucleon spins are oriented antiparallel to the orbital angular momentum. The S'-state is a L = 0 state that is not symmetric in the position coordinates of all three nucleons and arises because of the spin dependence of the nucleon-nucleon interaction.
Non-relativistic Fadeev calculations [87-89] of the three body bound state predict contributions to the ground state from $\sim$ 90% of S-state, 8.5% of D-state and $\sim$ 1.5% of S'-state. This picture is supported by the similarity between neutron and ^{3}He magnetic moments ($\mu_n = -1.91\mu_N$ and $\mu_{^3\mathrm{He}} = -2.12\mu_N$).
Hence, at first order, ^{3}He polarised targets can be used as effective polarised neutron targets, apart from some dilution coming from the protons and this was the reason to choose polarised ^{3}He to check the GDH integral on the neutron.
In this chapter is given a detailed description of the principle and performance of the polarised ^{3}He target used in the beamtime of July 2009. In section 4.2 the method used to polarise the ^{3}He gas is described. In section 4.3 the different depolarisation mechanisms and their effects in the ^{3}He samples are discussed. The preparation of the different com-

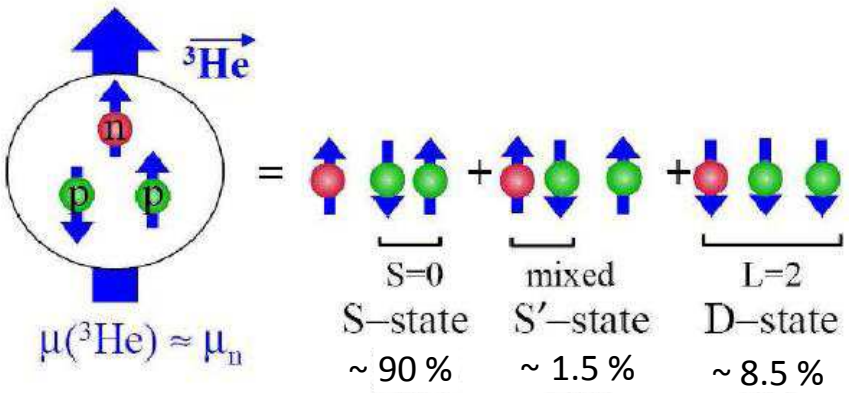

Figure 4.1: Components of the ground state ^{3}He wave function.

ponents of the target setup is described in section 4.4. In this section are also presented the preparation of the target cells and the design and the results obtained from some tests of the magnetic field and gradients of a solenoid and a pair of Helmholtz coils. Both components were used to provide a magnetic holding field over the target cell volume inside and outside the Crystal Ball detector, respectively. Finally, in section 4.5 the basics of the NMR technique and the setup used to measure the polarisation of the ^{3}He gas during the beamtime are presented.

4.2 Polarisation of ^{3}He

The ^{3}He gas used in this work was polarised by means of the Metastability Exchange Optical Pumping (MEOP) method. The MEOP process takes place in a homogeneous guiding magnetic field with the field direction defining the spin quantization axis. The polarisation process starts with a weak RF electric discharge that is maintained in a low pressure ^{3}He gas sample. In this way, a small fraction of the atoms ($\simeq 10^{-6}$) will be in the $2\,^3S_1$ metastable state. Then, circularly polarized resonant light at the wavelength of 1083 nm, incident upon the sample, excites the transition of the $2\,^3S_1$ state to the $2\,^3P_0$ states (see Fig. 4.2).
The $2\,^3S_1$ and $2\,^3P_0$ states are split by the fine and hyperfine interactions, yielding a total of 9 different allowed transitions [90], [91], labelled C_1 to C_9 [92]. The ^{3}He transitions C_8 and C_9 produce the largest ^{3}He polarizations. The components of the hyperfine structure

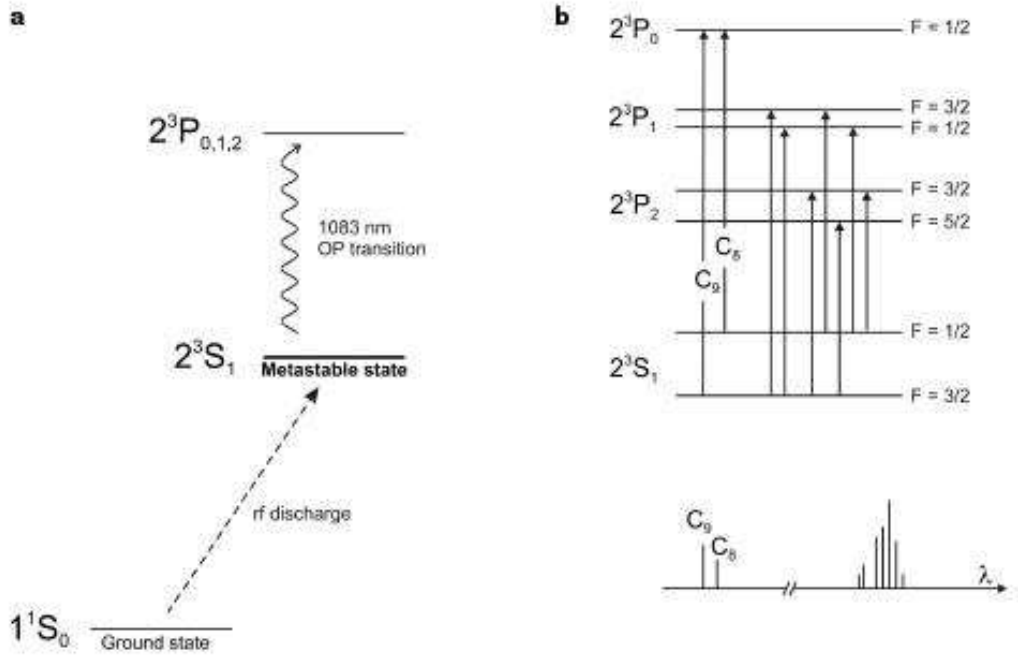

Figure 4.2: a) Low-lying ^{3}He energy levels. b) Optical transitions between the $2\,^3S_1$ and the $2\,^3P_0$ states of the ^{3}He .

of this line are depicted in Fig. 4.2.

Since the ^{3}He nuclei have spin I = 1/2, the atomic states have hyperfine structure with sublevels characterised by the magnetic quantum numbers m_F. The absorption of right-handed circularly polarised (σ^+) laser light causes transitions from the $2\,^3S_1$ ($m_F = -1/2$) to the $2\,^3P_0$ ($m_F = +1/2$) state (see Fig. 4.3). Then, after excitation, a spontaneous reemission to both sublevels of $2\,^3S_1$ state occurs. However, the continuous depopulation of the $m_F = -1/2$ sublevel results in a higher population of the $m_F = +1/2$ state.

Thus, the angular momentum of light is transferred to the metastable atoms which become polarized. Transfer of nuclear polarization to the ground-state atoms is achieved through metastability exchange collisions. During that process a polarised metastable atom and a non-polarised ground state atom exchange the excitation of their atomic electrons without altering the nuclear spins of the atoms involved. The collision process can be written as:

$$^3\vec{H}e(2\,^3S_1) + {}^3He(1\,^1S_0) \rightarrow {}^3\vec{H}e(1\,^1S_0) + {}^3He(2\,^3S_1)$$

As a result one obtains a ground state with the polarised nucleus, and a new metastable atom can be further optically pumped by the laser.

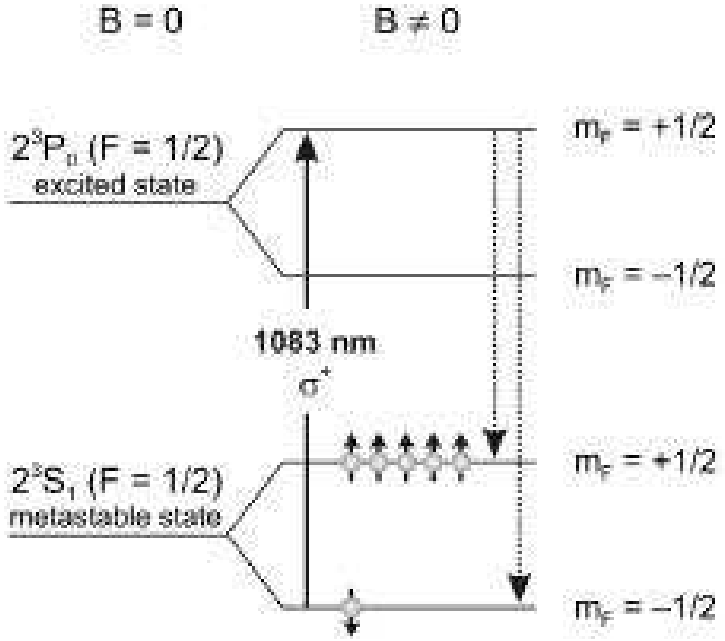

Figure 4.3: Schematic diagram of the optical pumping using the C_8 component of the ^{3}He transition. Right-handed circularly polarised light (σ^+) can only excite the transition with angular momentum selection rules $\Delta m_F = +1$. As a result the $m_F = -1/2$ state is depopulated and all population is transferred to the $m_F = +1/2$ state.

The metastable exchange optical pumping is a very fast and efficient process, in which it is possible to achieve very high polarization values (up to about 80%) in low pressure samples of ^{3}He of about 1 mbar [93], in only a few seconds.

4.2.1 ^{3}He Polarising System

The ^{3}He is spin-polarised with the polariser device of the Institut of Physics in Mainz from where it is transported to the A2 experimental area at MAMI.
A schematic sketch of the gas production system is presented in Fig. 4.4. The whole apparatus is located in a homogeneous magnetic field of 10 Gauss generated by a set of six coaxial coils and with relative field gradients $(dB_r/dr)/B_0$ in the order of $10^{-4}cm^{-1}$. This magnetic holding field provides a quantisation axis for the polarised ^{3}He nuclei.
The polarising system is composed mainly by three different parts. In the upper part of Fig. 4.4 one can see the ^{3}He reservoir and the titanium getters used for purification. In the middle part of this figure the optical pumping volume that has typical pressure values of

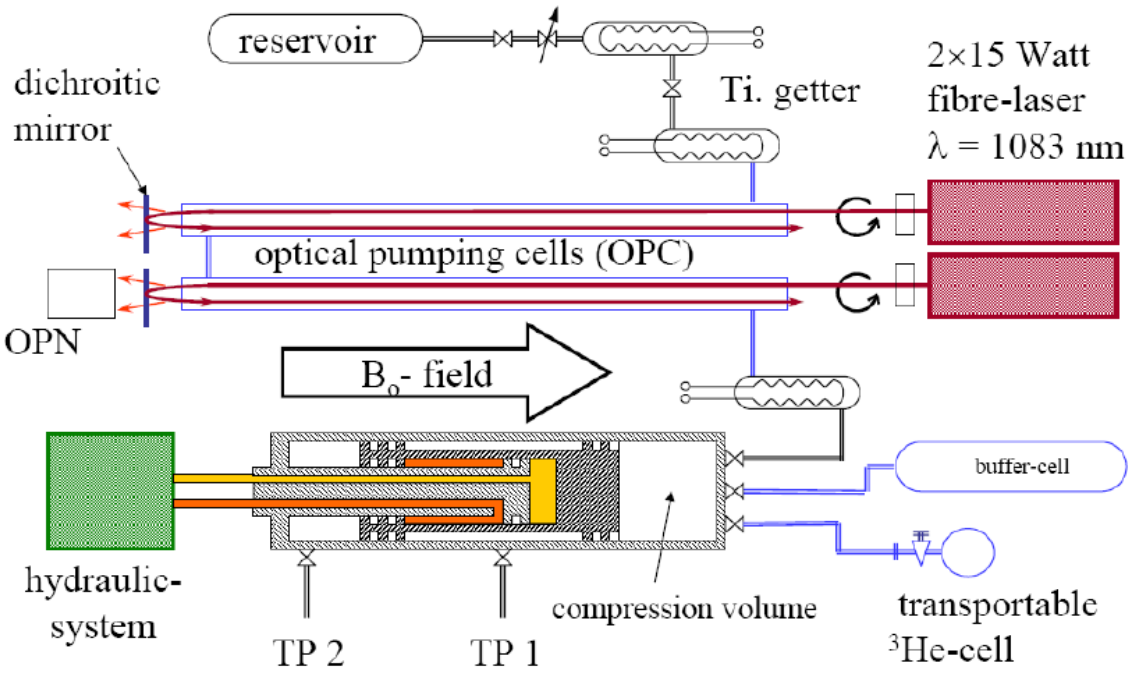

Figure 4.4: Schematic diagram of the Mainz ^{3}He Polarizer and Compressor system.

about 1 mbar is depicted. Two commercial 15 W fibre lasers (IPG Photonics Corporation, Model: YLD-15-1083) at 1083 nm are used for the optical pumping. This laser light passes through a polarizer cube and a lambda quarter plate and is circularly polarized. Then, this light is absorbed by the metastable atoms and in this process the angular momentum of the photon is transferred to the electron shell of the atom. Finally, after reemission and hyperfine coupling (in the $2\,^3S_1$ state), the resulting nuclear polarisation is transferred to the ground state by metastability exchange collisions.

In order to have the maximum light absorption, the five OP-cells have a length of 2.40 m. The laser beam passes through each OP-cell once and is then reflected back by dichroic mirrors, passing through each OP-cell for a second time to increase the efficiency of the optical pumping process. The nuclear polarization of the ^{3}He gas inside the OP cells is measured by an optical polarimeter. The optical method used to determine the nuclear polarization is based on the analysis of the degree of circular polarization of the red (668 nm) light emitted by the discharge in the cell [94].

After the optical pumping in the OP cells has been completed, in the last part of the process the polarised ^{3}He gas is compressed up to pressures of 5-6 bar using a mechanical non-magnetic polarization-conserving Titanium compressor driven by hydraulics that can

be seen in the lower part of Fig. 4.4. In a first step, the polarised gas is compressed into a buffer cell of V = 4 L. After having polarised the desired amount of gas, the polarised ^{3}He from the buffer cell is then compressed in a second step into a detachable storage cell. The loss of polarisation in the compressor is less than 2% [95] and 2 bar $\cdot$ l of ^{3}He can be polarised per hour to values $\geq$ 70% [96], [97].

4.3 ^{3}He Polarisation Relaxation

One of the most important considerations in the design of a polarised ^{3}He gas target is the minimisation of depolarising effects. The polarisation decays exponentially and can be written as:

$$P(t) = P_0 \; e^{-\frac{t}{T_1^{total}}}$$

where P_0 is the initial polarisation and T_1^{total} is the depolarisation time constant. There are three main factors that contribute to the total relaxation time T_1^{total} :

1. ^{3}He collisions with the cell wall (T_1^{wall}).
2. Magnetic dipole-dipole interactions between ^{3}He nuclei (T_1^{dipole}).
3. Magnetic field gradients (T_1^{grad}).

The total ^{3}He polarisation relaxation rate, T_1^{total}, is a sum of these individual effects:

$$\frac{1}{T_1^{total}} = \frac{1}{T_1^{wall}} + \frac{1}{T_1^{dipole}} + \frac{1}{T_1^{grad}}$$

Dipole relaxation results from ^{3}He -^{3}He atomic collisions, where the magnetic dipole interaction couples the nuclear spins resulting in a loss of nuclear polarisation to the relative orbital angular momentum of the colliding atoms [98]. The dipole relaxation is dependent on the ^{3}He density which is fixed by the constraints of the experiment and varies slightly with the temperature. Dipole induced relaxation has been calculated to be

$$T_1^{dipole} = \frac{807 \; h \cdot bar}{p \; [bar]}$$

where p is the measured pressure in bar at 300 K.
Another dominant relaxation source usually results from the collisions of the ^{3}He atoms with the walls of the target container. Wall relaxation rates can vary depending on the glass material used to build the cells. Different materials like pyrex, quartz, and aluminosilicate glasses (Corning 1720 and 1723; Schott 8290; GE180) have been tested as cell materials. In addition, various metallic surfaces have been examined by introducing metallic samples into the cell [98]. In conclusion, metals are found to give poorer results than

aluminosilicate glasses. There are two mechanisms, permission and absorption, which keep the gas nuclei in the vicinity of the glass surface, and those are the two dominant sources of wall relaxation. Relaxation occurs when the glass contains paramagnetic centers which can interact with the noble gas, causing the nuclear spin to relax.
The relaxation of a ^{3}He atom which has been absorbed into the glass may in general be a result of three mechanisms: precession of the ^{3}He moment about the net local field, magnetic field gradients caused by the magnetic dipoles in the glass, or dipolar coupling between a ^{3}He nucleus and a flipping magnetic dipole in the gas. The effect of these mechanisms is to reorient the nuclear spin of the ^{3}He atom away from its original direction. Wall relaxation of ^{3}He was investigated [99] by measuring relaxation times for ^{3}He in cells made from Pyrex and the aluminosilicate glass Supremax, that were internally coated with various metals. The results obtained reported that cesium, bismuth, and lead showed significantly increased relaxation times compared to uncoated Supremax cells, while magnesium, antimony and zinc did not show improvement. Pyrex cells coated with cesium, bismuth and rubidium also showed a large increase in relaxation time. Therefore, the wall relaxation rates are reduced using a cell wall coating [100].
In addition to T_1^{wall} and T_1^{dipole}, inhomogeneous magnetic fields can cause a significant destruction of the nuclear polarization. As polarized ^{3}He diffuses in magnetic field gradients, in its rest frame it may "see" time-dependent magnetic fields with a frequency near its Larmor frequency, resulting in a spin flip. The relaxation related to magnetic field inhomogeneities has been calculated [99], [101] and is given by:

$$T_1^{grad} = \alpha(B_0/(dB/dr))^2 \cdot p$$

where α is the diffusion constant of the ^{3}He in the target ($\alpha = 1.8 \times 10^3\,\mathrm{cm^2\,bar\,}h^{-1}$), $\mathrm{d}\vec{B}/\mathrm{d}r$ represents the transverse field gradient averaged over the cell volume, B_0 is the magnetic holding field, assumed to be along the *z-axis*, and p is the pressure.
Therefore, to guarantee that the field gradients are not relevant for the total lifetime, the relative field gradients are required to be less than about $10^{-4}\,\mathrm{cm^{-1}}$ for typical operating conditions with a holding field of $B_0 = 7$ Gauss.
This contribution to the ^{3}He relaxation rate can be made negligibly small by controlling the field gradients through a proper magnetic design of a solenoid, by magnetic shielding (important in the experiments where spectrometer magnets are close to the target) and by increasing the static field.

4.4 ^{3}He Target Setup

4.4.1 Overview

The main components of the polarised ^{3}He target setup are shown in a schematic view in Fig. 4.5. The target setup included, in addition to the target cell, a solenoid, a mechanical

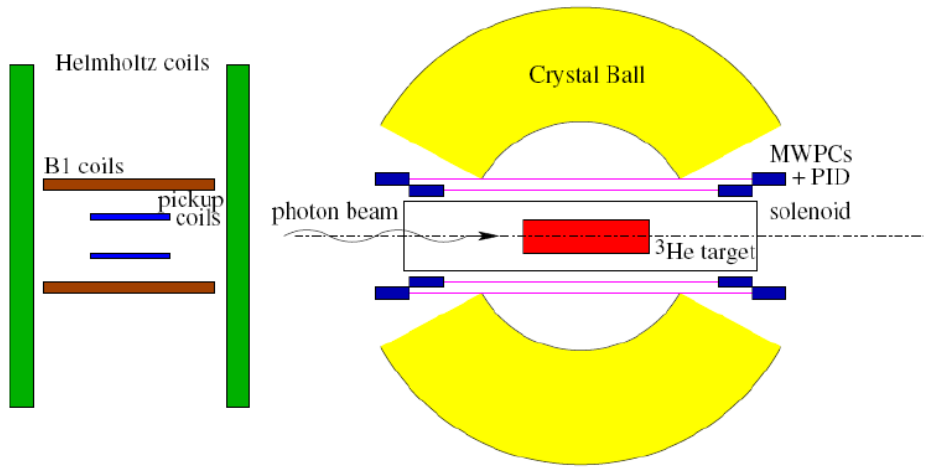

Figure 4.5: Sectional view of the ^{3}He experimental setup.

transport system and a pair of Helmholtz coils that comprises the vacuum chamber and the additional coils necessary for the polarimetry measurement. During the experiment, the ^{3}He target cell was located in the middle of a solenoid inside the Crystal Ball detector. This solenoid was used to provide the target spins with a magnetic holding field of a few Gauss, as well as to define the orientation of the polarisation parallel to the direction of the beam.

The pair of Helmholtz coils were placed outside of the Crystal Ball, in the upstream side, and was used to provide also a magnetic holding field to the gas target during the polarimetry measurement that will be described in more detail in section 4.5. A vacuum chamber, enclosing the RF and pick-up coils used in this polarisation measurement, was located in the middle of the two Helmholtz coils.

During this measurement, the ^{3}He cell was mounted within the vacuum chamber using a three-point adjustable aluminium support system which allowed for precise positioning of the target cell with respect to the chamber and the photon beam. The target cell edge was rigidly clamped to this aluminium holder by a brass screw. The aluminium holder was mounted in a non-magnetic mechanical rail system (igus DryLin-ZLW-1040 Toothed belt axis). This transport system is composed by a 2 m lubricant-free linear guide moved by a neoprene toothed belt with fiber-glass reinforcement. During the beamtime, this belt was driven up and down of the beam path by a stepping motor, transfering the target cell from the position in the Helmholtz coils during the polarisation measurement and exchange of the target cell and the position inside the solenoid during the normal data-taking.

The transport system had the possibility to transport the cells in manual or remote control

mode, thus it was possible to perform the polarimetry measurement without entering the experimental hall.
The rail system was mounted on a large vacuum flange which was attached to the vacuum chamber. This vacuum chamber was constructed from aluminium and connected from one side to the solenoid and from the other side to the beam pipe, also with aluminium flanges and tubes. Aluminium was chosen for its non-magnetic properties, since the vacuum chamber and the transport system are embedded in the magnetic field of the Helmholtz coils and the presence of magnetic materials could cause the appearance of magnetic field gradients. The whole system was pumped out by a mechanical pump and the vacuum was only broken for the exchange of the target cells.
The production and test of some components of the setup are discussed in further detail in the next sections.

4.4.2 Target Cell

An essential issue to perform the polarised ^{3}He measurement, was to obtain long relaxation times in order to achieve and maintain large nuclear polarisations of the samples. The fabrication of the target cell was very important in the production of these polarised ^{3}He gas samples. The construction of the target cell was constrained by the gas pressure required and by the atomic flux into the target cell. Moreover, another major topic in the performance of the target was to maintain the desired gas density.
As mentioned in section 4.3, the interaction with the inner surface of the cell is one of the most important sources of gas relaxation. Hence, different materials were examined by several groups [102], [103], [104] and it was suggested that glasses with low concentrations of paramagnetic iron atoms will have longer ^{3}He relaxation times than those with higher concentrations [105]. Low permeability of ^{3}He into the glass is also thought to increase the polarization relaxation time.
Therefore, quartz and pyrex glass cells were used in our experiment even with its high ^{3}He permeability due to its low iron content and also in order to minimize contamination of ^{3}He atoms. To reduce the effect of the high ^{3}He permeability in these two materials, the inner walls of the cells were coated with cesium. Cesium was chosen since the attractive potential of the helium atom to the cesium surface is very weak [106]. Due to this capability of repelling the ^{3}He atoms from the surface, there is a significant improvement in the relaxation times obtained from uncoated to cesium coated cells.
Seven different target cells were used during the ^{3}He experiment. The target cells were identical in design and very similar in dimensions (see Fig. 4.6). The Crystall Ball detector puts geometric constraints on the space available for the target. In order to fit inside the inner part of the CB detector and to reach a useful experimental luminosity, the target cells are cylindrical with an outer diameter of 6 cm and a total length of 20 cm. Under these conditions, with a gas pressure of 6 bar, the area density of ^{3}He atoms is

Figure 4.6: Overview of the target cell used in the photon beam.

$N_T \sim 3 \cdot 10^{21}/cm^2$. The total volume of the target cell is about 450 cm^3, with 2 mm thick glass walls. The size of the target cell is a compromise since the length of the cell has to be maximum compatible with the acceptance of the detector.
To minimize glass interactions with the photon beam during the scattering experiment, the cell had beam entrance and exit windows. The selection of the window materials was one of the most important features of the target cells, since there are several requirements that these materials have to fulfill. The material has to provide the necessary gas tightness and also as long as possible relaxation times of the gas polarisation. Besides this, it is essential to minimise the thickness of the window foils in order to have an appropriate gas to window events ratio. Thus, different materials were examined in order to know which one could be used for the target cell windows. Table 4.1 shows the different materials used in the ^{3}He measurement and some of their properties. The first material used for the target windows was aluminised Mylar, although it was rejected after it was seen that the cesium coating was destroyed, since water vapour from surrounding air diffused inside the cell. Afterwards, a target cell with Berilium windows was produced and used in the first days of the ^{3}He beamtime. The thickness of the foils was higher than the thickness of the other materials used in another cells, however the windows could not sustain the high pressure of the gas and the windows broke after few refillings of the cell with the polarised gas. This effect was probably due to the lower tensile strength of beryllium compared to the other materials used for the windows. Another material used was Havar. This is a cobalt based alloy that provides very high strength. The alloy has excellent corrosion resistance and is non-magnetic, but it has very short T_1 times. In parallel to the cells

Material	t [μ m]	$\rho \cdot t$ [g/cm^2]	T_1^{wall} [h]
Mylar (Al)	50	0.007	18
Be	150	0.027	14
Havar	10	0.008	15
Ti	50	0.022	40

Table 4.1: Properties of several materials used in the ^{3}He measurement. t is the thickness of the material, $\rho \cdot t$ is a measure of the expected background and T_1^{wall} is the total wall relaxation time.

with Havar windows a set of cells with titanium windows was produced. Finally, this was the preferred solution, since these cells with titanium windows gave the largest relaxation times providing the most statistically significant data.
The window foils were glued, using Araldite 2011, to aluminium caps (see Fig.4.6), which have a hole of 30 mm in the center to allow the beam to pass through. These aluminium caps provide some mechanical support to hold the high pressure of the gas inside the cell. In Fig. 4.6 one can also see the glass valve (Young POR 3/glass) that allowed the filling and venting of the polarised ^{3}He . This valve was connected to the ^{3}He filling station which provided the compressed polarised ^{3}He gas.

Cell Preparation

To make sure that there were no impurities in the cell before filling with the polarised ^{3}He , the cells were treated and prepared using a multi-step procedure. First, the cells were rinsed with distilled water and Mucasol. Afterwards the cells are pumped out and coated with cesium. The cesium intended for coating of the inner walls was distilled from a side arm into the cell kept at room temperature. Afterwards, once the inner walls were evaporated with the Cesium metal the side arm used in this procedure was sealed off. Finally, after the degaussing of the cells, they were ready for direct optical pumping with polarised ^{3}He gas.
In the preparation of the cell, it has to be taken into account that, as it was already mentioned before, the ferromagnetic contaminants produce a high depolarisation of the ^{3}He gas [107]. Therefore, an appropiate demagnetisation [108] of the cell increases significantly the relaxation times as it can be seen in Fig. 4.7. In this figure the black curve represents the relaxation time of one of the cells used in the ^{3}He beamtime as a function of the pressure before the degaussing procedure, while the red curve represents the relaxation time for the same cell after the demagnetisation. As it can be clearly seen in this plot, at 4 bar (the mean pressure of the ^{3}He gas during the beamtime) the relaxation time increases from 20 h to 35 h for the same cell.

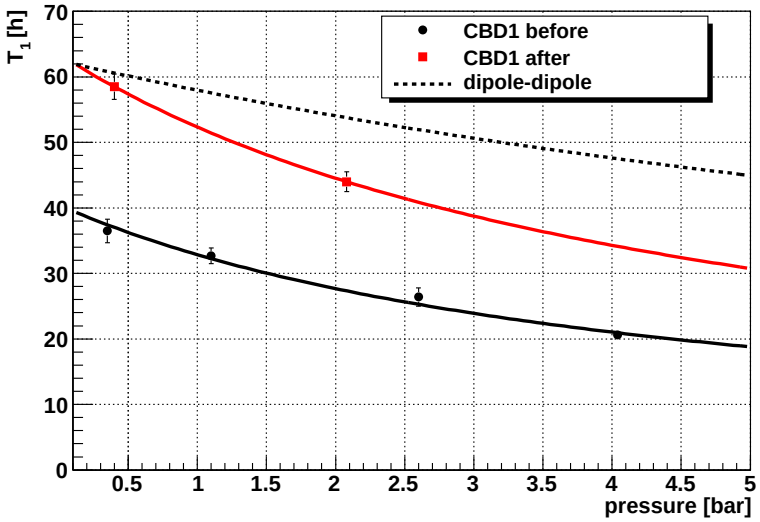

Figure 4.7: Relaxation time as a funtion of the pressure before and after the degaussing procedure.

The demagnetization is accomplished by a rapidly reversing and decreasing of the magnetic field inside which the cell is located. This procedure will cause the impurity dipoles to assume a nearly random orientation throughout the material.

Cell Transport and Installation

When the polarised ^{3}He filling process at the polariser setup in the Institute of Physics in Mainz was finished, the target cell was brought to the A2 experimental area at MAMI. During the transport, the polarized gas needs a magnetic guiding field of a few Gauss which has to be sufficiently homogeneous across the cell volume to prevent the gas depolarisation. For this reason, the cell was transported inside a pair of Helmholtz coils with a movable power supply, as shown in Fig. 4.8.

The installation of the cell was a delicate procedure, since it was essential to avoid the appearance of field gradients that lead to gas depolarisation. First of all, the cell was transferred from the transport Helmholtz coils to the vacuum chamber where it was fixed to the aluminium support attached to the stepping motor, as it can be seen in Fig. 4.9. Then, the chamber was closed and air was pumped out. Afterwards, the first polarisation measurement, which took aproximately 3 minutes, was performed. Once this measurement was finished, the cell was transported by the mechanical rail system to the center of the CB detector for the normal data taking period.

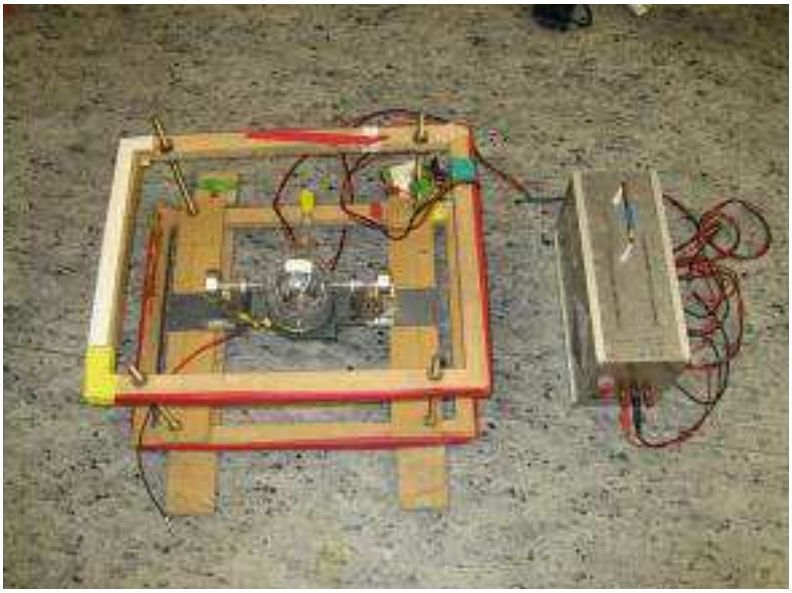

Figure 4.8: Transport Helmholtz coils.

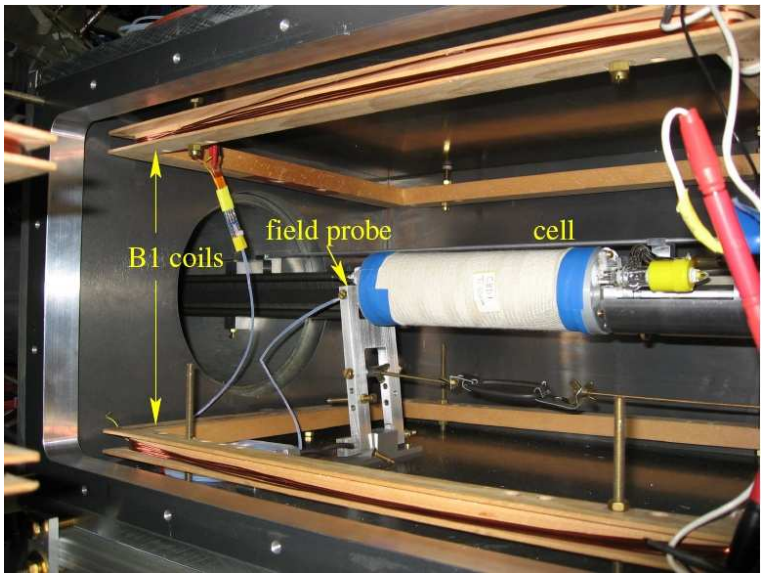

Figure 4.9: Target cell located inside the vacuum chamber.

At the end of the whole transport process, the relative loss of polarisation was $\sim 1\%$. The polarimetry measurement was carried out every 2 hours during the beamtime running period and the target cell was exchanged two times per day.

4.4.3 Magnetic Holding Field

In order to keep the ^{3}He target cell polarised for a sufficiently long time, it has to be kept, during data taking, inside a controlled uniform magnetic field volume. The strength and uniformity of this field play an important role in obtaining long polarization relaxation times. The gradient-to-field ratio should be less than $10^{-4} cm^{-1}$ for a magnetic field of approximately $7\,G$.
Iron-free solenoids are known to produce regions of very uniform fields which are long in the direction of the lines of force. Therefore, a solenoid was used to achieve such conditions. The critical parameters of the solenoid design were dimension, material and electronics to be used.
As the solenoid had to be placed inside the Crystal Ball detector, it had to have an appropriate size to fit inside this detector. Moreover, the target cell dimensions constrained the inner radius of the solenoid. The only free geometrical parameter was the length. Taking the homogeneity constraints into account, it had to be shown that the available space along the z–axis was sufficient to place a solenoid that creates a magnetic field which meets these constraints. Hence, solenoids of various lengths between 600 mm and 1000 mm were studied to find the minimum length necessary.
Since the goal was to mathematically model a solenoid and determine the region of uniform magnetic field within a given tolerance, numerical calculations of the field and gradients were carried out with a finite element code called FEMM (Finite Element Method Magnetics). This program can be used for solving electromagnetic two dimensional problems at low frequency for planar and axisymmetric domains. The program currently deals with linear/nonlinear magnetostatic [109], linear/nonlinear time harmonic magnetic and linear electrostatic problems.
With the data obtained from the FEMM simulation, a 800 mm length solenoid was manufactured [110]. The material used to build the solenoid was copper wire of 0.424 mm diameter. The size of the wire, together with the magnitude of the magnetic field and the current flowing through the wire, determine the number of turns used to produce the solenoid.
The solenoid has an inner diameter of 82 mm and an outer diameter of 82.8 mm. The coil was wound on a CFK–tube with a cross section of $1 \times 82\,\mathrm{mm}^2$ and 1200 mm in length. The solenoid contains one layer with 1975 turns of copper wire. Table 4.2. shows the geometrical parameters of the solenoid.
Various tests were carried out in order to measure the magnetic field within the solenoid using a hall probe. The linear relation between the magnetic field magnitude and the

Parameter	Value
Inner coil diameter	82.0 mm
Outer coil diameter	82.848 mm
Area of uniformity (target volume)	450 cm^3
Uniformity in target region	$10^{-4}\,G/cm$
Magnetic Field	$7\,G$
Copper wire inner diameter (without insulation)	0.395 mm
Copper wire outer diameter (with insulation)	0.424 mm
Current	0.225 A

Table 4.2: Geometric parameters for the solenoid.

current in the coil was determined using the three axis magnetometer MAG–03 MS from Bartington Instruments Ltd.
The sensors provide measurements of static and alternating magnetic fields in three axes. They convert the magnetic flux density measured on three axes, into a bipolar analog voltage. Analog output voltages V_x, V_y and V_z are in linear proportion to the flux density. Therefore, the three sensors were connected to three different channels in a voltmeter. The current in the coil was provided by a Goodwill DC power supply. The power supply was set up to run in current mode, which produced 0.225 A of current and 15 V. The resistance of the solenoid was measured directly and was found to be 65.3 Ω. In Table 4.3 are shown the calculated and measured circuit properties of the solenoid. In this study,

Parameter	Calculated	Measured
Total current	0.225 A	0.224 A
Voltage drop	15.05 V	14.92 V
Resistance	68.42 Ω	65.3 Ω
Power	3.311 W	3.28 W

Table 4.3: Calculated and measured circuit properties of the solenoid

a right–handed coordinate system with the positive *z-axis* pointing along the field produced by a positive current was chosen. The positive *y-axis* pointed vertically upward. It is mandatory to know the exact position of the sensor element with respect to a point of reference. In this case, the point of reference was chosen to be the center of the solenoid. The solenoid and the test arrangement are shown in Fig. 4.10. Afterwards, the magnetic field inside the solenoid was measured. This measurement of the field was performed for three different positions of the gaussmeter, one along the axis in the center of the solenoid and another two at 1 and 2 cm off axis. In the measurement of the normal components of

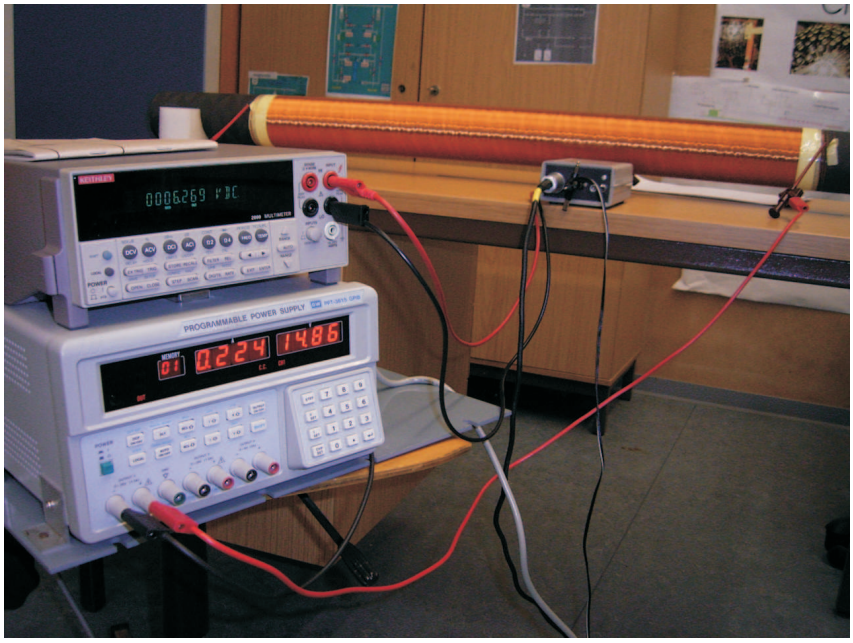

Figure 4.10: Overview of the solenoid with the electronic setup used to perform the test measurement.

the field, the superposition of the earth magnetic field with a magnitude of ~ 0.5 G was seen .
Fig. 4.11 displays the result obtained in this measurement for the magnetic field which is ~ 7 G over the target cell region. The measured relative field gradient along the axis is smaller than $5 \cdot 10^{-4} cm^{-1}$ as it can be seen in Fig.4.12.

4.4.4 External Magnetic Holding Field

Due to the constraints in the available space inside the Crystal Ball tunnel region, the gas polarisation degree had to be measured outside the Crystal Ball detector during the data taking phase. Thus, it was also necessary to provide a region having a uniform magnetic field outside CB during the polarimetry measurement. For this purpose, a pair of Helmholtz coils was designed and constructed.
As in the solenoid case, the strength and uniformity of this field were the most important parameters to be taken into account. In order to prevent the depolarization of the gas when the target cell was transfered from the solenoid to the Helmholtz coils, the gradient-to-field ratio of the coils should be less than $10^{-4} cm^{-1}$ for a magnetic field of approximately $7\,G$.
Also in this case, numerical calculations of the field and gradients of the Helmholtz coils

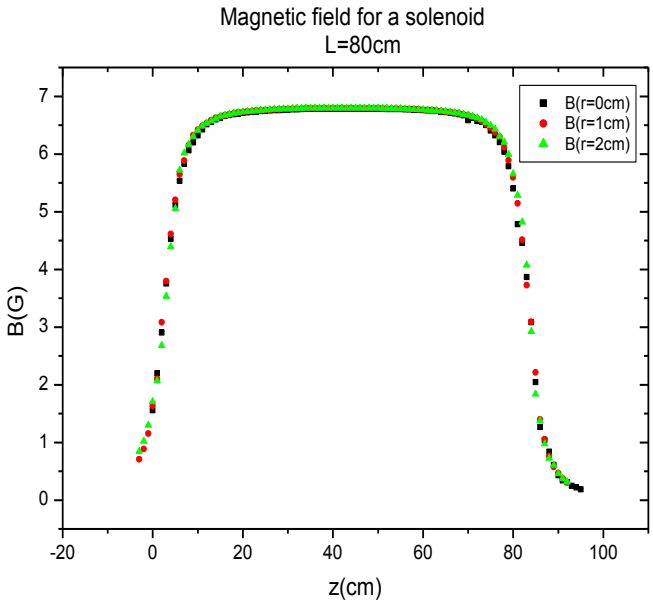

Figure 4.11: Measured magnetic field for the 800 mm solenoid.

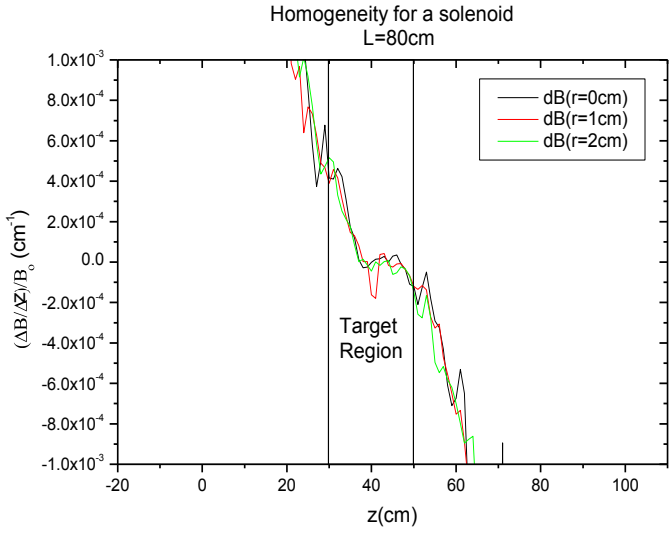

Figure 4.12: Measured homogeneity of the magnetic field for the 800 mm solenoid.

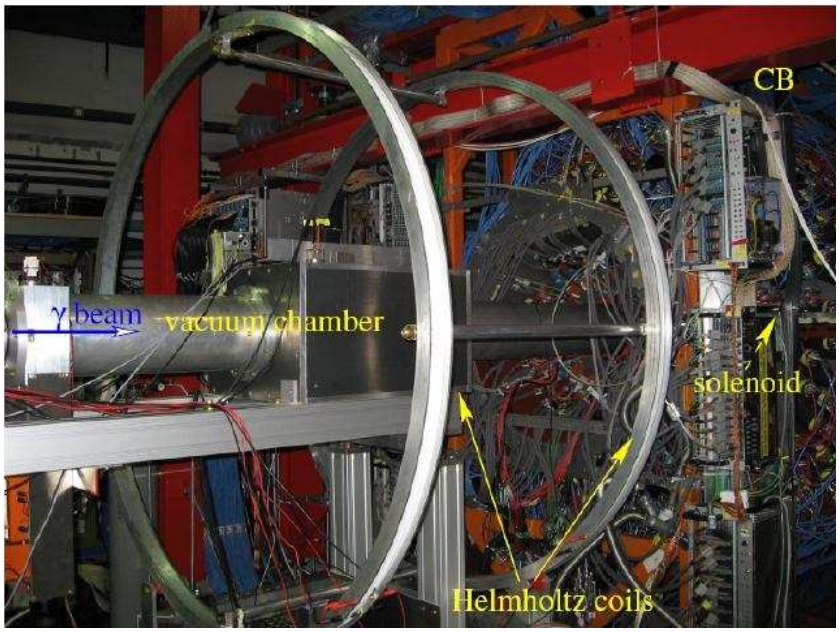

Figure 4.13: Helmholtz coils located upstream of the Crystal Ball.

were carried out with the finite element code FEMM and with the information obtained by the simulation, two coils with 160 cm diameter each were manufactured. Table 4.4. shows the main parameters of the coils. The coils were wound on an aluminium support in order to avoid spurious field gradients and were located upstream of the Crystal Ball, as it can be seen in Fig. 4.13. The system also comprises the vacuum chamber containing the additional coils needed or the polarimetry measurement.

Various tests were carried out in order to measure the magnetic field within the coils using the same three axis magnetometer MAG–03 MS from Bartington Instruments used for the solenoid. In these tests it was seen that the iron frame of the Crystal Ball produced

Parameter	Value
Coils diameter	160 cm
Copper wire diameter	0.2 cm
N° of windings	150
Uniformity in target region	$10^{-4} cm^{-1}$
Magnetic Field	$7\,G$
Current	4 A

Table 4.4: Main parameters for the Helmholtz coils.

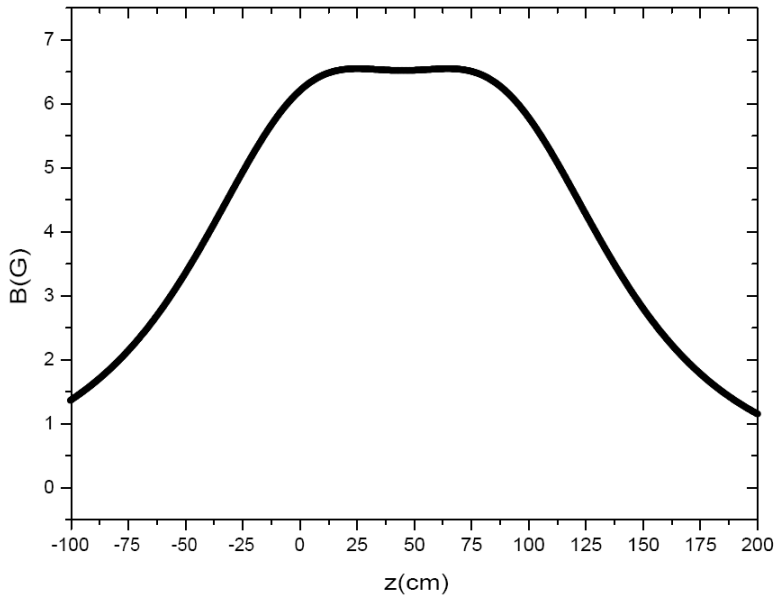

Figure 4.14: Measured magnetic field for the Helmholtz coils.

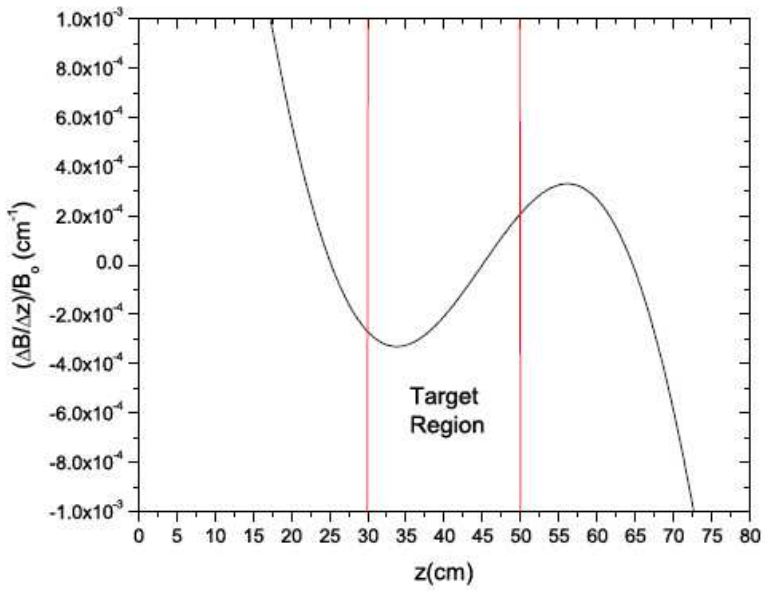

Figure 4.15: Measured homogeneity of the magnetic field for the Helmholtz coils.

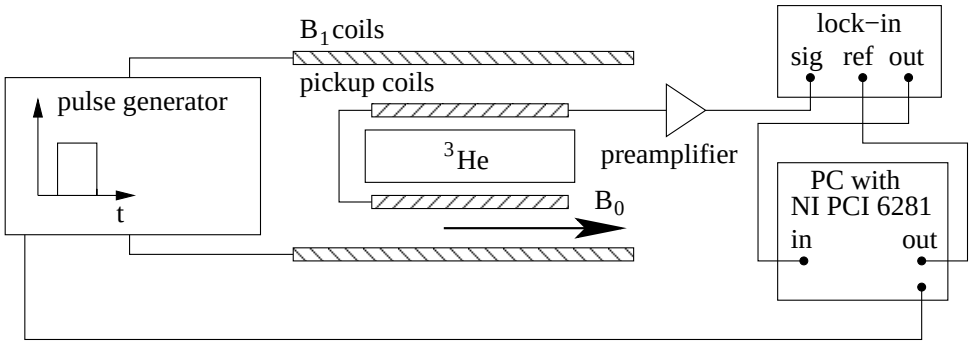

Figure 4.16: Diagram of the electronics and components used during typical NMR polarimetry measurements.

some gradients in the Helmholtz coils. Thus, it was necessary to add five extra windings with separate power supply to the coil that was closer to the CB frame in order to optimize the NMR signal.
In Fig. 4.14 and Fig. 4.15 the results obtained in these measurements for the axial magnetic field and homogeneity of the coils, respectively, are shown. The measured magnetic field in the target cell region is $\sim 7G$ and the relative field gradient along the axis is less than $3 \cdot 10^{-4} cm^{-1}$ which is very similar to the required value.

4.5 Polarimetry Measurement

The measurement of the ^{3}He polarisation was carried out via a NMR (Nuclear Magnetic Resonance) technique. The setup used for the polarimetry measurement is shown in Fig. 4.16. The external magnetic field B_0 produced in the z-direction by the Helmholtz coils provides a quantisation axis along which the ^{3}He spins are oriented. A static pulse with a duration of 2 s and an amplitude of 120 mG is applied perpendicular to the holding field B_0 via the rectangular B_1 coils (30 x 40 cm, 10 windings). The rising and the trailing edge of the pulse have a rise time of 20 μs, which is a prerequisite for the process to be nonadiabatic at a Larmor frequency of 14.5 kHz. Hence, the ^{3}He spins cannot follow the sudden tipping of the total magnetic field ($\vec{B_0} + \vec{B_1}$). Therefore, a transverse component of the magnetization occurs at the leading and trailing edge of the B_1 pulse which gives rise to an induced voltage (free induction decay (FID) signal) in the pick up coils. For practical purposes the FID signal at the trailing edge is recorded via an ADC card, as the total field gradients are smaller when B_1 is off, resulting in longer transverse relaxation times T_2. The signal of the pickup coils first passes a resonance preamplifier which is tuned to the Larmor frequency of ^{3}He and which has a quality factor of 7. Then, the signal

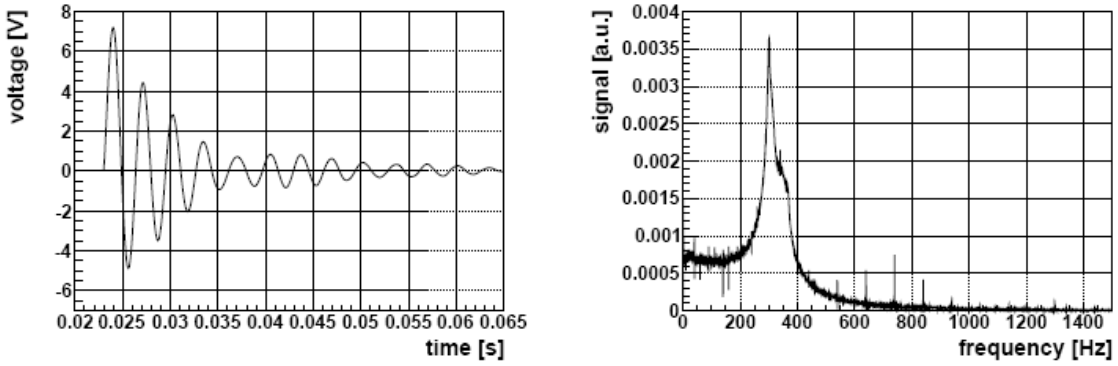

Figure 4.17: The FID signal (left) produces, after a Fourier transformation, a peak spectrum(right).

from the preamplifier is fed into a lock-in amplifier (Stanford Research SR8 10 DSP) to improve the signal-to-noise ratio. The reference frequency close to the Larmor frequency is generated by a NI PCI 6281 card. This ensures a stable phase of the outgoing signal. The reference frequency is chosen in such a way that the beatfrequency of the outgoing signal is around 100 Hz.
The FID signals in the time domain (signal amplitude as a function of time) can be converted into frequency domain signals (amplitude versus frequency) using the Fourier Transform (see Fig.4.17). The B_1 pulse results in a flip angle of $\alpha \approx 2^\circ$ and the relative polarisation loss amounts to 0.02% per pulse. Due to the small flip angle and the small polarisation losses the described method can be used for frequent monitoring of the polarisation in parallel to the ordinary data taking. The area under the Fourier peak in the Fourier spectrum is proportional to the polarisation. The signal amplitude (free induction decay) yields only a relative measurement of the polarisation, but a fit to the exponential decay gives a value of the T1 (relaxation) with a very high precision.
During the ^{3}He beamtime, the decay of the longitudinal magnetisation was periodically monitored every 2 hours. In Fig. 4.18 the polarisation values as a function of the time for the whole ^{3}He beamtime are shown. The blue points correspond to the values obtained from the FID measurement. The relaxation values improved significantly from the first days of the beamtime, when the T_1 was around 6 hours compared to the 20 hours obtained at the end of the beamtime.
The yellow points of Fig. 4.18 represent the results of the exponential parametrization that is in agreement with the experimental points, thus there were no additional relaxation terms under beam conditions.

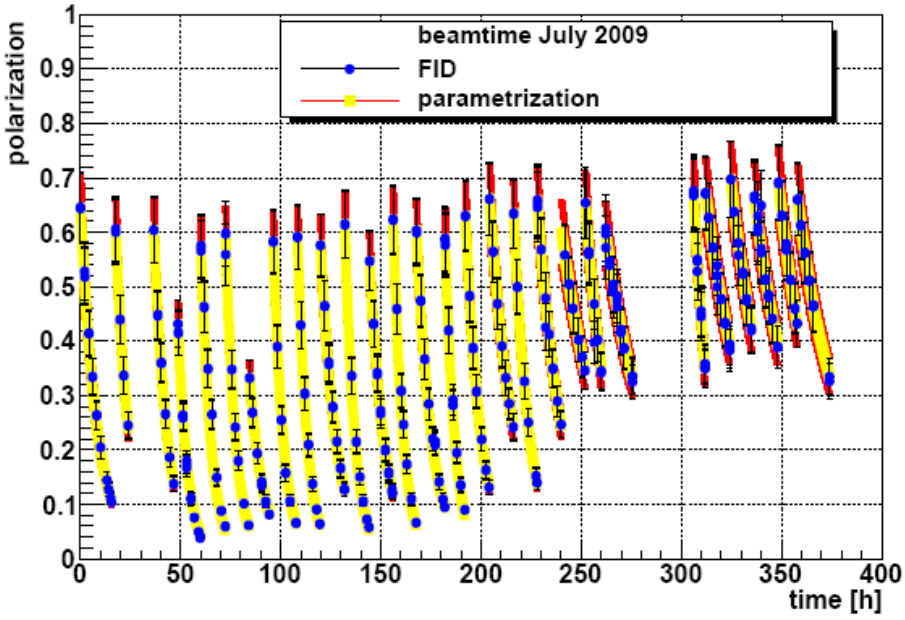

Figure 4.18: Polarisation as a function of the time for the ^{3}He beamtime.

Chapter 5
Experimental Method

5.1 Total Inclusive Cross Section Measurement

Because of the low final state multiplicity, two different methods can in principle be used to measure the total photoabsorption cross section (σ_{tot}) in the photon energy range 150 $\leq \nu \leq$ 800 MeV:

1. The "partial channel method" in which the evaluation of σ_{tot} is based on the identification and sum of all partial channels for photoproduction and photodisintegration.

2. The "inclusive method" consisting in the direct determination of σ_{tot} by measuring the total number of hadronic events detected.

However, different multiparticle final states are obtained from the photoabsorption processes. These multiparticle final states are difficult to detect individually and have quite different acceptances and detection efficiencies. Therefore, it is advantageous to measure the total photoabsoption cross section inclusively, since the systematic uncertainties arising from unobserved final states are minimised in this approach.
For this reason, it is necessary to detect at least one reaction product of any of the possible hadronic final states with as high as possible solid angle acceptance and efficiency. The corrections needed to evaluate the detector efficiencies and the loss of events emitted in the angular/momentum regions not covered by the detector have to be estimated using models. This loss of events due to the limited acceptance has to be kept as low as possible to minimise model dependent contributions. Thus, in the total inclusive cross section measurement, it is not necessary to identify individual processes, since what is needed is the reliable detection of charged particles and a high efficiency for the hadron neutral decay modes.
The CB-TAPS detector, which covers 97% of the 4π solid angle and with a detector efficiency $\geq$99% for both charged hadrons and photons coming from neutral meson decays, is well suited for this measurement.

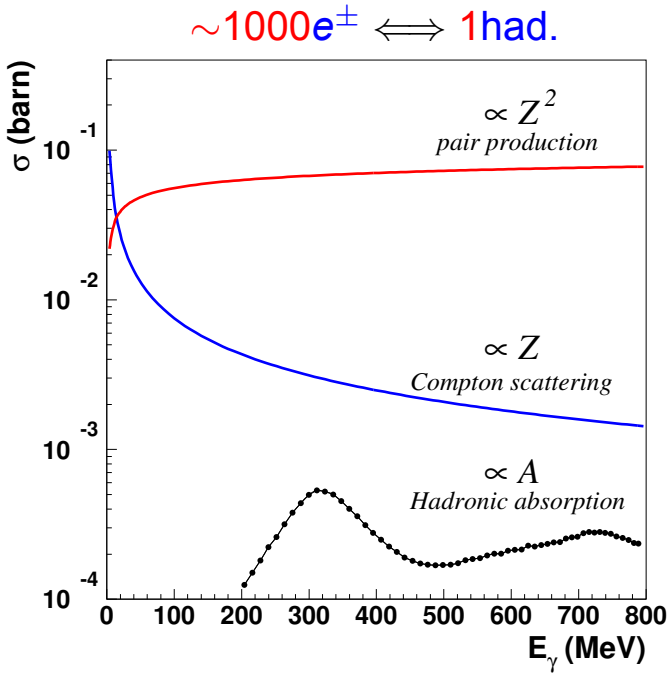

Figure 5.1: Total cross sections on Hydrogen of the electromagnetic background processes as a function of the photon energy compared to the total hadronic cross section.

5.2 Trigger Conditions

In order to have the maximum efficiency, the trigger condition required for a total inclusive cross section measurement is to detect at least one charged or neutral hadron in CB or TAPS, with the lowest possible threshold energies, i.e, ∼20 MeV for CB and ∼40 MeV for TAPS.
Due to these open trigger conditions, it is essential to suppress the electromagnetic events coming from pair production of electron and positron in the Coulomb field of the atomic nuclei and Compton scattering off orbital electrons of the atoms, since it represents the overwhelming part of the reaction products from the photon beam interactions with the target materials. As it can be seen in Fig. 5.1, the electromagnetic cross section is several orders of magnitude larger than the hadronic processes.
This background, which is much more enhanced in forward direction than the hadronic events, has to be on-line suppressed by about 3 orders of magnitude in order not to pollute the hadronic processes significantly. This rejection of the e.m background can be performed by means of the threshold Cherenkov counter located in the forward polar angle region that has been previously described in section 3.6.

Chapter 6
Data Analysis

In March 2009 a feasibility test for a total inclusive measurement using an unpolarised liquid hydrogen target was performed at MAMI. The aim of this measurement was to test the detector response and the trigger conditions to be applied later to the polarised data. The comparison between the total inclusive cross section obtained in this measurement to the existing results from previous experiments can also be used as a reference in order to test and develop the analysis procedures.
Later, in July 2009 a measurement was carried out using a polarised ^{3}He gas target in combination with the circularly polarised photon beam of MAMI. This was the first doubly polarised photoproduction experiment on ^{3}He. The data obtained in this experiment provide information on the photoreactions on polarised free neutrons and can be used for the experimental check of the fundamental GDH sum rule on the neutron.
The procedure for the analysis of both the unpolarised and the polarised data used to obtain the total photoabsortion cross section on the neutron are presented in this chapter.

6.1 Cross Section Evaluation

In the most general case, the cross section for any photoreaction can be written as:

$$\sigma(E_\gamma) = \frac{N(E_\gamma)}{\mathcal{L}(E_\gamma)}, \tag{6.1}$$

where $N(E_\gamma)$ is the number of reaction events with a corresponding photon energy E_γ and $\mathcal{L}(E_\gamma)$ is the integrated luminosity of the reaction. Taking into account that the detection efficiency of a real detector setup is below unity, the number of reaction events is given by:

$$N(E_\gamma) = \frac{N_{det}(E_\gamma)}{\epsilon_{det}(E_\gamma)}, \tag{6.2}$$

where $N_{det}(E_\gamma)$ is the number of detected reaction events and $\epsilon_{det}(E_\gamma)$ is the detection efficiency of the setup.
The integrated luminosity is determined by the particular experimental setup used and is defined as:

$$\mathcal{L}(E_\gamma) = N_\gamma(E_\gamma) \cdot N_{target} \cdot d_{target}, \tag{6.3}$$

with $N_\gamma(E_\gamma)$ the number of photons with energy E_γ impinging on a target of thickness d_{target} and N_{target} the number of target nucleons per unit volume which is given by:

$$N_{target} = \frac{\rho N_A}{A} \tag{6.4}$$

where ρ is the target material density, $N_A = 6.022 \cdot 10^{23}\ mol^{-1}$ is the Avogadro's number, and A is the atomic mass of the target material.
Therefore, one obtains for the total cross section the following expression:

$$\sigma(E_\gamma) = \frac{N_{det}(E_\gamma)}{N_\gamma(E_\gamma) \cdot \rho N_A/A \cdot d_{target} \cdot \epsilon_{det}(E_\gamma)}. \tag{6.5}$$

6.2 Event Selection Procedure

The procedure to determine an experimental cross section from the raw data obtained by the experimental data acquisition follows some steps:

1. Data reduction. A calibration has to be done to convert the raw electronic signals recorded by the QDCs and TDCs from the different detector elements into real physical quantities related to the detected particles as emission angles or deposited energies. The values recorded by the QDCs are thus converted to energies in MeV and those recorded by the TDCs are converted to time in ns.

2. Cluster algorithms. In order to group together the detector hits originating from the same incident particle, a cluster algorithm has to be applied to the data from the Crystal Ball and TAPS.

3. Random events subtraction. The contribution of events due to accidental hits inside the tagger, i. e, random events that have no proper electron-photon time correlation are subtracted from the total number of selected events.

4. Geometrical cuts. If needed, some geometrical and energetical cuts have to be applied.

5. Empty-target subtraction. Subtraction of the empty target to the full target data to ensure that all the events originate from the target material only.

6. Evaluation of correction factors and efficiencies. The total number of selected events has to be corrected for the detection inefficiencies of the setup and for the events lost in the software selection procedure, $\epsilon_\gamma(E_\gamma)$, by means of simulations.

7. Evaluation of the cross section. Taking into account the detector efficiencies, once the number of good events has been selected and the contribution of accidental events has been subtracted, the cross section can be evaluated (Eq. 6.5).

In the case of a double polarisation experiment, like the one treated in this thesis, it is necessary during the data analysis to additionally take into account the degrees of polarisation of both the target (P_t) and of the photon beam (P_γ). The evaluation of the target polarisation for the ^{3}He experiment is explained in detail in section 3.3.3. As it is shown in that section, the degree of photon polarisation is obtained using a Møller polarimeter.
The above mentioned procedure will be explained in more detail in the following sections.

6.3 Tagger Calibration

6.3.1 Photon Beam Energy Calibration

The energy of the resulting photon beam produced by MAMI has a flux curve over a range of energies with an intensity which closely follows $1/E_\gamma$ as it can be seen in Fig. 6.1. Therefore a precise determination of the photon beam energy requires an accurate knowledge of the incident electron beam energy which is defined by the microtron settings. Accurate energy measurements were performed with this purpose by the MAMI operators at intervals of few days. Then, this information is used to infer the energy of the tagged photons from the incident electron beam energy E_0 and the measured energy of the recoiling bremsstrahlung electron E_{e^-} in the tagger focal plane detector as given in Eq.(3.1)
The energy of the bremsstrahlung electron is determined from its hit position in the Tagger focal plane detector. A calibration of the correspondance between hit position and beam energy is performed by a ray tracing in an equivalent uniform field using a computer program [111], [112].
This program is based on a field map measured along the main beam trajectory that is applied as an equivalent uniformed field. The strength of this uniform field is measured using an NMR probe which is positioned inside the tagger magnet.
The structure of the focal plane detector frame defines the focal plane detector array. Thus, using a map of positions and angles of the individual focal plane scintillators, the program follows a χ-squared minimisation routine to find the bremsstrahlung electron energy which passes directly through the center of each tagger scintillator.The relationship

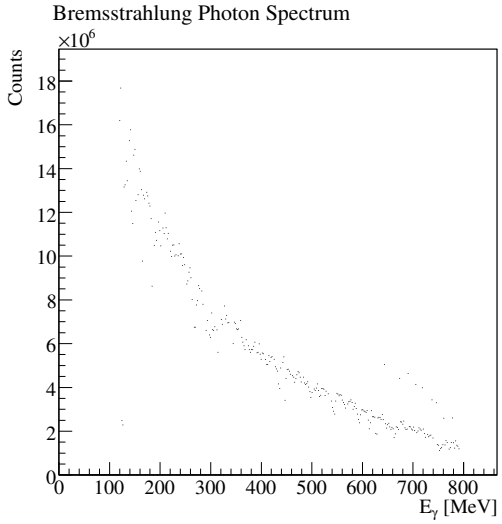

Figure 6.1: Calibrated photon energy flux spectrum.

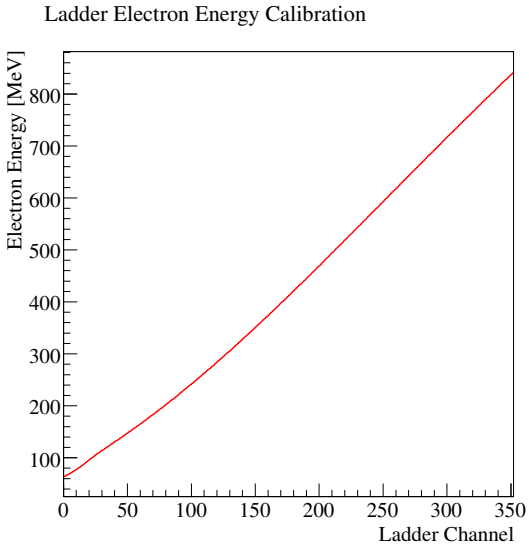

Figure 6.2: Tagger Calibration.

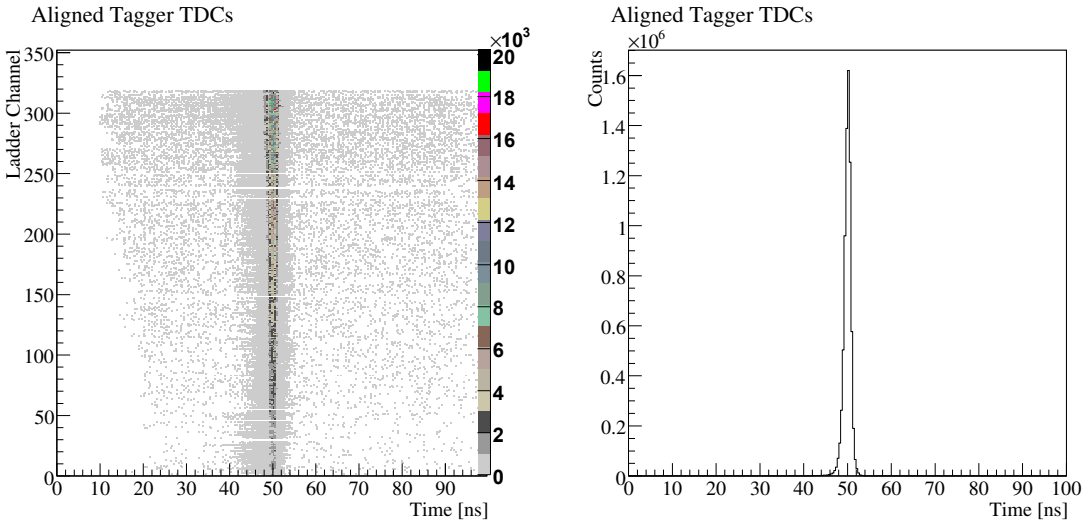

(a) Aligned tagger TDCs.

(b) Projection of (a).

Figure 6.3: Tagger timing alignment.

between the electron energy and the corresponding focal plane detector element calculated for an NMR value of 1.049 T is shown in Fig. 6.2.
The NMR measurement is monitored for each individual beamtime to ensure that the Tagger calibration has not been changed.

6.3.2 Timing Alignment & Calibration

The channel to time conversion for each tagger TDCs is set by the TDC modules (Time to Digital Converters) and has been established as ∼0.18 ns/channel [59]. To facilitate uniform cuts on the combined timing spectrum from the complete focal plane array, it is required that all the individual tagger channels are aligned such that the peaks related to the experimental trigger ("prompt" peak) of all elements are coincident at the same point in each TDC time spectrum (see Fig.6.3).
This channel alignment is performed by fitting a Gaussian distribution to the prompt peak of each channel. This is obtained using experimental data from low intensity tagging efficiency runs where the Crystal Ball and TAPS are left out of the DAQ and the experimental trigger is made by an ∼100% efficient Pb-Glass detector placed in the photon beam downstream of the target (see section 3.3.2). Due to the low intensity electron

beam, the resulting timing spectrum is dominated by the prompt peak since the number of random coincidences in the tagger focal plane detector is minimised. Then, the mean of the Gaussian is determined and a constant time offset is applied to shift the mean of each channel to the same arbitrary time.
This alignment can be used for a whole run period and in the data analysis, instead of selecting channel-by-channel a single set of 'prompt' and 'random' time windows can be applied to the entire Tagging Spectrometer.

6.4 Photon Cluster Algorithm

The final state particles of an event deposit energy in the CB producing an electromagnetic shower which in ∼98% of events spread their energy among a cluster of adjacent crystals. To reconstruct such a shower, the cluster algorithm identifies groups of crystals with energy deposited originating from the same incident photon. For this, it first finds the crystal with the largest energy deposit and then considers additionally its 12 neighbouring crystals (see Fig. 6.4).
Then the sum of the energies in each of the 12 crystals is taken as the deposited energy

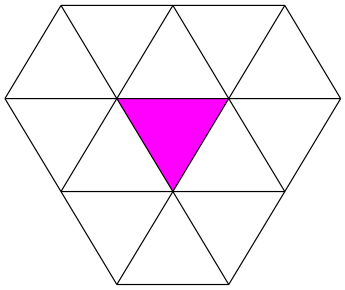

Figure 6.4: NaI cluster in CB. Each triangle represents one crystal. The central crystal is the one with the highest energy and its surrounded by the 12 nearest crystals which could be part of a cluster.

in any cluster. A minimum energy deposit in a crystal is necessary to be counted as part of a cluster in CB. Also, a total minimum cluster energy is required in order to prevent that a split off cluster is treated as a separate cluster.
The location of a cluster in the CB is calculated as a weighted sum of each of the cluster elements (relative to the center of the CB) and the energy deposition in that crystals.

Thus, the reconstructed hit position, X_{rec} can be calculated as:

$$X_{rec} = \frac{\sum_i^N x_i \sqrt{E_i}}{\sum_i^N \sqrt{E_i}} \tag{6.6}$$

where x_i refers to the x-coordinate of the crystal, E_i is the energy deposited in the i-th crystal and N is the number of crystals in the cluster. Taking into account the cluster locations, energies deposited for an event, photon directions and the incoming photon beam information obtained fron the Tagger, one can determine the different particle reactions.

6.5 Random Subtraction

The CB and all additional detector triggers are placed in coincidence with the tagger to relate each event with the photon energy that induces the reaction. The time registered by the TDC modules for each element of the focal plane detector corresponds to the relative time difference between the hit in the tagger element and the detector event. To separate photon induced reactions from accidentals seen in the detector setup, only events that appear in coincidence with the detection of an electron inside the tagger spectrometer within a certain time window are accepted.
The photon induced events enabling the trigger have a constant time difference, since the electrons and photons travel with the speed of light. This time difference is related to the time of propagation of the photon from the radiator to the target and the time taken for the produced particles to make the experimental trigger. Hence, these events will appear at similar time differences in the TDC spectra producing a prominent peak as it can be seen in Fig. 6.5. Two regions with the same time width are defined in this TDC spectra to correct for accidental time coincidences. Region 2 in Fig. 6.5 contains only the random background, i.e, electrons which are not associated with the photon producing the experimental trigger while region 1 includes both, the accidental background and the well correlated events.
The contribution of the random background in region 1 can be corrected taking an appropriately weighted sample of the random events in regions 2 and subtract them from the events of region 1.
To improve the statistical error of this procedure the possible multiple hits in the tagger have to be taken into account. There are basically two possible sources for this:

1. One electron that produces a Bremsstrahlung photon enters the Tagger and by multiple or Moller scattering hits more than one focal plane detector. This effect can be recognised and corrected since all the hit tagger channels are in an adjacent tagger detector. This correction can be done taking into account the tagger channel with the correspondent highest photon energy, since, due to geometrical reasons,

the electrons are preferably scattered into tagger channels that belong to higher electron energies and hence lower photon energies.

2. One or more random electrons enter the tagger within the coincidence time interval together with a possibly 'good' electron. These events can be recognised by multiple hits in non-adjacent tagger channels and must be treated individually by the random subtraction method described above.

As a result, for each detected event in CB or TAPS, there is the possibility to have more than one electron hit detected by the Photon Tagger. Specially at the electron currents used for the ^{3}He experiment, the probability of having two or more electrons per trigger is not negligible. Therefore, this effect was also taken into account in the time window selection as it can be seen in Fig. 6.5, where the multihit effect is illustrated by the red region.

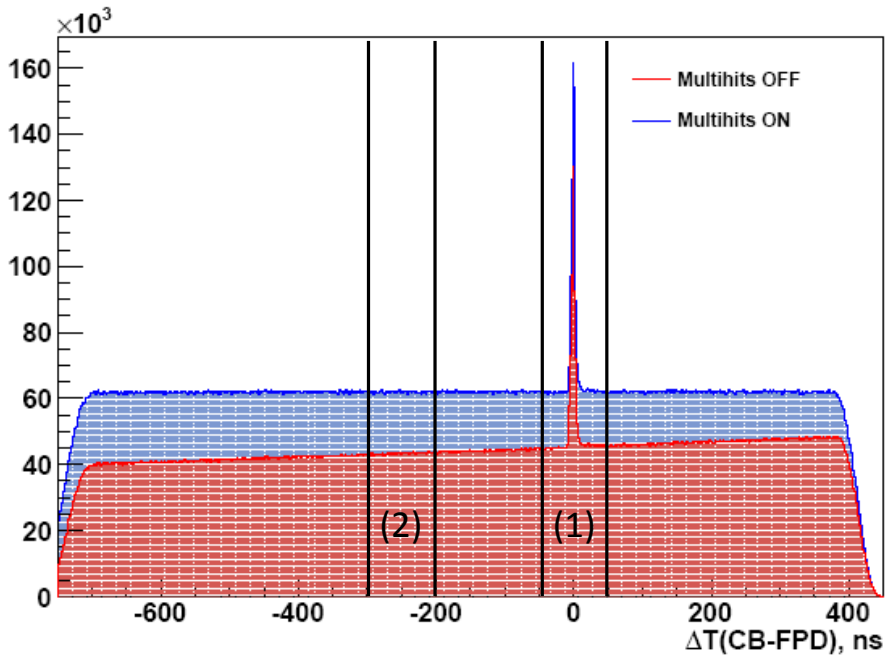

Figure 6.5: Time-difference spectrum for all tagger focal plane channels with respect to Crrystal Ball. The region (1) contains the prompt events. The region (2) contains only the accidental events.

6.6 Total Photoabsorption Cross Section on Unpolarised Hydrogen

Prior to the polarised ^{3}He experiment, another measurement was carried out using an unpolarised liquid hydrogen target. In this unpolarised measurement, the trigger conditions and the analysis procedure applied were used later as a reference to get the total cross section for the polarised ^{3}He measurement. As it was described in section 6.1, the total inclusive photoabsorption cross section for the unpolarised hydrogen measurement can be written as:

$$\sigma(E_\gamma) = \frac{Experimental\ yield\ in\ a\ 4\pi\ angle}{(number\ of\ photons)(number\ of\ target\ nucleons/area)}$$

This can also be expressed as Eq.(6.5).
For this measurement, the CB trigger as discussed before in section 5.2, required the presence of at least one particle. However, these open trigger conditions were not implemented yet in TAPS, thus the presence of at least two particles inside TAPS was required. Around 10% of the CB and around 75% of the TAPS raw triggers were eliminated by the online Cherenkov veto conditions.
In Fig. 6.6 the total inclusive cross section obtained from the unpolarised hydrogen data is shown and compared to the existing previous data. In this plot the red points correspond to the CB data that were obtained without any event selection apart from the subtraction of the tagger random coincidences. The blue points are the previous results corrected for the detector acceptance and for the trigger inefficiencies taking only into account single pion photoproduction channels.
As it can be seen in Fig. 6.6, our data are very well in agreeement with the results obtained in previous experiments for E_γ below 500 MeV, the energy region in which only the $\gamma p \rightarrow N\pi$ channels play a relevant role. In the region 500 MeV $< E_\gamma <$ 0.8 GeV, where a slight discrepancy can be seen with previous data, the $\gamma p \rightarrow N\pi\pi$ channels start to play a relevant role. Since they are still close to threshold, there is a non-negligible loss of strength inside our detector acceptance that has not been corrected yet and that explains the observed feature. For $E_\gamma > 0.8$ GeV values, many multi-pion production channels start to be effective and, due to the very large detector acceptance, at least one photoemitted hadron is detected. For this reason, there is no loss of efficiency for these channels as it is demonstrated by the good agreement that is again present with previous data at $E_\gamma > 0.8$ GeV.
This result give us confidence in the validity of the algorithms applied for the total cross section evaluation. These algorithms could then be also applied, only with slight modifications, to the data obtained in the polarised ^{3}He measurement.

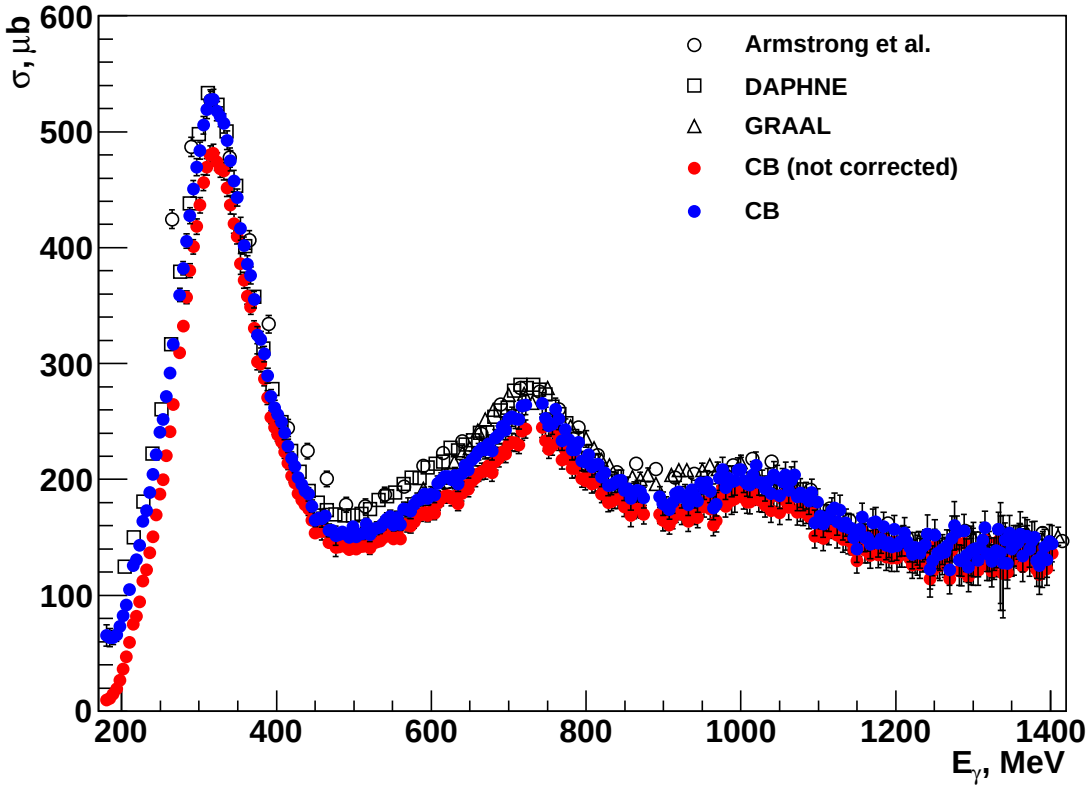

Figure 6.6: Unpolarised total inclusive cross section on hydrogen compared with the existing published data of ref. [113] (circles); ref.[114] (squares) and ref.[115] (triangles). The red points correspond to the CB data obtained without any event selection appart from the subtraction of the tagger random coincidences. The blue points are the CB data corrected for the detector acceptance and the trigger inefficiencies. Only statistical errors are shown.

6.7 Total Photoabsorption Cross Section on Polarised ^{3}He

The analysis of the doubly polarised data obtained using a circularly polarised beam and a longitudinally polarised ^{3}He gas target are presented in this section. The results of this measurement are the first of their kind since such an experiment had never been carried out before. The observables of interest are the total inclusive photoabsorption cross sections for the two relative alignments of the photon helicity and the ^{3}He spin. The cross section corresponding to the parallel polarisation orientation (spin 3/2 state) is denoted as $\sigma_{3/2}$, while the cross section in the antiparallel case (spin 1/2 state) is written as $\sigma_{1/2}$. Only the measurement of the difference $\Delta\sigma^{pol} = \sigma_{3/2} - \sigma_{1/2}$ is needed in order to obtain experimental information about the GDH sum rule on the neutron.
The helicity dependent total photoabsorption cross section difference $\Delta\sigma^{pol}(E_\gamma)$ can be determined by the following equation:

$$\Delta\sigma^{pol}(E_\gamma) = \sigma_{3/2}(E_\gamma) - \sigma_{1/2}(E_\gamma) = \frac{N^H_{3/2}(E_\gamma) - N^H_{1/2}(E_\gamma)}{\mathcal{L}(E_\gamma)} = \frac{\Delta N^H(E_\gamma)}{\mathcal{L}(E_\gamma)}, \tag{6.7}$$

where $\mathcal{L}(E_{\gamma)}$ is the integrated luminosity and $\Delta N^H(E_\gamma)$ is the difference of the experimental yields of events with hadronic reaction products with different polarisation orientations within the full 4π solid angle region. The evaluation of the integrated luminosity $\mathcal{L}(E_{\gamma)}$ is carried out using the method outlined in section 6.1.
The selection of events in the 3/2 and 1/2 helicity states was performed following the same procedures as in the unpolarised analysis explained in section 6.6. Then, in order to obtain the $\Delta\sigma^{pol} = \sigma_{3/2} - \sigma_{1/2}$ difference, these number of events are normalised and subtracted.
In the case of the polarised analysis procedure, only few modifications with respect to the unpolarised analysis have to be done. Mainly, the parameters related to the target (dimensions, composition, density) need to be modified and the beam and target polarisation values need to be included in the analysis and each event is now weighted by their inverse product.
Including the polarisation parameters in Eq.(6.5), the total polarised cross section can be written as:

$$\sigma(E_\gamma) = \frac{1}{P_{target} \cdot P_\gamma} \frac{N_{det}(E_\gamma)}{N_\gamma(E_\gamma) \cdot \rho N_A/A \cdot d_{target} \cdot \epsilon_{det}(E_\gamma)}. \tag{6.8}$$

where P_{target} and P_γ are the target and beam polarisation, respectively. The particular helicity-spin orientation (1/2 or 3/2) is given by the knowledge of the electron spin orientation and the direction of the target polarisation.

6.7.1 ^{3}He Data Analysis

The data presented in this section were taken in Mainz in July 2009 during the first doubly polarized photoproduction experiment on ^{3}He. The measurement covered around 380 hours of beamtime. However, the hours of recorded data are less than the total time devoted to the experiment, being around 240 hours of statistics in total, since the data taking was interrupted at times for cell exchange, beam optimisation and equipment reparations as well as tagging efficiency runs.
The polarised tagged photon beam was produced via Bremsstrahlung of longitudinally polarised electrons produced by the MAMI accelerator as it was explained in section 3.2.1. In order to maximize the degree of photon polarisation, two different electron energies, E_{e^-}= 525 MeV and E_{e^-}= 855 MeV, were used. The Bremsstrahlung photons were tagged using the Glasgow-Mainz spectrometer with an energy resolution of about 2 MeV (section 3.2.2). The experimental events analysed in this work are coming only from the main hadron detector Crystal Ball. The statistics concerning the beamtime period are given in Table 6.1.
The main principles of the analysis for the polarised data will not be repeated in this

	$E_{e^-} = 855MeV$	$E_{e^-} = 525MeV$
Data taken	30/06 to 9/07, 2009	10/07 to 17/07, 2009
Recorded data	110 hours	115 hours
Volume of data recorded	176 GB	162 GB
Photon Flux	$\sim 0.8 \cdot 10^6/sec/20MeV$	$\approx 2 \cdot 10^6/sec/20MeV$

Table 6.1: Experimental run statistics.

section, since the analysis procedure used to obtain the total inclusive photoabsorption cross section is the same as the one used for the analysis of the unpolarised data. Only the most relevant modifications of the ^{3}He data analysis will be mentioned here.
In the measurement of the total inclusive cross section all hadronic events have to be taken into account. Therefore, it was required to run with a very open trigger, i.e, with the presence of at least one particle in the CB or TAPS and with very low energy thresholds. Also, the Cherenkov online veto was used in the polarised measurement to suppress as much as possible the triggers due to electromagnetic processes.

Limitations & Background Sources

During the data taking of July 2009, there was a series of limitations and background sources for both electron beam energy periods that gave unwanted contributions to the count of events.

For the 855 MeV period the photon flux was $\sim 0.8 \cdot 10^6/sec/20MeV$, this is 50% less than what was assumed in the proposal [116]. In this case the main limitations were due to some problems in the data acquisition system. An additional problem was the low relaxation time of the target cells used in this part of the measurement. Another limitation was given by the low density of the gas inside the cell if compared with the entrance and exit windows densities. This effect can be seen in Fig. 6.7 where the z-vertex distribution is shown for all one trajectory events in a 12 hours run period with an electron beam energy of 855 MeV. In the upper part of Fig. 6.7 the red histogram corresponds to the distribution of events for a target cell full of polarised ^{3}He gas at a pressure of 3.5 bar and with two 150μm beryllium entrance and exit windows. The black histogram corresponds to an empty measurement carried out with the same target cell.
In the lower part of Fig. 6.7 one can see the difference between the measurements with full and empy target. It was expected to have 16% of the events coming from the gas/windows density ratio, however only 8% of the events are produced from the gas. This difference is mainly due to events coming from the beam halo, cosmic rays and the electromagnetic events produced in the target cell windows. The two peaks that can be seen in the plots correspond to the entrance and exit target windows that are slightly deformed because of the pressure difference in the empty and full measurements.
In the 525 MeV run period the photon flux was $\approx 2 \cdot 10^6/sec/20MeV$ as it was assumed in the proposal. Although there were also some data acquisition and detector problems the situation improved significantly with respect to the 855 MeV run period. Also the relaxation time of the target cells used in this measurements was higher. In Fig. 6.8 is shown the z-vertex distribution taken with one trajectory events for a 12 hours run period with an electron beam energy of 525 MeV. The measurement was taken with a target cell full of polarised ^{3}He gas at a pressure of 3.5 bar and with two 50μm titanium entrance and exit windows. In the upper part of Fig. 6.8 the black histogram corresponds to the events with parallel orientation while the red histogram corresponds to the events with antiparallel orientation. In order to maximise the asymmetry effects, the polar angle θ was selected within the region from 30° to 140°.
In the lower part of Fig. 6.8 the difference between the parallel and antiparallel distributions is shown. The constant fit function used inside the gas region shows a positive asymmetry effect, however the asymmetry ratio is $\sim 3 \cdot 10^{-3}$, this is roughtly equal to what it was expected.

Beam Halo Background

As it was already mentioned in the previous section, one of the main sources of background was due to the beam halo, specially for the 855 MeV run period as it can be seen in Fig. 6.9. In this figure one can see the $\theta - \phi$ correlation of the events for E_γ=

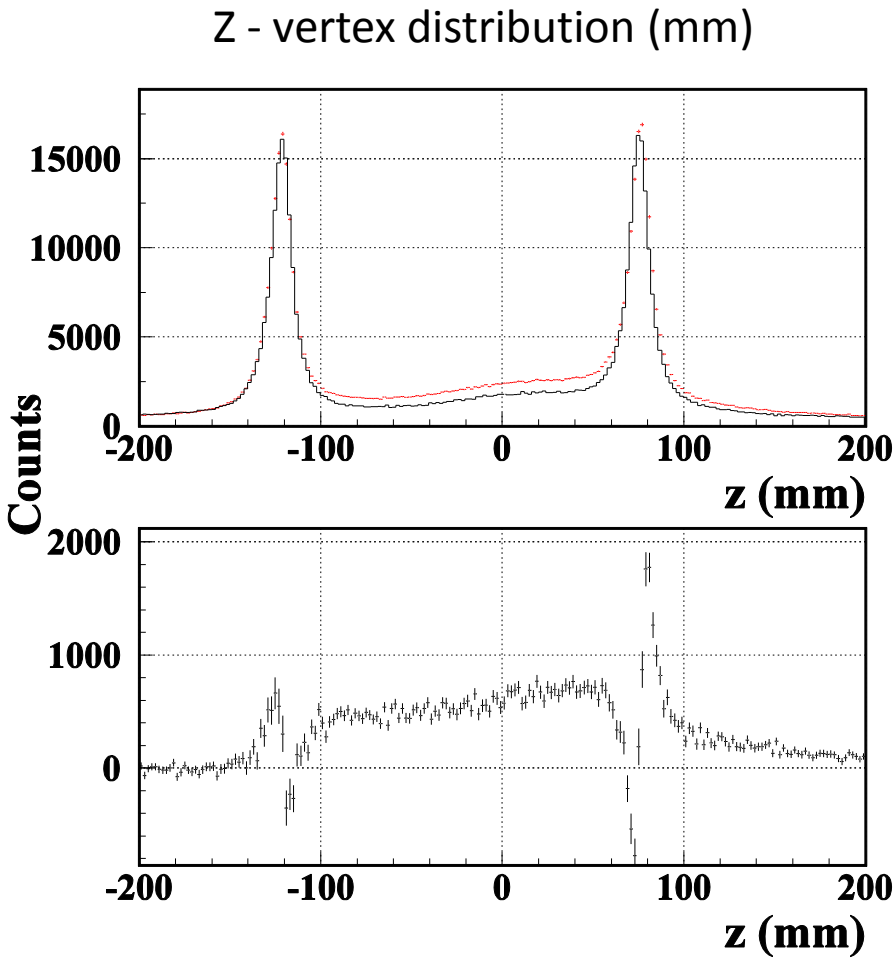

Figure 6.7: Upper plot shows the z-vertex distribution for an electron beam energy of 855 MeV and for a full(red) and empty(black) target measurement. The lower plot shows the difference full-empty target.

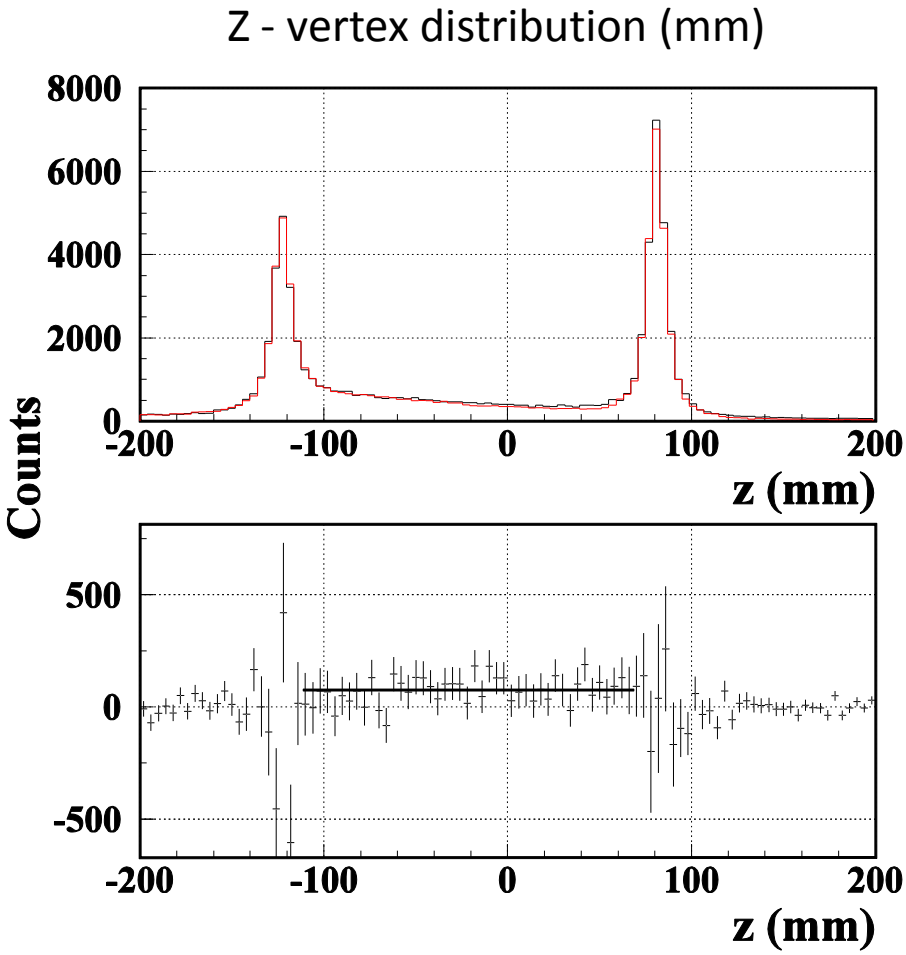

Figure 6.8: Upper plot shows the z-vertex distribution for an electron beam energy of 525 MeV for events with parallel(black) and antiparallel(red) orientation. The lower plot shows the difference parallel-antiparallel.

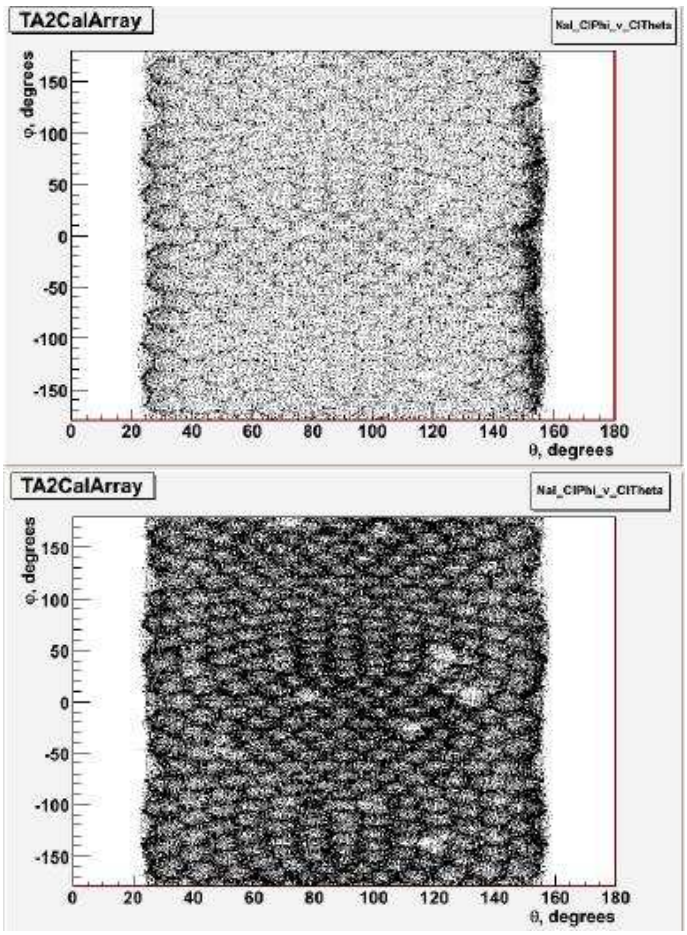

Figure 6.9: $\theta - \phi$ correlation distribution of events for $E_\gamma = 855MeV$(upper plot) and $E_\gamma = 525MeV$(lower plot).

855 MeV and E_γ= 525 MeV. The angles θ and ϕ are evaluated from the crystal position assuming that particles are emitted at z = 0. The effect of the beam halo affected the particles hitting the most upstream crystals of the Crystal Ball, i. e, the particles coming before entering the target region. One can clearly see this in the 855 MeV plot, where the distribution of events in the area around $\theta = 25^\circ$ and $\theta = 150^\circ$ is higher than in the central region. For the E_γ= 525 MeV plot, one can see that the distribution of events is more uniform, thus there was less background produced from the beam halo for the measurement at this energy.
Therefore, due to the problems exposed above and the substantial background present in the data obtained in the 855 MeV run measurement, in the following, only the data and results for the 525 MeV will be reported.

Cuts on Polar Angle and Energy

In order to minimise the background contribution due to the beam halo, some cuts in the energy and on the polar angle were applied in the data analysis. The Crystal Ball events for all the clusters with $E_{cluster} < 50$ MeV and for $\theta < 30^\circ$ or $\theta > 140^\circ$ were rejected. With these cuts the loss of efficiency is negligible but most of the background is rejected, specially in the E_γ= 855 MeV case, were the beam halo had a big contribution as it was shown in Fig. 6.9.

6.7.2 GEANT Simulations

The detector setup used during the ^{3}He experiment does not fully cover the 4π acceptance. Hence, an extrapolation needs to be performed to compensate for the missing angular (and momentum) regions.
The helicity dependent total cross section difference in full acceptance can be written as:

$$\Delta\sigma_{4\pi} = \Delta\sigma^{CB}_{(21^\circ-159^\circ)} + 2\pi \int_{0^\circ}^{21^\circ} \Delta(\frac{d\sigma}{d\Omega}) sin(\theta) d\theta + 2\pi \int_{159^\circ}^{180^\circ} \Delta(\frac{d\sigma}{d\Omega}) sin(\theta) d\theta, \qquad (6.9)$$

where $\Delta\sigma^{CB}_{(21^\circ-159^\circ)}$ is the helicity dependent total cross section difference inside the CB detector acceptance. The other two terms at the right hand side of the Eq.(6.9) have to be determined from a theoretical model. Moreover, the detector efficiencies are not 100%. Thus, to estimate and recover the lost events a simulation is needed. With this purpose a GEANT4 (GEometry ANd Tracking) simulation was used to get both the detection efficiency and the extrapolation corrections.
The GEANT package [117] uses Monte Carlo techniques to simulate reactions and interactions with detector materials. The detector and target geometry and the dimensions of its components are included in the simulation program. This code also takes into account

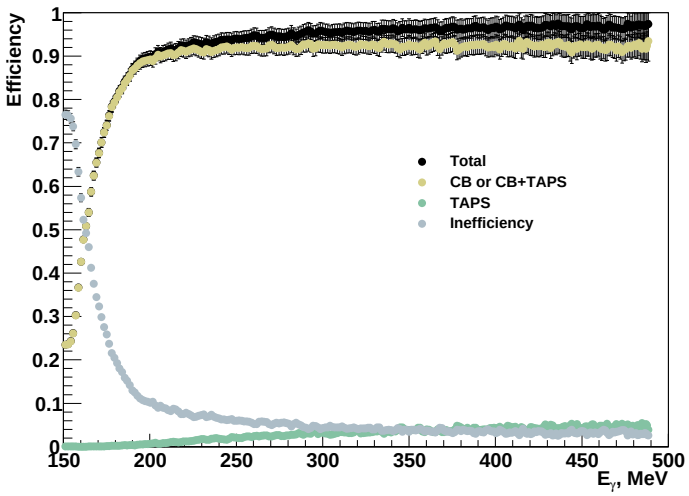

Figure 6.10: Simulated detector efficiency for the $p\pi^-$ channel at $E_\gamma \leq 525$ MeV.

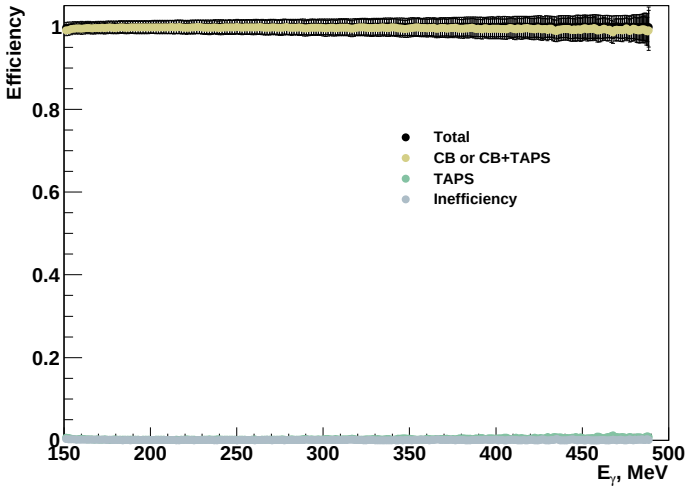

Figure 6.11: Simulated detector efficiency for the $n\pi^0$ channel at $E_\gamma \leq 525$ MeV.

the different resolutions and detection thresholds, and includes the same analysis procedures performed on the real data.
The simulated overall efficiencies obtained for the $p\pi^-$ and $n\pi^0$ channels, respectively, as a function of the photon energy at $E_\gamma \leq 525$ MeV, are shown in Figs. 6.10 and 6.11. These are simulated reactions on the quasi free neutron. In the case of the ^{3}He target, in which the spin structure is dominated by that of the neutron, and assuming that the proton polarisation cancels exactly, these are the two main channels with the larger contribution below 500 MeV.
In this energy range, the TAPS contribution for the $p\pi^-$ channel represents only $\sim 5\%$ of the detected events, while for the $n\pi^0$ channel the contribution is negligible. These single pion channels represent the most unfavorable case for the detector acceptance. When at least one additional pion is emitted in the final state, the efficiency is very close to 100% over the full angular range.
Therefore, CB alone covers most of the acceptance and in a first approximation, the evaluation of the total inclusive cross section can be determined, with a small correction factor, using only the events detected in CB.
In Fig. 6.12 the extrapolation of the helicity dependent total cross section difference to

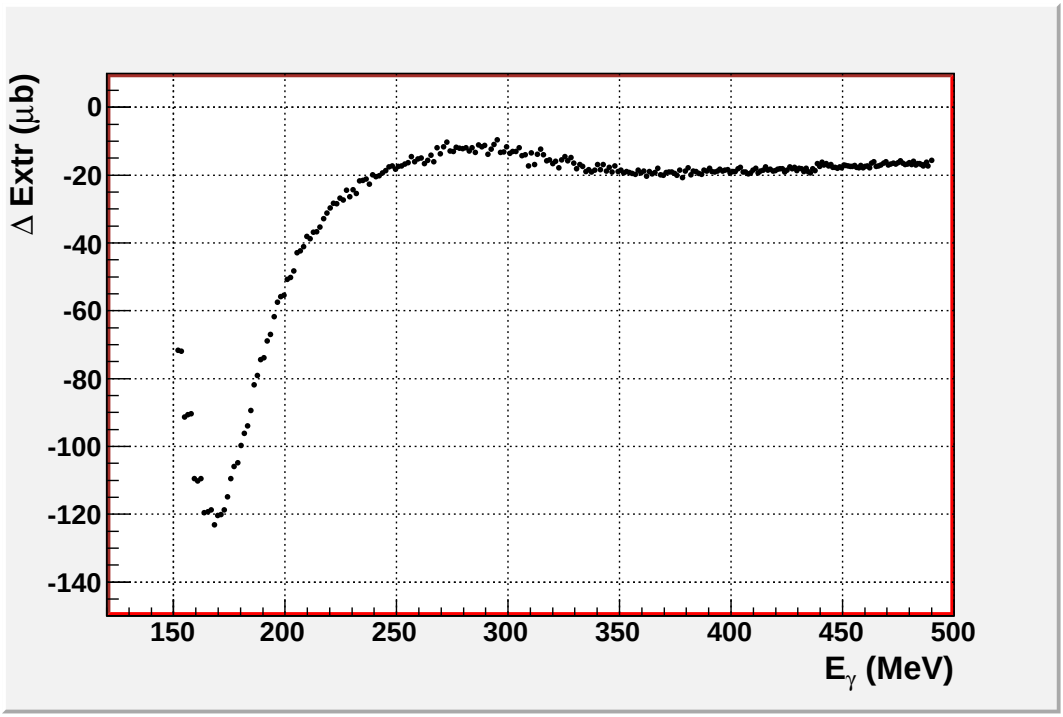

Figure 6.12: Helicity dependent total cross section difference evaluated using the MAID model for the extrapolation into the full acceptance.

4π is shown. To get this extrapolation correction it was assumed that the protons and the neutron inside the ^{3}He behave as free ones and only the effect of the different spin alignments in the components of the wave function (see Section 4.1) has been taken into account. Therefore, the overall extrapolation can be written as:

$$\Delta\sigma^{^3He} = 0.87 \cdot \Delta\sigma^n - 2 \cdot (0.026 \cdot \Delta\sigma^p) \tag{6.10}$$

where $\Delta\sigma^n$ and $\Delta\sigma^p$ are obtained from the SAID [48] and MAID [49] models.
The maximum correction is about -120 μb at a photon energy of 170 MeV. At higher energies it decreases to about -20 μb. The negative sign is due to the fact that $\sigma_{1/2}$ for the reaction $\gamma n \rightarrow \pi^- p$ is much more forward-peaked than $\sigma_{3/2}$. Therefore, the correction for $\sigma_{3/2} - \sigma_{1/2}$ due to the acceptance hole in forward direction is negative.

Chapter 7
Results

In this chapter the results from the analysis of the doubly polarised data obtained using a circularly polarised beam and a longitudinally polarised ^{3}He gas target are presented. The data were collected during the measurement performed in July 2009 with a polarised ^{3}He target for two different MAMI electron beam energy periods, one at 855 MeV and another one at 525 MeV. Due to some acquisition problems and to the substantial noise present in the data obtained in the 855 MeV run measurement, only the results for the 525 MeV period are presented. In this energy domain, the single pion photoproduction channels give almost all the contribution to the measured total inclusive cross section.
The experimental setup and the analysis procedure were described in the previous chapters. The event reconstruction and selection techniques applied to the unpolarised data described in chapter 6 were also used to obtain the total photoabsorption cross section on unpolarised ^{3}He and, with some minor modifications, in the analysis of the doubly polarised data to obtained the total photoabsorption cross section difference $\sigma_{3/2} - \sigma_{1/2}$ on ^{3}He . These results are the first of their kind since such an experiment had never been carried out before.
These data are compared with the predictions of the model of A.Fix [118-120] as well as with the SAID [48] and MAID [49], [56] models.
Finally, a comparison between the helicity dependent total cross section difference obtained from the ^{3}He measurement and the results obtained by the GDH collaboration for the proton and the deuteron will be presented in this chapter.

7.1 Total Photoabsorption Cross Section on Unpolarised ^{3}He

The total photoabsorption cross section on unpolarised ^{3}He as a function of the incoming photon energy is shown in Fig. 7.1. This result was obtained from a part of the 525 Mev data with a preliminary photon flux evaluation. These unpolarised ^{3}He data are compared

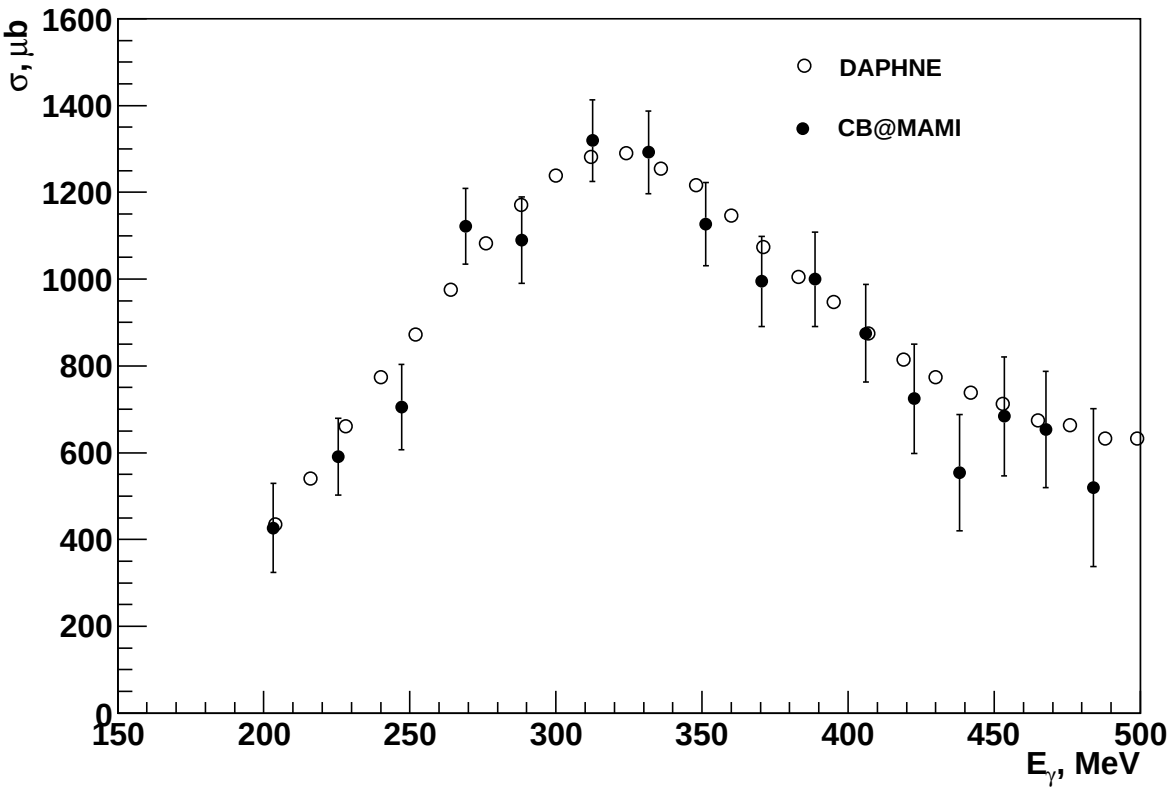

Figure 7.1: Total unpolarised photoabsorption cross section on ^{3}He as a function of the photon energy.

to the ones obtained from a previous measurement using the DAPHNE detector. The analysis procedure applied to the unpolarised ^{3}He data is the same as the one explained in chapter 6. The good agreement between the ^{3}He cross section and the previous data thus proofs the reliability of this procedure.

7.2 Helicity Dependent Total Photoabsorption Cross Section Difference on ^{3}He

In the determination of the helicity dependent total photoabsorption cross section difference on ^{3}He , the observables of interest are the absorption cross sections for the two possible helicity states.
Applying the analysis procedure described in chapter 6 and using Eq.(6.5), it was possible to estimate the cross section difference $\Delta\sigma_{31} = \sigma_{3/2} - \sigma_{1/2}$. In this difference, the contribution from events coming from the target windows and the beam halo vanishes and the pure ^{3}He contribution can be obtained. The good agreement of our unpolarised hydrogen and ^{3}He data with previously published data gave us confidence in the analysis procedure. Hence, including the beam and target polarisation in this analysis and taking into account the simulated detector efficiencies and the extrapolation correction determined in the previous chapter, the total polarised cross section difference could be determined.
Fig. 7.2 shows the result obtained for the helicity dependent total photoabsorption cross section difference on ^{3}He as a function of the incoming photon energy. These results are compared with the predictions from the model of A.Fix (black curve) and from the SAID (red curve) and MAID (blue curve) multipole analysis.
In the case of the SAID and MAID, the prediction is simply the sum of all free Nπ helicity dependent cross section differences according to Eq.(6.10).
The model of A.Fix is a straightforward extension of the work previously done on the deuteron [119]. The elementary production operator $\gamma p \rightarrow N\pi$ is taken from the MAID multipole analysis and is afterwards embedded into the ^{3}He wave function to take into account the nuclear effects. An empirical attenuation factor was then applied to take into account the absorption of the photoemitted particles inside the nuclear medium.
As it can be seen from the comparison of the MAID and Fix curves of Fig. 7.2, the predicted role of the nuclear effects is to damp and broaden the peak due to the excitation of the Δ resonance. This effect, which is mainly due to the Fermi motion of the interacting neutron, has also been observed in the unpolarized total inclusive cross section data [121].
As one can see in Fig. 7.2, the agreement between our experimental data and the SAID and MAID models is reasonable, taking into account the non-negligible statistical errors of the experimental data. Hence, it seems that the nuclear effects are not so important

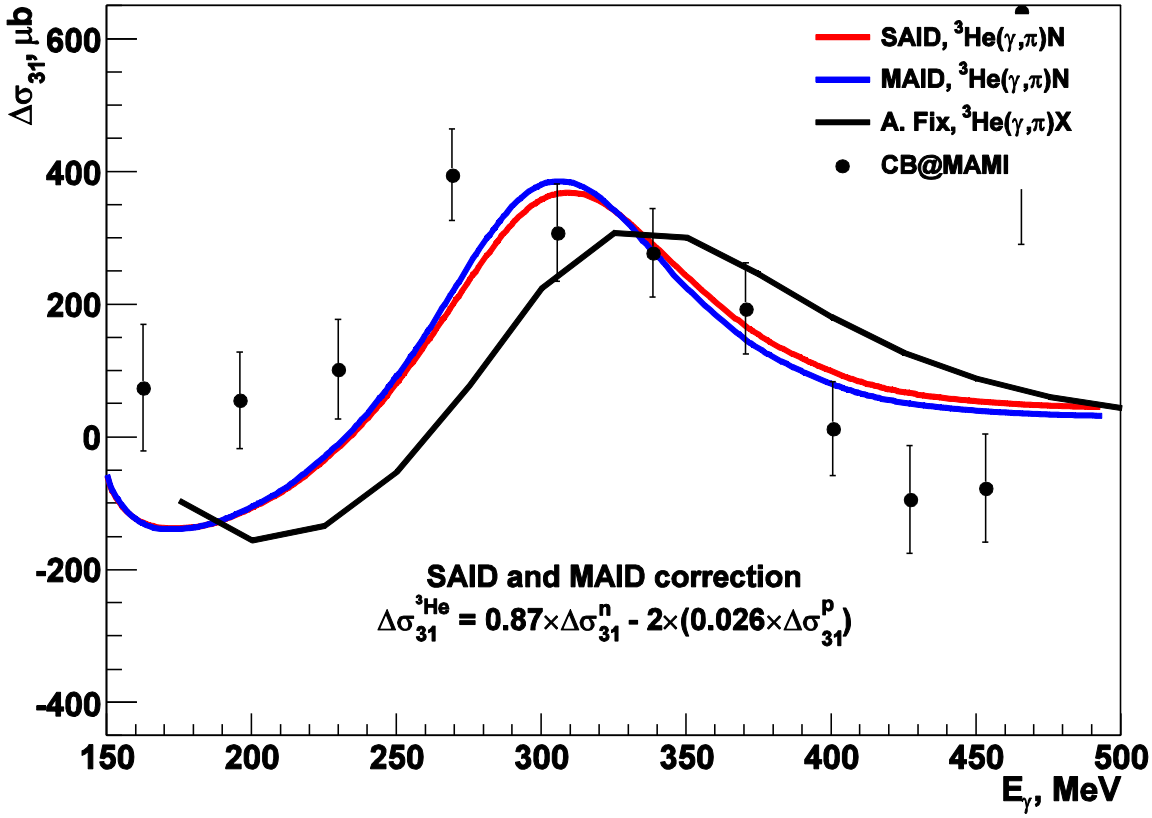

Figure 7.2: Helicity dependent total photoabsorption cross section difference, $\Delta\sigma_{31} = \sigma_{3/2} - \sigma_{1/2}$ on ^{3}He as a function of the photon energy.

in this case or that the free $\gamma N \rightarrow N\pi$ amplitude is underestimated by MAID.
For these reasons, further theoretical calculations and more accurate experimental data, as well as a deeper analysis of the existing data is required. The photon flux evaluation has to be checked in more detail and the information of the PID and MWPC has to be fully developed and implemented in the analysis to evaluate the helicity dependent cross section for the partial $\gamma N \rightarrow N\pi$ channels.

7.3 The GDH Sum Rule on the neutron

From the results and the discussion presented in the previous section it is clear that the present models can not be used for a reliable extraction of the free neutron information from the ^{3}He data obtained at Mainz. Although more complete models [122] are now under development, the very simple model, previously used for the extrapolation correction (Eq.6.10), can be used to have a very rude neutron extraction method.
In the upper part of Fig. 7.3 the helicity dependent total cross section difference as a function of the photon energy obtained with the ^{3}He measurement compared to the results obtained by the GDH collaboration for the proton and the deuteron is shown. From these results the "free neutron" data for the ^{3}He and the deuteron can be extracted in a very simple way, disregarding nuclear effects and taking into account only the effect of the small wave function components on the nucleon orientation. As it has been mentioned in section 4.1, besides the S wave, the three-body wave function contains a percentage of S' and D waves, $P_{S'}$ and P_D, which are responsible for a proton contribution to the polarisation of ^{3}He . The amount of such a contribution can be calculated by considering the quantities $P_{p(n)}$ (the so called "effective nucleon polarisations") that represent the probability to have a proton (neutron) with spin parallel to ^{3}He spin.
In a pure S-wave state $P_n = 1$; $P_p = 0$, whereas for a 3-body wave function containing S, S' and D-waves one has:

$$P_n = 1 - \frac{2}{3}P(S') - \frac{4}{3}P(D)$$

$$P_p = -\frac{1}{3}[P(D) - P(S')]$$

being P(D) and P(S') the D- and S'-wave probabilities. With P(D) = 8.37% and P(S') = 1.6%, one gets P_n = 87% and P_p = -0.026%.
Under this approximation one then has:

$$\Delta\sigma_{^3He} = 0.87\Delta\sigma_{neutron} - 0.052\Delta\sigma_{proton}; \Delta\sigma_{neutron} = \frac{\Delta\sigma_{^3He} + 0.052\Delta\sigma_{proton}}{0.87}$$

In a similar way, the extraction of the free neutron from the deuterium can be performed by:

$$\Delta\sigma_{deuteron} = 0.92(\Delta\sigma_{proton} + \Delta\sigma_{neutron}); \Delta\sigma_{neutron} = \frac{\Delta\sigma_{deuteron}}{0.92} - \Delta\sigma_{proton}$$

where the 0.92 factor represents the effective proton/neutron polarisation in the deuteron. The comparison between the "free neutron" data obtained with this simple model is shown in the lower part of Fig. 7.3. Both results are also compared to the SAID and MAID models for the sum of all single pion photoproduction channels on the neutron.
Given the very rough nature of the used approximation, one can say that there is a good agreement between the two extracted free "neutron" data. These data are also not too much different from the free neutron predictions from SAID and MAID.
In Fig. 7.4 is presented the helicity dependent total photoabsorption cross section difference from the deuteron obtained by the GDH collaboration and the "free neutron" extraction as a function of the photon energy compared with the total photoabsorption cross section difference and the "free neutron" extraction from the ^{3}He measurement. As it can be clearly seen, due to the spin structure function of the ^{3}He (see section 4.1) the proton contribution to the measured helicity dependent yields is much smaller in the ^{3}He than in the deuteron case. Thus, the photoabsorption on a polarised ^{3}He target is a very promising alternative method to investigate the GDH integral for the neutron.

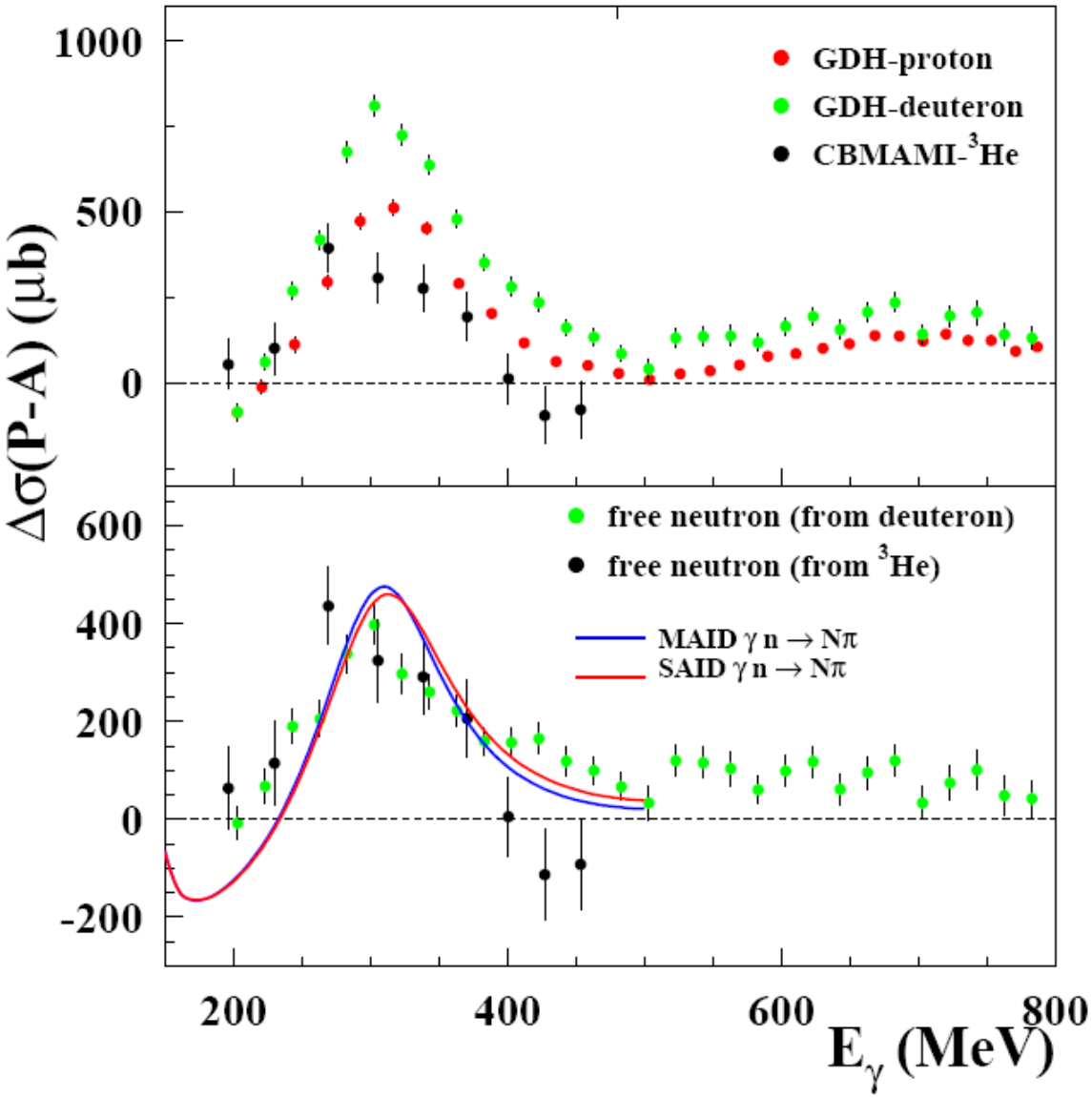

Figure 7.3: In the upper part is presented the helicity dependent total photoabsorption cross section difference on ^{3}He as a function of the photon energy compared with the results obtained by the GDH collaboration for the proton and the deuteron. In the lower part there is a comparison between the "free neutron" extraction from the ^{3}He and deuteron.

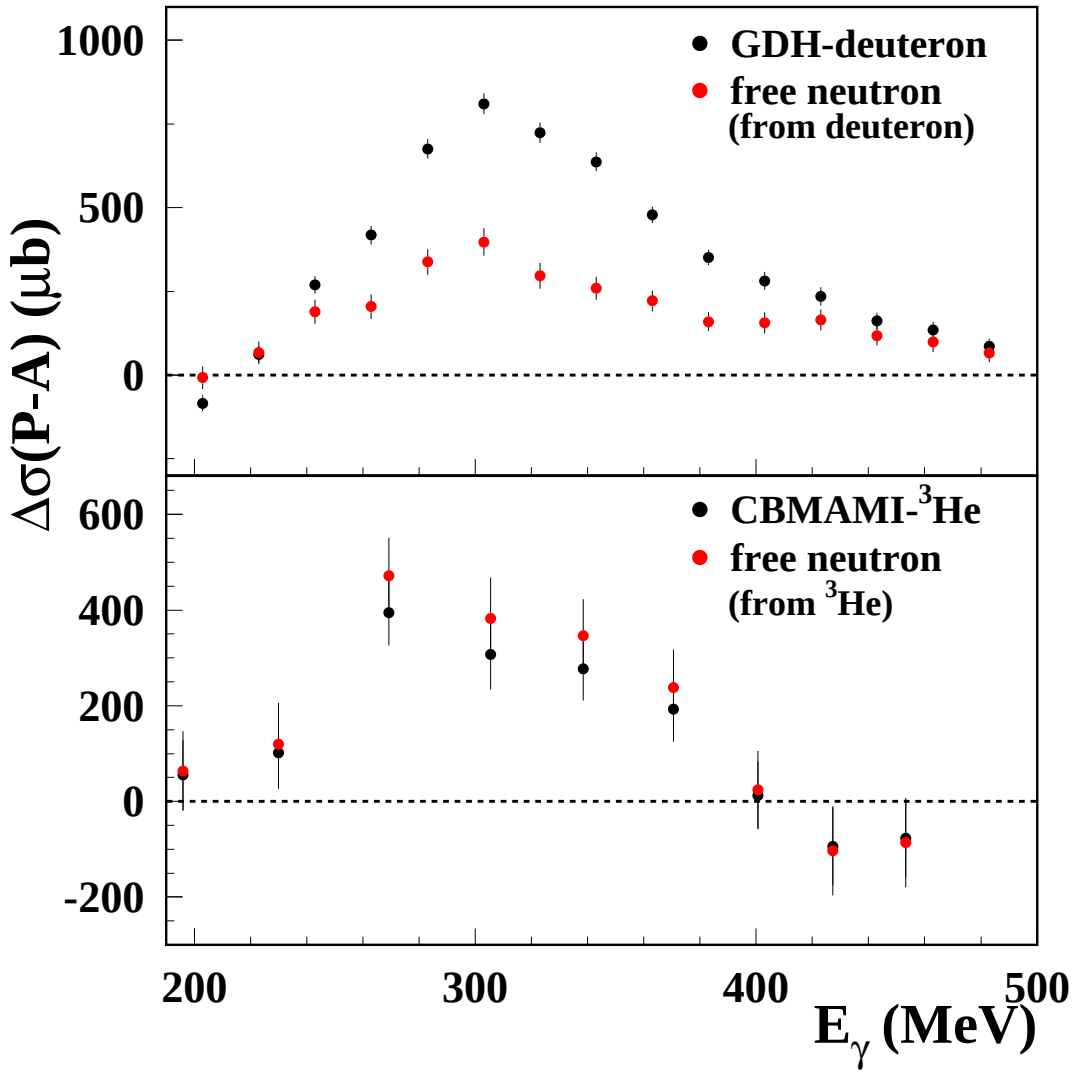

Figure 7.4: In the upper part is presented the helicity dependent total photoabsorption cross section difference from the deuteron obtained by the GDH collaboration and the "free neutron" extraction as a function of the photon energy. In the lower part is shown the total photoabsorption cross section difference and the "free neutron" extraction from the ^{3}He measurement.

Chapter 8
Summary and Conclusions

The experimental verification of the Gerasimov-Drell-Hearn (GDH) sum rule which is based on very general quantum mechanical principles, provides a fundamental information about the spin structure of the nucleon. The use of a circularly polarised photon beam and a longitudinally polarised nucleon target gives access to the measurement of the helicity dependent cross sections, the observables that are needed for this verification. The first experimental check of the GDH sum rule was the measurement of the total photoabsorption cross section on the proton carried out jointly at Mainz and Bonn by the GDH collaboration, with a measured photon energy range between 200 MeV and 2.9 GeV. The combined results obtained in this measurements support the validity of the GDH sum rule for the proton. The helicity dependent total inclusive cross section on the deuteron was also measured by the GDH collaboration in the photon energy range from 200 MeV to 1.9 GeV at Mainz and Bonn.
Due to the lack of free neutron targets, the most accurate experimental verification of the GDH sum rule on the neutron is obtained using a polarised ^{3}He target. This is because the ^{3}He is a two spin paired proton system with an unpaired neutron in relative S states, thus the magnetic moment of the ^{3}He is approximately equal to the neutron magnetic moment. Therefore, the proton contribution to the measured helicity dependent yields is very small making the ^{3}He spin structure be very close to the free neutron.
For this reason, the first double polarisation experiment on ^{3}He with a measured photon energy range between 200 and 800 MeV was performed. This measurement was carried out in Mainz in July 2009.
The preparation of the whole ^{3}He experimental setup and the analysis procedure of the data obtained in this measurement were described in this thesis.
A detailed explanation of the different components of the ^{3}He setup was also given. The design of a solenoid needed to provide a magnetic holding field for the ^{3}He gas was presented, as well as the different tests carried out to measure the magnetic field and gradients in the target region. The design and test of the Helmholtz coils used in the polarimetry measurement were also presented. Another important issue shown in this work was the

production, preparation, and properties of the different target cells used in the ^{3}He measurement.
In March 2009, a feasibility test for a total inclusive measurement of the photoabsorption cross section on unpolarised hydrogen was carried out. The aim of this measurement was to test the detector response and the trigger conditions to be applied later to the polarised measurement. Since it is essential to suppress as much as possible the electromagnetic background induced from pair production and Compton scattering at forward polar angles, a threshold Cherenkov detector was installed downstream of the Crystal Ball.
Due to the good agreement between the cross section results on hydrogen compared to previous measurements, the analysis procedure used with the unpolarised data was applied to the polarised data, with some minor modifications.
In the measurement carried out with a polarised ^{3}He target two MAMI energy settings, 855 MeV and 525 MeV, were used. Due to several acquisition and detector problems in the 855 MeV period and the substantial background present in the data obtained, only the results for the 525 MeV period are presented in this work.
In order to check the data quality and analysis method, the total photoabsorption cross section on unpolarised ^{3}He was determined from the polarised ^{3}He data. This cross section was compared with previous data obtained with the DAPHNE detector showing a good agreement between both cross sections.
The helicity dependent photoabsorption cross section difference on ^{3}He was also obtained. These results were compared with the free neutron models SAID and MAID and with the model of A. Fix. Within the error bars there is a reasonably good agreement between our results and the SAID and MAID models. A comparison between the results obtained for the extraction of the "free neutron" from the ^{3}He data and the deuteron data obtained by the GDH collaboration using a very simple model based on SAID and MAID, also shows that both neutron results are quite similar.
These first data obtained for the neutron from ^{3}He are consistent within the errors with the data extracted from the deuteron measurement. A test of the GDH sum rule for the neutron requires more accurate experimental data in a wide photon energy range and further theoretical calculations to take into account the nuclear effects. Also the analysis of the existing data is still in progress. The photon flux evaluation has to be checked in more detail and the information of the PID and MWPC has to be fully developed and implemented in the analysis for the study of the helicity dependent cross sections for some partial reaction channels. This work will provide some information to evaluate the properties of the baryon resonances and a very detailed check of the nuclear models needed for the extraction of the free-neutron information.
The results that has been shown in this thesis already prove that a polarised ^{3}He gas target can be used for the experimental check of the GDH sum rule on the neutron. From the experience gained in this experiment, we can in future improve the experimental conditions with the use of:

1. a smaller collimator that will decrease the beam halo component by a factor of 2.

2. improved trigger conditions that will allow to have different thresholds for different CB sections and to have a on-line cluster algorithm for a more efficient background rejection. Present estimates indicate that at least 50% of the background can be on-line vetoed.

3. a faster data acquisition system that now allows to collect a double number of events than before.

In the meanwhile, additional work on the target cells has been performed and, at the moment, the relaxation time T_1 has increased to about 40 hours.
Taken all this facts into account, it will be possible to measure the helicity dependence of the main partial meson photoproduction channels, i. e, $\gamma N \rightarrow N\pi$, $\gamma n \rightarrow N\pi\pi$ and $\gamma n \rightarrow n\eta$.

Bibliography

[1] R. E. Taylor, Proc. of 4th Int. Symp. on Electron and Photon interactions at High Energies. Daresburg, Eng., 251 (1969).

[2] R. P. Feynman, Phys. Rev. Lett. 23, 1415 (1969).

[3] M. Gell-Mann, Phys. Lett. 8, 214 (1964).

[4] G. Zweig, CERN report TH-401, 412 (1964).

[5] The E80 collaboration: M. Alguard et al. *Deep inelastic scattering of polarized electrons by polarized protons*, Phys. Rev. Lett. 37, 1261 (1976).

[6] The E130 collaboration: G. Baum et al., Phys. Rev. Lett. 45, 2000 (1980).

[7] The EMC collaboration: J. Ashman et al., *A measurement of the spin asymmetry and determination of the structure function g_1 in deep inelastic muon-proton scattering.* Phys. Lett. B 206. 2. 364 (1988).

[8] J. D. Bjorken, Phys. Rev., 148 (1966); Phys. Rev. D 1, 1376 (1970).

[9] J. Ellis and R. L. Jaffe, Phys. Rev. D 9, 1444 (1974); (E) D 10, 1669 (1974).

[10] S. D. Drell and A. C. Hearn, Phys. Rev. Lett. 162, 1520 (1966); S. B. Gerasimov, Yad. Fiz. 2, 839 (1965).

[11] P. Minkowski, in Proc. Workshop on Effective Field Theories of the Standard Model, Hungary (1991), ed. U.-G. Meissner (World Scientific, Singapore, 1992).

[12] J. Kodaira, Nucl. Phys. B 165, 129 (1980).

[13] S. A. Larin, Phys. Lett. B 334, 192 (1994).

[14] G. Altarelli and G. Ridolfi, Nucl. Phys. B (Proc. Suppl.) 39B,C, 106 (1995).

[15] S. D. Bass, R. J. Crewther, F. M. Steffens and A. W. Thomas, hep-ph/9701213.

[16] J. R. Johnson et al., Nucl. Instr. and Meth. in Phys. Res. A 356, 148 (1995).

[17] R. M. Woloshyn, Nucl. Phys. A 496, 749 (1989).

[18] S. B. Gerasimov, Yad. Fiz. 2, 598-602 (1965); Sov. J. Nucl. Phyz. 2, 430-433 (1966).

[19] S. D. Drell and A. C. Hearn, Phys. Rev. Lett. 16, 908-911 (1966).

[20] M. M. Giannini, Proceedings of the Second International Symposium on the GDH Sum Rule and the Spin Structure of the Nucleon, 1st ed., edited by M. Anghinolfi, M. Battaglieri, and R. D. Vita (World scientific, New Jersey 2003).

[21] G. B. Arfken and H. J. Weber, Mathematical Methods for Physicists 4th ed. (Academic Press, San Diego, California 1995).

[22] F. E. Low, Phys. Rev. 96, 1428 (1954).

[23] M. Gell-Mann and M. L. Goldberger, Phys. Rev. 96, 1433 (1954).

[24] A. Donnachie and P. Landshoff, Phys. Lett. B 296, 227 (1992).

[25] P. D. B. Collins,*Introduction to Regge Theory*, Cambridge University Press (1977).

[26] S. D. Bass, Mod. Phys. Lett. A 12, 1051 (1997).

[27] M. Gell-Mann, M. L. Goldberger and W. E. Thirring, Phys. Rev. 95, 1612 (1954).

[28] M. Anselmino, B. L. Ioffe and E. Leader, *On possible resolution of the spin crisis in the parton model*. Sov. J. Nucl. Phys. 49, 136 (1989).

[29] V. Burkert and B. Ioffe, *On the Q^2 Variation of the Spin Dependant Electron-Proton Scattering*. CEBAF PR 92-018 (1992).

[30] V. Burkert and B. Ioffe, *Polarized Structure Function of the Proton and the Neutron and the GDH and Bjorken Sum Rules*. CEBAF PR 93-034 (1993).

[31] V. Burkert and Z. Li, *What do We Know About the Q^2 Evolution of the GDH Sum Rule*. CEBAF PR 92-017 (1992).

[32] V. Bernard, N. Kaiser and U. Meissner, *Small Momentum Evolution of the Extended Drell-Hearn-Gerasimov sum rule*. Phys. Rev. D 48, 3062 (1993).

[33] J. Soffer and O. Teryaev, *Role of g_2 in Relating the Schwinger and Drell Hearn Gerasimov Sum Rules*. Phys. Rev. Lett. 70, vol. 22, 3373 (1993).

[34] J. Soffer and O. Teryaev, *Comment on the Burkhardt-Cottingham and Generalised GDH Sum Rules for the Neutron*. Phys. Rev. D 56, 7458 (1997).

[35] D. Drechsel, S. S. Kamalov, G. Krein and L. Tiator, *The Generalized Gerasimov-Drell-Hearn Integral and the Spin Structure of the Nucleon*. Phys. Rev. 59, 094021 (1999).

[36] Z. Li, *Polarized Structure Function of the Nucleon in the Resonance Region*. Phys. Rev. D 47 - 5 1854 (1993).

[37] M. Anselmino et al., Sov. J. Nucl. Phys. 49, 1 (1989).

[38] X. Ji and J. Osborn, *Generalized Sum Rules for Spin Dependent Functions of the Nucleon*. hep-ph 9905410 (1999).

[39] F. E. Close and R. G. Roberts, Phys. Lett. B 316, 165 (1993).

[40] L. Montanet et al., Particle Data Group, Phys. Rev. D 50, 1173 (1994).

[41] J. Ellis and M. Karliner, Phys. Lett. B 341, 397 (1995).

[42] HERMES collaboration, K. Ackerstaff et al., Phys. Lett. B 444, 531 (1998).

[43] Fatemi et al., Phys. Rev. Lett. 91, 222002 (2003).

[44] H. Herminghaus, *Bau und Betrieb von MAMI, Arbeits und Ergebnisbericht 1987-1989* (SFB 201) (1989).

[45] H. Herminghaus et al., Nucl. Instr. Meth. 138, 1 (1976).

[46] S. Nakamura et al., Nucl. Instr. Meth. A 411, 93-106 (1998).

[47] D. Drechsel and T. W. Walcher, Rev. Mod. Phys 80, 731 (2008).

[48] R. A. Arndt et al., Phys. Rev. C 66, 055213 (2002).

[49] D. Drechsel et al., Phys. Rev. D 63, 114010 (2001).

[50] A. Fix and H. Arenhövel, Eur. Phys. J. A 25, 115 (2005).

[51] S. Sumowigado and T. Mart, Phys. Rev. C 60, 028201 (1999).

[52] Q. Zhao, J. S. Al-Khalili and C. Bennhold, Phys. Rev. C 65, 032201 (2002).

[53] N. Bianchi and E. Thomas, Phys. Lett. B 450, 439 (1999).

[54] S. Simula et al., Phys. Rev. D 65, 034017 (2002).

[55] H. Weller et al., Prog. Part. Nucl. Phys. 62, 257 (2009).

[56] D. Drechsel et al., Nucl. Phys. A 645, 145 (1999); http://www.kph.uni-mainz.de/MAID/

[57] K. Aulenbacher et al., Nucl. Instr. Meth. A 391, 498 (1997).

[58] I. Anthony et al., Nucl. Instr. Meth. A 301, 230 (1991).

[59] S. J. Hall et al., Nucl. Instr. Meth. A 368, 698 (1996).

[60] H. Olsen and L. C. Maximon, *Photon and Electron polarization in High-Energy Bremsstrahlung and Pair Production with Screening*, Phys. Rev. 114, 887 (1959).

[61] B. Wagner et al., Nucl. Instr. Meth. A 294, 541-548 (1990).

[62] H. Olsen, Springer Tracts in Mod. Phys. 44, 83 (1968).

[63] U. Stockter, Diplomarbeit, University of Mainz (1996).

[64] G. Audit et al., *DAPHNE: a large-acceptance tracking detectorfor the study of photoreactions at intermediate energies*. Nucl. Instr. Meth. A 301, 473-481 (1991).

[65] E. Bosze et al., *Rohacell foam as a silicon support structure material for the PHENIX multiplicity vertex detector*. Nucl. Instr. Meth. A 400, 224-232 (1997).

[66] B. Lannoy, Ph, D. thesis, University of Gent (2000).

[67] D. Ryckbosch, private communication.

[68] N. Reynaert, licentiate's thesis (1995).

[69] R. Novotny, *The BaF_2 photon spectrometer TAPS*. IEEE Transactions on Nuclear Science 38, 379-385 (1991).

[70] K. Kleinknecht, *Detectors for Particle Radiation*. Cambridge University Press (1986).

[71] R. Novotny et al., *Scintillators for photon detection at medium energies - a comparative study of BaF_2, CeF_3 and $PbWO_4$*. Nucl. Instr. Meth. A 486, 131-135 (2002).

[72] R. M. Woloshyn, Nucl. Phys. A 496, 749 (1989).

[73] D. Krambrich, *Aufbau des Crystal Ball-Detektorsystems und Untersuchung der Helizitätsasymmetrie in $\gamma p \to p\pi^0\pi^0$*. Ph. D thesis, University of Mainz (2007).

[74] P. Drexler, *Entwicklung und Aufbau der neuen TAPS-Elektronik*. Ph. D thesis, University of Giessen (2004).

[75] Root manual: http://root.cern.ch.

[76] S. Stringarl, *Spin Polarised Quantum Systems*, Ed. (World Sci.Pub.Co. (1989).

[77] J. Becker et al., Nuc. Instr. Meth. A 402, 327 (1998).

[78] G. L. Jones et al., Nuc.Instr Meth. A 440, 772 (2000).

[79] W. Heil et al., Nuc.Instr Meth. A 485, 551 (2002).

[80] C. H. Tseng, G. P. Wong,V. R. Pomeroy, R. W. Mair, D. P. Hinton,D. Hoffmannand, R. E. Stoner, F. W. Hersman, D. G. Cory and R. L. Walsworth. *Low-Field MRI of Laser Polarized Noble Gas.* Phys. Rev. Lett. 81, 3785-3788 (1998).

[81] M. Salerno, E. E. de Lange, T. A. Altes, J. D. Truwit, J. R. Brookeman, and J. P. Mugler III. *Hyperpolarized ^{3}He diffusion MRI of the lungs in emphysema:Comparison with pulmonary function test-Initial experience.* Radiography, 222:252-26 (2002).

[82] S. Fichele. *Hyperpolarized ^{3}He Gas Production for Magnetic Resonance Imaging of the Human Air-ways.*PhD-thesys, University of Nottingham (2002).

[83] A. J. Deninger, B. Eberle, M. Ebert, T. Grossmann, et al., *Quantification of regional intrapulmonary oxygen partial pressure evolution during apnea by He-3 MRI.* Journal of Magnetic Resonance, 141:207-216 (1999).

[84] D. Rohe et al., Phys. Rev. Lett. 83, 4257 (1999).

[85] J. Krimmer et al., Nuc.Instr Meth. A 611, 18 (2009).

[86] B. G. Yerozolimsky, Nucl. Instr. Meth. Phys. A 440, 491 (2000).

[87] B. Blankleider and R. M. Woloshyn, Phys. Rev. C 29, 538 (1984).

[88] R. Schulze and P. Sauer, Phys. Rev. C 48, 38 (1990).

[89] J. L. Friar et al., Phys. Rev. C 42, 2310 (1990).

[90] C. G. Aminoff, C. Larat, M. Leduc, Revue Phys. Appl. 24, 827 (1989).

[91] E. Stolz, M. Mayerhoff, N. Bigelow, M. Leduc, P. J. Nacher and G. Tastevin. *High-nuclear polarization in ^{3}He and ^{3}He–^{4}He mixtures by optical pumping with a laser diode.* Applied Physics B 63, 629-633 (1996).

[92] T. R. Gentile and R. D. McKewon. *Spin-Polarizing He-3 Nuclei with an Arc-Lamp-Pumped Neodymium-Doped Lanthanum Magnesium Hexaluminate Laser.* Physical Review A 47, 456-467 (1993).

[93] C. Larat. PhD thesis Université Paris (1991).

[94] M. Wolf. Ph. D thesis University of Mainz (2004).

[95] J. Schmiedeskamp. Ph. D thesis University of Mainz (2005).

[96] E. Otten, Europhysics News 35, 16 (2004).

[97] M. Batz et al., J. Res. Natl. Inst. Stand. Technol. 110, 293 (2005).

[98] N. Newbury et al., Phys. Rev. A 48, 4411 (1993).

[99] W. Heil, H. Humblot, E. Otten, M. Schaffer, R. Surkau and M. Leduc, Phys. Lett. A 201, 337 (1995).

[100] A. J. Deninger et al., Eur. Phys. J. D 38, 439 (2006).

[101] L. D. Schearer and G. K. Walters, Phys. Rev. 139 (5A)1398 (1965).

[102] F. D. Colegrove, L. D. Schearer and G. K. Walters, Phys. Rev. 132, 2561 (1963).

[103] W. A. Fitzsimmons, L. L. Tankersley and G. K. Walters, Phys. Rev. 179, 156 (1969).

[104] R. S. Timsit, J. M. Daniels, and A. D. May, Can. J. Phys. 49, 561 (1971).

[105] J. Schmiedeskamp et al., Eur. Phys. J. D 38, 427 (2006).

[106] E. Cheng, M. W. Cole, W. F. Saam and J. Treiner, Phys. Rev. Lett. 67, 1007 (1991).

[107] J. Schmiedeskamp et al., Eur. Phys. J. D 38, 445 (2006).

[108] F. Thiel et al., Rev. Sci. Instr. 78, 035106 (2007).

[109] D. Meeker, *Finite Element Method Magnetics. Version 4.0 User's Manual 2004.*

[110] P. Aguar Bartolomé, Diplomarbeit, University of Mainz (2005).

[111] A. Reiter et al., *A microscope for the Glasgow photon tagging spectrometer in Mainz.* Eur. Phys. J. A 30 (2006).

[112] K. Livingston, AcquTagger Manual: http://nuclear.gla.ac.uk/ acqusys/doc/AcquTagger.pdf.

[113] T. A. Armstrong et al., Phys. Rev. D 5, 1640 (1972).

[114] M. MacCormick et al., Phys. Rev. C 53, 41 (1996).

[115] O. Bartalini et al., Phys. Atom. Nucl. 71, 75 (2008).

[116] MAMI, A2-Collaboration proposal: Helicity dependence of single and double pion photoproduction processes and the GDH integral on the neutron. (PAC 2009).

[117] M. Goosens. *GEANT - Detector Description and Simulation Tool*, CERN Program Library Long Writeup W5013, CERN (1994).

[118] H. Arenhövel and A. Fix, Phys. Rev. C 72, 064004 (2005).

[119] A. Fix and H. Arenhövel, Phys. Rev. C 72, 064005 (2005).

[120] A. Fix, private communication.

[121] M. MacCormick et al., Phys. Rev. C 55, 1033 (1997).

[122] D. R. Phillips, J. Phys. G: Nucl. Part. Phys. 36, 104004 (27pp) (2009).